DETERMINATION OF TISSUE OPTICAL PROPERTIES

DETERMINATION OF TISSUE OPTICAL PROPERTIES FROM INTERSTITIAL FLUENCE RATE MEASUREMENTS: A STUDY OF THE SYSTEMATIC ERRORS

By

PATRICIA D. SINGH

A Thesis

Submitted to the School of Graduate Studies

in Partial Fulfilment of the Requirements

for the degree

Master of Science

McMaster University

MASTER OF SCIENCE (1994) MCMASTER UNIVERSITY

(Physics) Hamilton, Ontario

TITLE: Determination of Tissue Optical Properties from Interstitial Fluence Rate Measurements: A Study of the Systematic Errors

AUTHOR: Patricia D. Singh, B. Sc. (University of the West Indies)

SUPERVISOR: Dr. M.S. Patterson

NUMBER OF PAGES: xi, 123

Abstract

Increased efficacy of light and laser applications in medicine is achieved by accurate light dosimetry. A minimally invasive technique for the determination of the optical coefficients of tissue involves interstitial measurements of the local fluence rate at two or more points in the tissue using isotropic, fibre optic detectors and application of a diffusion model of light propagation. The diffusion models assume simple, homogeneous tissue geometries, possibly oversimplifying the effect of tissue heterogeneities and boundaries. The primary goals of this study were to investigate the influence of realistic finite geometries on the fluence rate distribution and to quantify the systematic errors in the derived optical properties.

A Monte Carlo model was developed to predict the fluence rate distribution in any plane of interest in a medium and was verified by comparison with diffusion theory solutions for simple geometries. Fluence rate measurements were made in optically infinite and semi-infinite phantoms for a wide range of optical properties and it was determined that the optical coefficients were derived accurately for phantoms with $\mu_{eff} > 0.2$ mm^{-1} and $2 < \mu_t' < 10$ mm^{-1}.

Measurements were also made in finite spherical volumes with absorbing ($R_d = 0.35$) and diffuse reflecting ($R_d = 0.85$) boundaries for three optical phantoms and comparisons of the experimental fluence rates with the predictions of the finite volume Monte Carlo model are presented. Boundary effects were observed to be significant within 4 transport mean free paths (mfp') of the boundary. The optical coefficients were derived by applying a diffusion solution for an infinite medium and it was determined that within 2 mfp' of the boundary, the derived μ_a was overestimated by 40% and underestimated by 20% for the absorbing and reflecting boundaries, respectively.

Acknowledgements

I wish to thank Dr. M.S. Patterson for his supervision, helpful discussions and suggestions. The assistance of Dr. L. Lilge in all aspects of this thesis is gratefully acknowledged. Thanks also to Dr. T. Farrell for taking the time to answer to my questions about Monte Carlo techniques. I am deeply grateful to the following people whose assistance in the lab was invaluable: James Joseph, Dr. J. Heyward, Julie Northcott, Glendon Lee and Brian Pogue. My sincere thanks to my parents for teaching me the value of a good education. And last but certainly not least, thanks to Reza for helping me to keep things in perspective.

Table of Contents

Table of Figures

Table of Tables

Chapter 1

Introduction

Developments in laser instrumentation and fibre optic technology have led to increased light and laser applications in medicine. Improved efficacy of diagnostic and therapeutic applications relies on, among other factors, accurate light dosimetry. Therapeutic procedures, such as photodynamic therapy, laser hyperthermia and laser biostimulation (Parrish & Wilson, 1991), are dependent on the absorption (and indirectly, the scattering) of light photons in the target tissue to produce the desired biological effects. Diagnostic techniques which include fluorescence and absorption spectroscopy rely instead on detecting fluorescence emission and changes in the intensities of the remitted photons, respectively (Parrish & Wilson ,1991). Light propagation in tissue is governed by the optical properties of tissue, which will be discussed in the next section.

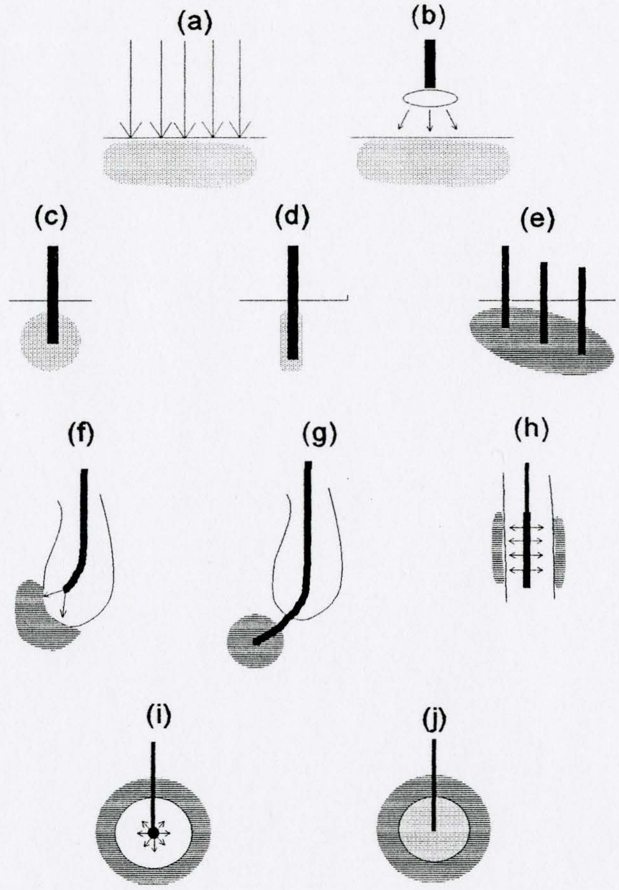

Figure 1.1 Examples of the irradiation geometries used in photodynamic therapy. The stippled areas represent schematically the pattern of irradiance in highly scattering tissue. (a), (b) Surface irradiation from broad beam or lens-tipped fibre. (c)-(e) Interstitial irradiation with cut-end or cylindrical fibres. (f)-(h) Intracavitary and intralumenal irradiation. (i), (j) Intracavitary whole surface irradiation using an isotropically-tipped fibre or a light diffusing liquid (shaded). (Wilson & Patterson, 1986)

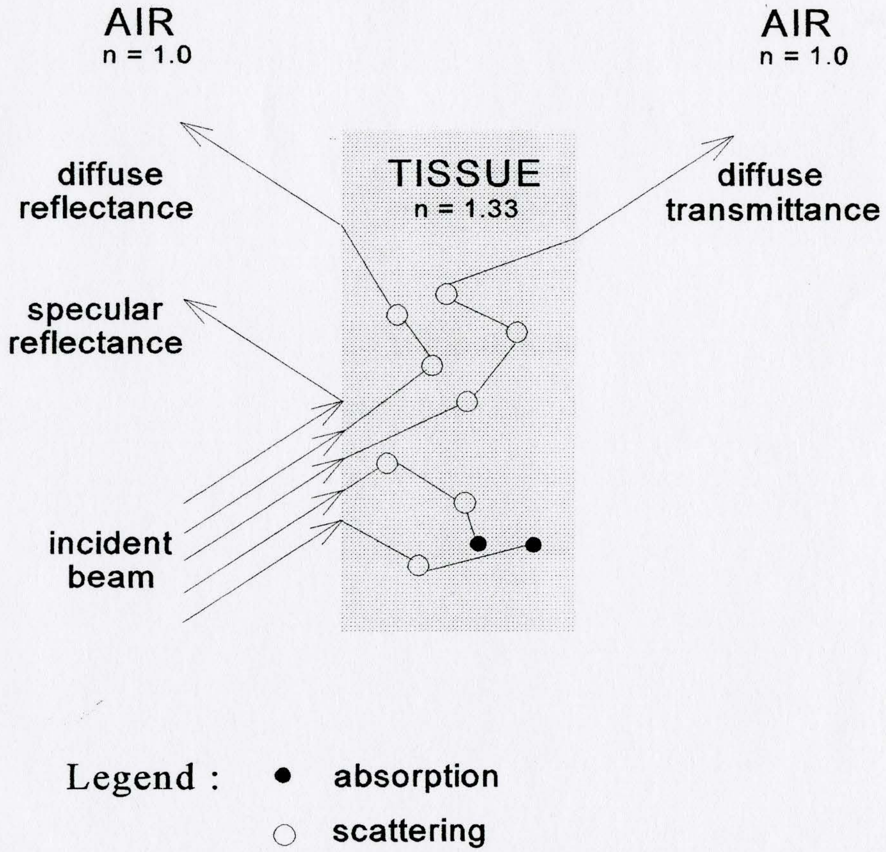

Figure 1.2 Interactions of light photons with tissue (Svaasand, 1984; Doiron, 1984)

1.1 Tissue optical properties

In diagnosis and therapy, light can be delivered to the target tissue by surface illumination or by interstitial, intralumenal or intracavitary irradiation via optical fibres, as shown in Figure 1.1 (Wilson & Patterson, 1986). For a particular irradiation geometry, the spatial distribution of the light energy fluence rate within optically turbid media, such as biological tissue, is dependent on the wavelength-dependent absorption and scattering characteristics of the medium. The primary interactions of light photons with tissue are absorption and elastic scattering but photons can also be specularly reflected at the surface or may be diffusely reflected or transmitted, as shown in Figure 1.2.

Many applications exploit the spectral region, 600 -1300 nm, known as the "optical window" because tissue absorption is lowest in this region thereby allowing maximum light penetration to be achieved (Wilson, 1991a, Wilson & Jacques, 1990). In this wavelength range (visible and near IR), absorption of photons is due to tissue chromophores such as haemoglobin, melanin and bilirubin while scattering arises from microscopic variations in the refractive index of the tissue (Wilson, 1991a; Star et al., 1991). On a macroscopic level, however, tissue can be characterized by an average refractive index, n, which gives rise to specular reflection at tissue-air interfaces. Scattering in tissue is highly forward peaked, similar to that observed for isolated particles which are comparable in size to the wavelength of the incident light (Wilson, 1991a,b). The angular distribution of scattering from each particle is uniquely specified by a phase function, $S(\theta)$, described in Chapter 2. Typically the average cosine of the phase function, called the anisotropy parameter, g, is used to characterize the nature of the scattering where values of 0 and 1 represent isotropic and forward directed scattering, respectively. The scattering coefficient, μ_s, and anisotropy parameter are often combined into a single reduced scattering coefficient, $\mu_s' = \mu_s(1 - g)$, for computational ease.

The fundamental optical parameters for light dosimetry are the absorption and scattering coefficients, μ_a and μ_s, which represent the probabilities per unit path length for photon absorption and scattering, respectively. For most tissues in the visible and near IR, scattering dominates absorption and the range of values for the absorption and reduced scattering are $0.01 < \mu_a < 1.0\ mm^{-1}$ and $10 < \mu_s < 100\ mm^{-1}$ (Wilson, 1991b, Wilson & Jacques, 1990), respectively. The highly forward-directed scattering in tissue is characterized by an anisotropy parameter typically between 0.7 and 0.95 (Wilson, 1991b) and the average tissue refractive index, n, ranges from 1.38 to 1.41 (Bolin et al., 1989).

1.2 Light Dosimetry

Optimization of light delivery in therapeutic procedures, such as photodynamic therapy (PDT) requires accurate light dosimetry or light treatment planning (Wilson et al., 1987; Wilson & Patterson, 1986). As shown in the schematic of Figure 1.3, light dosimetry for PDT (Wilson et al., 1987) involves an inverse and a forward problem. The former is the more difficult problem of determination of the optical properties of the tissue while the latter is a forward calculation of the spatial distribution of the light fluence rate throughout the tissue volume of interest, based on the known optical properties, irradiation conditions and a mathematical model of light propagation.

The optical properties of tissue, μ_a , μ_s and g or μ_a and μ_s', can be determined either directly or indirectly. Direct determination from measurements of the light transmitted through and reflected from tissue samples, has the advantage of being independent of a model of light propagation. However, these measurement techniques are necessarily invasive and require optically thin tissue samples (thickness $\leq$ 100 μm) so that only singly scattered photons are detected (Wilson et al., 1987). In addition to the difficulties involved in tissue preparation, the measurement of optical parameters such as μ_a , μ_s, the total attenuation coefficient, μ_t (= $\mu_a + \mu_s$), and the phase function, S(θ), present a number of technical problems as discussed by Wilson et al. (1987). Some of these are reduction of background light, minimization of refraction at interfaces and in the case of determination of the scattering coefficient, measurement of the forward scattered light only.

Indirect techniques are preferred since measurements can be made in bulk tissue *in vivo* (Wilson et al., 1987). These involve measurements of macroscopic parameters such as the effective attenuation coefficient, penetration depth, reflectance, transmittance and fluence rate, on bulk tissue and subsequent derivation of the optical coefficients by applying a model of light propagation. Some of the techniques which are being investigated for quantitative *in vivo* light dosimetry are steady state (Kienle at al., 1994; Farrell et al., 1992) and time-resolved (Patterson et al., 1991; Patterson et al., 1989) diffuse reflectance and interstitial fluence rate measurements (Lilge & Wilson, 1993; Driver et al., 1991; Arnfield et al., 1990, 1989).

Diffuse reflectance techniques have the advantage of non-invasive determination of the optical properties of tissue *in vivo*. The fundamental assumptions of both steady-state and time-resolved techniques are that the tissue is homogeneous and optically semi-infinite, the source and detectors are small compared with the their separation (Patterson et al., 1991) and scattering dominates absorption. The primary restrictions are the signal strength and the tissue size and geometry. For deep-seated targets located several centimetres below the tissue surface, the optical properties can be determined more efficiently using the interstitial measurement technique, which is introduced in the next section.

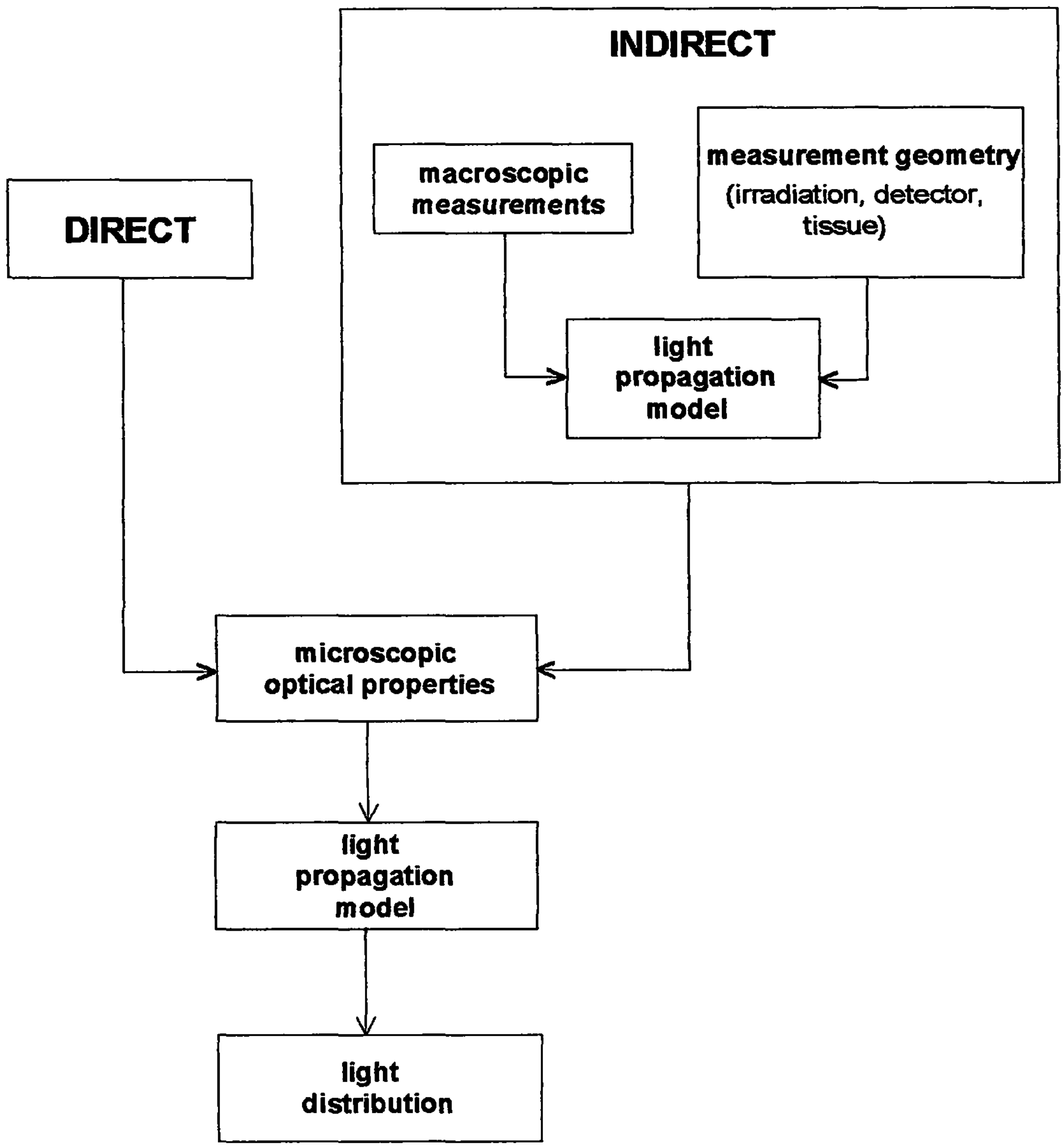

Figure 1.3 Elements of light treatment planning for PDT (Wilson et al., 1987).

1.3 Interstitial measurement technique

Quantitative *in vivo* fluence rate dosimetry can be achieved using the interstitial measurement technique (Lilge & Wilson, 1993; Driver et al., 1991; Arnfield et al., 1990, 1989). This technique involves measurement of the absolute fluence rate at two or more points in the tissue using interstitial isotropic fibre optic detectors, as shown in Figure 1.4. The optical coefficients are subsequently derived as free parameters in a non-linear fit of the measured fluence rates at the known detector positions to the predictions of a model of light propagation. The forward calculation of the fluence rate distribution throughout the tissue volume is then achieved using the derived optical coefficients and a model of light propagation such as diffusion theory or Monte Carlo models, discussed in the next two chapters.

Although diffusion theory models are typically used in solving the inverse problem of deriving the optical properties and for the forward calculation of the fluence rate distribution throughout the tissue volume, these models assume simple, homogeneous tissue geometries, possibly oversimplifying the clinical situation of tissue heterogeneities and boundaries. The validity of these models in confined volumes, where the effect of boundaries may be significant, needs to be evaluated by comparison with more accurate numerical methods such as Monte Carlo calculations. The accuracy of the derived optical properties is dependent not only on the validity of the diffusion model but also on uncertainties introduced by the experimental procedure. Sources of error include detector calibration and positioning and the influence of the detectors on the light field (Lilge & Wilson, 1993; Driver et al., 1991; Arnfield et al., 1990, 1989). The utility of the interstitial measurement technique as a tool for quantitative *in vivo* dosimetry relies on quantification of and correction for these errors. A detailed description of this technique and previous studies which have influenced this work is presented in Chapter 4.

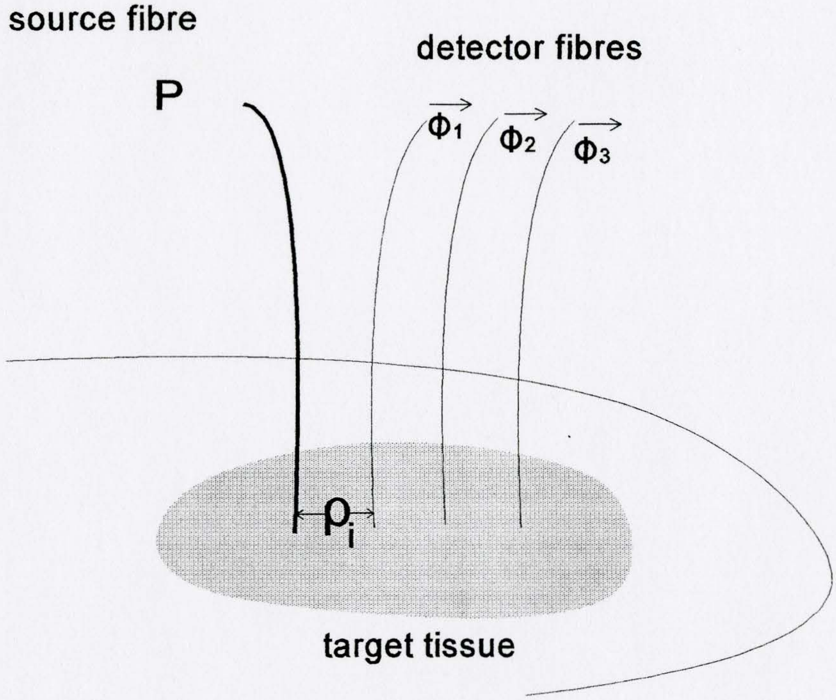

Figure 1.4 Alignment of optical fibres interstitially to determine the optical properties from multiple point fluence rate measurements. P is the delivered power and Φ_i is the fluence rate at known distances, ρ_i, from the point source (Lilge & Wilson, 1993).

1.4 Project Proposal

In preclinical *in vivo* studies, small animal models are used to simulate the biological situation in man to enable investigation of the efficiency of light and laser applications in medicine. In these studies, interstitial measurements in confined areas such as the cranial cavity of rodent models may be influenced by the presence of boundaries. The goals of this study are to investigate the influence of realistic finite geometries and variable boundary conditions on the interstitial fluence rate measurements and to quantify the systematic errors in the derived optical properties.

A Monte Carlo model is developed to predict the fluence rate distribution in the plane containing the source, and is verified by comparison with diffusion theory solutions in infinite and semi-infinite media. Two source-detector arrays, linear and spiral arrangements of the detector probes relative to the source fibre, are used in the measurements in infinite and semi-infinite media to determine their influence on the accuracy of the derived optical properties.

Interstitial fluence rate measurements are made in finite spherical volumes with two boundary conditions, absorbing and diffuse reflecting boundaries. These fluence rate measurements are compared with Monte Carlo simulations to enable quantification of the systematic errors in the measurements and the magnitude of the boundary effect is determined by evaluating the accuracy of the derived optical coefficients. Additional measurements are done in a rodent skull to determine the effect of complex boundaries on the accuracy of the derived optical properties.

The mathematical models of light propagation which were utilized in this study, diffusion theory and Monte Carlo models, are discussed in Chapters 2 and 3, respectively. Experimental methods are described in Chapter 4, results and discussion are presented in Chapter 5 and the conclusions in Chapter 6.

Chapter 2

Models of light propagation

2.1 Introduction

Electromagnetic wave theory, which accounts for the absorption and scattering properties of a material in terms of its dielectric properties, can be used as a rigorous, mathematical description of light propagation in random, turbid media (Wilson & Patterson, 1986: Ishimaru, 1989; Wilson & Jacques, 1990). However, inhomogeneities in the dielectric properties of the medium which lead to complex mathematical equations (Ishimaru, 1989) and an unavailability of data for the various tissue types, make this approach to modelling light transport in tissue impractical (Cheong et al., 1990). Alternatively, radiation transport theory, from which clinically useful approximate analytical and numeric models have been derived, is used .

It is useful at this point to define the quantities which will be used throughout this thesis. The quantities of fundamental interest in light dosimetry are the radiance, $\psi(\mathbf{r},\Omega)$ and the radiant energy fluence rate, $\Phi(r)$. The radiance at a given point, as defined in equation 2.1, is the radiant power dP passing through that point and propagating within the solid angle $d\Omega$ in a direction Ω, per unit solid angle and per unit area oriented normal to the direction of propagation (Svaasand, 1984; Sutter, 1989).

$$\Psi(\boldsymbol{r},\Omega) = \frac{dP}{d\Omega \cdot d\boldsymbol{A}} \tag{2.1}$$

In clinical applications of low intensity light such as photodynamic therapy, the biological end-point is a result of the absorption of light in tissue (Arnfield, 1988; Star et al., 1987). Hence, the radiant energy fluence rate is the fundamental dosimetric quantity since its product with the absorption coefficient yields the energy absorbed per unit time per unit volume (Star & Marijnissen, 1987). The fluence rate, $\Phi(r)$, defined as the flux of energy onto an infinitesimally small sphere divided by the cross-sectional area of that sphere, is found by integrating the radiance over the 4π solid angle (equation 2.2). This is the physical quantity which is measured in the experimental part of this thesis.

$$\Phi(\boldsymbol{r}) = \int_{4\pi} \Psi(\boldsymbol{r},\Omega)\, d\Omega \tag{2.2}$$

As discussed in Chapter 1, the primary interactions of light photons in turbid media are absorption and scattering. Tissue is, therefore, characterized by absorption and scattering coefficients, μ_a and μ_s, which represent the probabilities per unit pathlength for absorption and scattering , respectively (Wilson et al., 1987). Other useful quantities for describing the propagation of photons are the total interaction coefficient, μ_t (= $\mu_a + \mu_s$), and its inverse, the mean free path (mfp = $1/\mu_t$), the average distance travelled by a photon between interactions. The phase function, S(Ω', Ω), describes the angular distribution of scattering for a single scattering event and when normalized, as shown in equation 2.3, it represents the probability density function for scattering from direction Ω' into Ω (Cheong et al.,1990).

$$\int_{4\pi} S(\Omega',\Omega)\, d\Omega = 1 \qquad (2.3)$$

Assuming that the probability of scattering is a function only of the angle between the two directions Ω'and Ω (Prahl, 1988; Ishimaru, 1989), the phase function can be written:

$$S(\Omega',\Omega) = S(\Omega'\cdot\Omega) = S(\cos\theta) \qquad (2.4)$$

Jacques *et al* (1987) have demonstrated that the Henyey-Greenstein (HG) phase function, first proposed by Henyey & Greenstein(1941), is a reasonable description of the phase function observed in a range of tissues. The HG probability density function for scattering is given by :

$$S(\theta) = \frac{1-g^2}{(1+g^2-2g\cos\theta)^{3/2}} \cdot \frac{1}{2} \qquad (2.5)$$

where the anisotropy parameter, g, is given by :

$$g = \int S(\theta)\cos\theta\, d(\cos\theta) = \langle \cos\theta \rangle \qquad (2.6)$$

2.2 Radiation transport theory

The fundamental assumption of radiation transport theory is that wave effects, such as diffraction and polarization, may be ignored and light photons may be treated as neutral particles (Wilson & Patterson, 1986). Assuming steady state conditions and elastic scattering, the time-independent, single energy group radiative transfer equation for the radiance can be written as (Groenhuis, 1983; Profio, 1989) :

$$\nabla\cdot\Psi(\boldsymbol{r},\Omega) = -\mu_t(\boldsymbol{r})\Psi(\boldsymbol{r},\Omega) + \int_{4\pi}\mu_s\, S(\Omega',\Omega)\,\Psi(\boldsymbol{r},\Omega')\,d\Omega' + Q(\boldsymbol{r},\Omega) \qquad (2.7)$$

where

$\Psi(r,\Omega)$ = radiance at a point r in the direction Ω ($Wm^{-2}sr^{-1}$)

μ_t = total interaction coefficient (m^{-1})

= $\mu_a + \mu_s$

μ_a = absorption coefficient (m^{-1})

μ_s = scattering coefficient (m^{-1})

$S(\Omega', \Omega)$ = phase function describing the angular distribution of light scattered from direction Ω' into direction Ω

$Q(r,\Omega)$ = volume source density ($Wsr^{-1}m^{-3}$)

The transport equation is derived by balancing the losses and gains of photons from an arbitrary volume (Duderstadt & Hamilton, 1976; Profio & Doiron, 1981). The first term on the right hand side of equation 2.7 represents the losses from the radiance at point r in the direction Ω due to photons being absorbed and scattered out of this direction. The integral describes the gain from scattering of photons into direction Ω from other directions and the term $Q(\mathbf{r},\Omega)$ is representative of any volume source present in the medium.

Exact analytic solutions of the transport equation are possible only for simple geometries and source distributions. Typically, approximate analytic models, such as diffusion theory (Duderstadt & Hamilton, 1976) and Kubelka-Munk models (Kubelka, 1948) and numeric methods, such as Monte Carlo (Wilson & Adams, 1983) and discrete ordinates (Profio & Doiron, 1987), are used to describe the light distribution in turbid media.

2.3 Diffusion theory

The diffusion theory or P1 approximation to the radiative transfer equation (Duderstadt & Hamilton, 1976) is obtained by truncating the expansion of the radiance in Legendre polynomials after the first two terms i.e. l =0 and l =1 terms, representative of an isotropic and a forward directed term (Cheong et al., 1990). The general time-independent diffusion equation as derived by Duderstadt & Hamilton (1976) is written as :

$$-D\, \nabla^2 \cdot \Phi(\boldsymbol{r}) + \mu_a \Phi(\boldsymbol{r}) = Q(\boldsymbol{r}) \tag{2.8}$$

where $\Phi(r)$ is the fluence rate and $Q(r)$ represents the source term if one is present. The diffusion coefficient, D, which incorporates a correction for anisotropic scattering, is given by :

$$D = \frac{1}{3[\mu_a + \mu_s(1-g)]} \tag{2.9}$$

The fundamental assumptions of this derivation are that the radiance is only linearly anisotropic, sources emit isotropically and conditions are steady state. Furthermore, it is assumed that the optical coefficients are independent of position in the medium. The first assumption necessarily implies that the diffusion approximation is not valid within several transport mean free paths {mfp' = $1/\mu_t'$ = $1/(\mu_a + \mu_s')$} of sources or boundaries and in media where absorption dominates scattering ($\mu_a \geq \mu_s(1-g)$).

Solution of the diffusion equation requires (a) characterization of the source terms and (b) specified boundary conditions (Wilson & Patterson, 1986; Farrell & Patterson, 1992). Exact solutions of the transport equation in the diffusion approximation for infinite and semi-infinite geometries, which have been empirically determined to be accurate, are presented below.

2.3.1 Infinite geometry

The diffusion equation for an isotropic emitting point source at the origin of an infinite medium, can be written for spherical geometry as (Duderstadt & Hamilton, 1976):

$$\frac{1}{r^2}\frac{d}{dr} r^2 \frac{d\Phi}{dr} - \mu_{eff}^2 \, \Phi(r) = 0 \,, \qquad r > 0 \tag{2.11}$$

where

$$\mu_{eff} = \sqrt{3\,\mu_a\,(\,\mu_a + \mu_s'\,)} \tag{2.12}$$

The general solution for equation (2.11) is:

$$\Phi\,(r) = \frac{A\, e^{-\mu_{eff}\, r}}{r} + \frac{B\, e^{\mu_{eff}\, r}}{r} \tag{2.13}$$

and the constants A and B can be solved for by applying the boundary conditions,

(i) $$\lim_{r \to 0} \; 4\,\pi\, r^2 J\,(r) = S_0$$

where the current density, $J(r) = -D\, \nabla\, \Phi(r)$ and

(ii) $$\lim_{r \to \infty} \Phi\,(\,r\,) < \infty\,.$$

The second condition implies that B = 0 and the first implies that $A = S_0/4\pi D$ so that the solution to the diffusion equation for a point isotropic source in an infinite medium is

$$\Phi(r) = \frac{S_0}{4\pi r D} e^{-\mu_{eff} r} \tag{2.14}$$

The above solution can be modified for anisotropic delivery by replacing an anisotropic source at a depth z in the medium with an isotropic source at a depth $z + 1/\mu_s'$, if it is assumed that the light distribution is approximately isotropic after one effective scattering pathlength (Patterson et al., 1991, Lilge & Wilson, 1993)).

An alternative solution of the diffusion equation for an isotropic point source in an infinite medium is that derived by Grosjean (1956) which is given as (Lilge & Wilson, 1993):

$$\Phi(r) = \frac{P}{4\pi}\left(\frac{1}{Dr}\frac{\mu_s'}{2\mu_a + \mu_s'} e^{-\mu_{eff(g)} r} + \frac{1}{r^2} e^{-\mu_t' r}\right) \tag{2.15}$$

where

$$\mu_{eff(g)} = \sqrt{3\mu_a(\mu_a + \mu_s')\frac{\mu_a + \mu_s'}{2\mu_a + \mu_s'}} \tag{2.16}$$

and $\mu_t' = \mu_a + \mu_s'$. This solution is derived in a manner similar to that of the diffusion equation (i.e. from an approximation to the radiation transport equation). Compared with the diffusion solution of equation 2.14, the source term of equation 2.15 is multiplied by the factor $\mu_s'/2\mu_a + \mu_s'$ and μ_{eff} has the additional factor $\mu_a + \mu_s'/2\mu_a + \mu_s'$. While there is no difference between this solution and diffusion theory for high transport albedos ($\mu_s'/\mu_a + \mu_s' \approx 1$), the fluence rate distribution is predicted accurately by equation 2.15 for media with comparable absorption and scattering, as will be discussed in Chapter 5.

2.3.2 Semi-infinite geometry

The diffusion model presented in this section is a solution of the general diffusion equation for a point isotropic source in a semi-infinite medium with isotropic scattering (Farrell & Patterson, 1992). This model takes into account refractive index matched and mis-matched boundaries between a turbid and a non-scattering medium and satisfies these boundary conditions using a negative image source approach (Eason et al, 1978). A refractive index matched boundary implies that there is no photon current back into the medium while a mis-match at the interface requires incorporation of the internal reflection at the boundary.

Either boundary condition can be satisfied by forcing the fluence rate to zero at an extrapolated boundary at a height z_b above the surface via the introduction of a negative image source above the boundary (see Figure 2.1) where

$$z_b = 2AD \tag{2.17}$$

The internal reflection parameter, A, can be derived from the Fresnel reflection coefficients. Alternatively, Groenhuis et al. (1983) have adopted an empirical approach in which A is calculated according to :

$$A = \frac{1+r_d}{1-r_d} \tag{2.18}$$

where r_d (equation 2.17) is derived from a curve fit for the internal reflection due to perfectly diffuse radiation (Egan & Hilgeman, 1979).

$$r_d = -1.440 n_{rel}^{-2} + 0.710 n_{rel}^{-1} + 0.668 + 0.0636 n_{rel} \tag{2.19}$$

where the relative refractive index, $n_{rel} = n_{med}/n_{ext}$ (n_{med} and n_{ext} are the refractive indices of the medium of interest and the external medium, respectively). Since there is no internal reflection at a matched boundary, this corresponds to A =1. The solution for the fluence rate at a point (r,z) due to a point isotropic source at $(0,z_0)$ (i.e. at a depth z_0 below the surface), as shown in Figure 2.1, is given as

$$\Phi(r) = \frac{1}{4\pi D}\left(\frac{e^{-\mu_{eff} r_1}}{r_1} - \frac{e^{-\mu_{eff} r_2}}{r_2}\right) \tag{2.20}$$

where r_1 and r_2 which represent the radial distances from the point (r,z) to the real and image sources, respectively, are given by :

$$r_1 = \sqrt{(z-z_0)^2 + r^2}$$

and

$$r_2 = \sqrt{(z+z_0+2z_b)^2 + r^2}$$

2.4 Monte Carlo

As discussed in the previous section diffusion theory yields solutions for the fluence rate for simple, homogeneous media and is accurate only if scattering dominates absorption and in regions distant from sources and boundaries. These limitations make numerical techniques such as Monte Carlo preferable, as in addition to requiring no further assumptions to those of radiative transfer, light distributions in heterogeneous media, finite volumes and complex geometries can be modelled. Monte Carlo calculations adopt a statistical approach to solving the transport equation and as such are limited only by the statistical uncertainties arising from the tracing of a finite number of photon histories.

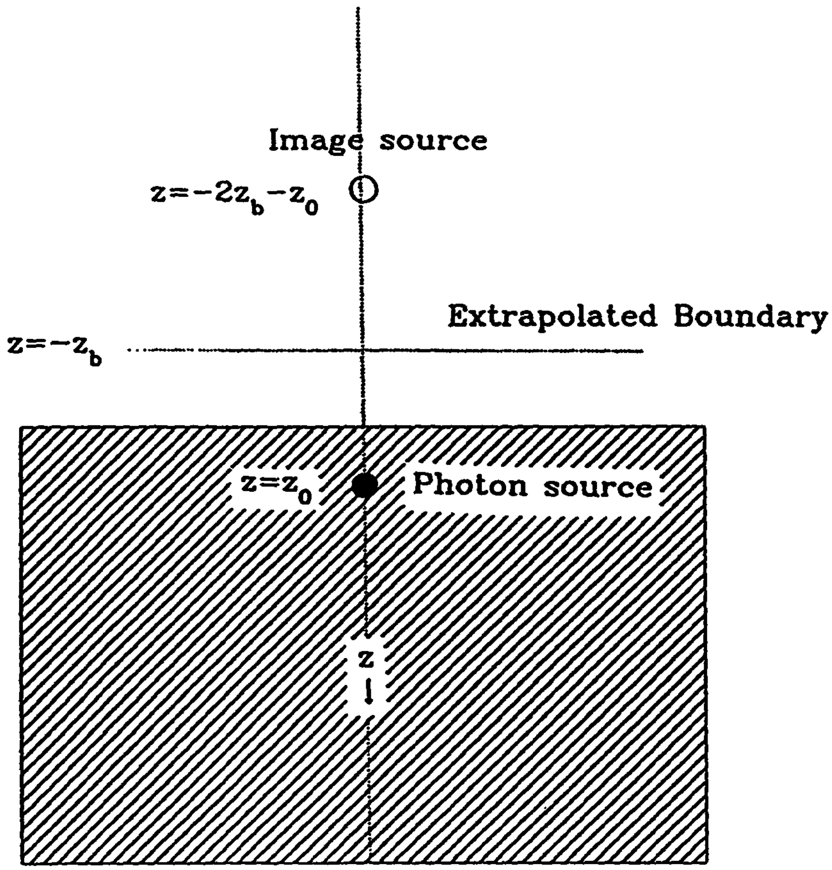

Figure 2.1 Negative image source (Farrell & Patterson, 1992)

Chapter 3

Monte Carlo Modelling

3.1 Introduction

The Monte Carlo model, first developed by Metropolis and Ulam, adopts a statistical approach to the modelling of physical and mathematical problems, for which analytic solutions may be cumbersome or non-existent (Metropolis & Ulam, 1949; Raeside, 1976). The primary advantage of this method for simulating light transport in optically turbid media is its versatility in modelling realistic source-detector geometries, tissue heterogeneities, finite geometries and media with comparable absorption and scattering. Utilization of fast computers and variance reduction techniques, as discussed below, enables tracing of large numbers of photon histories in acceptable computation times (Key et al.,1991).

3.2 Monte Carlo code

The Monte Carlo method, within its statistical nature, yields exact solutions of the radiation transport equation by tracing photon histories using randomly sampled variables. These variables such as the photon step size and scattering angle, are selected from the relevant probability distributions, described below. Figure 3.1 is a flowchart of the basic Monte Carlo code (Wang & Jacques, 1993; Prahl et al.,1989) used in this study. The random variables and the variance reduction and scoring techniques utilized are discussed in the rest of this chapter.

The code was adapted from a code written in BASIC by Farrell & Patterson (1992) and was translated into FORTRAN 77 and simulations were run on a Sun SPARCstation 10. The modifications to the code included scoring of the photon fluence rate in arbitrary planes in the medium rather than the diffuse reflectance at the surface. Realistic isotropic and anisotropic delivery were also incorporated into the code. Typically 10^5 photon histories were traced for the infinite, semi-infinite and finite media investigated. Run times ranged from less than 15 minutes to 50 hours for absorption dominated ($\mu_a/\mu_s' \sim 10$) and highly scattering media ($\mu_a/\mu_s' \sim 10^{-3}$), respectively. Typical run times for media with optical properties simulating soft tissue ($\mu_a/\mu_s' \sim 10^{-1}$ - 10^{-2}) ranged from 30 minutes to 1 hour.

3.2.1 Random Sampling

The fundamental requirement for all Monte Carlo calculations is a reliable supply of random numbers (Raeside, 1976). Instead of using true random numbers which do not facilitate reproducible results, computer-generated sequences of pseudo-random numbers, uniformly distributed on the unit interval, are used (Knuth, 1981). The random number generator utilized in this study was the Fortran77 random number generator which was initialized by input of a seed at the beginning of each simulation.

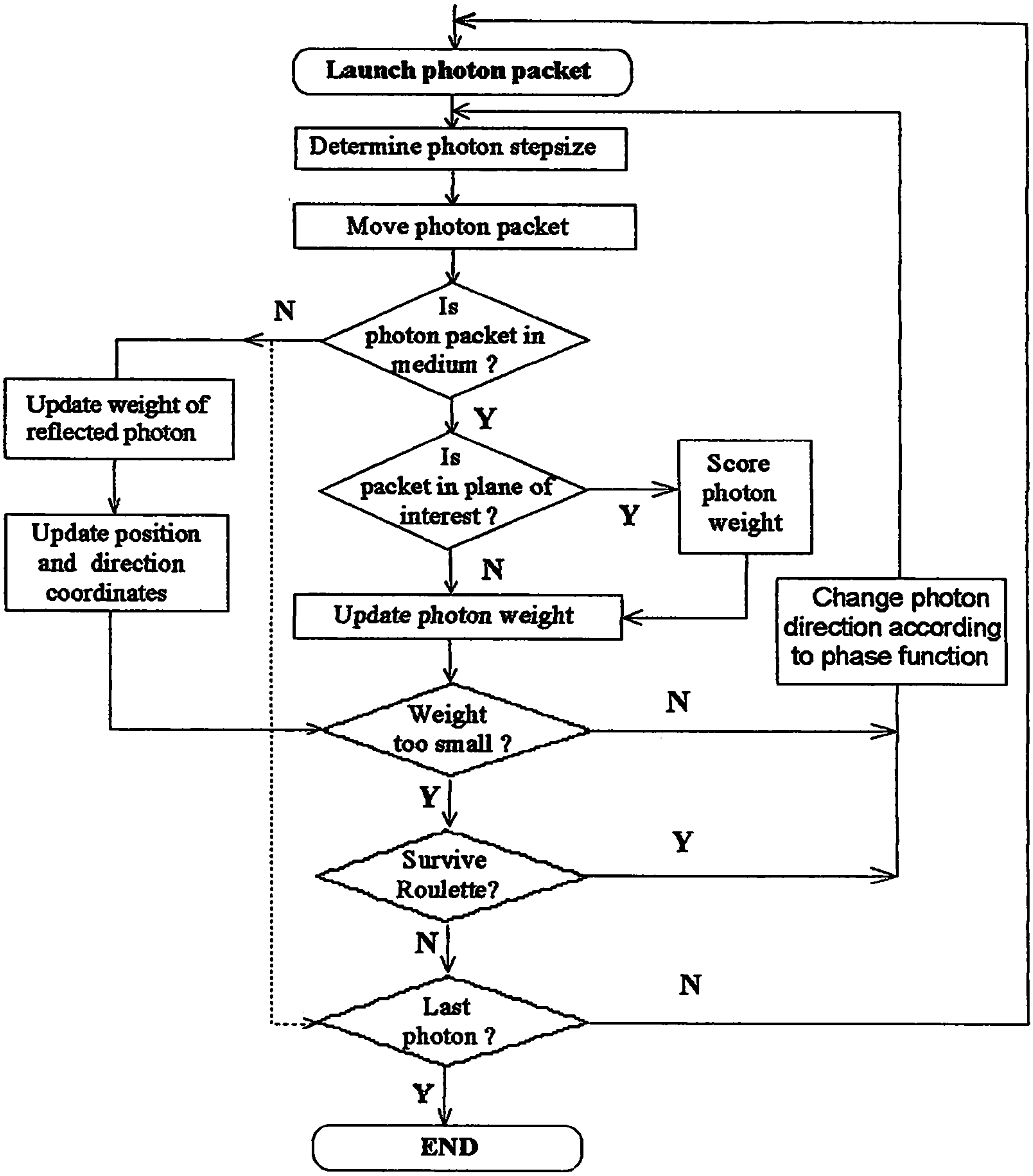

Figure 3.1 Flowchart of Monte Carlo code. The dotted line represents the case of a refractive-index-matched boundary (Wang & Jacques, 1993; Prahl et al., 1989).

3.2.1.1 Random Number Generator Tests

A number of random number generator (rng) tests were performed to assess the suitability of the Fortran77 rng for the Monte Carlo simulations. These included tests for correlation, uniformity on the unit interval and serial association. The correlation test checks for independence in a sequence of random numbers. Table 3.1 illustrates that the values expected for an uncorrelated sequence of numbers are not statistically different from the observed values for sequences of 10^5 and 10^6 random numbers, respectively. These results imply that the choice of any random number is independent of the other numbers in the sequence.

Table 3.1 Results of serial correlation test (R_i, R_j and R_k are successive random numbers in the sequence)

Quantity	Expected values (uncorrelated sequence)	Observed values	
		10^5	10^6
$<R_i>$	0.500	0.499714	0.500242
$<R_iR_i>$	0.333	0.332659	0.333431
$<R_iR_iR_i>$	0.250	0.249163	0.250037
$<RiRj>$	0.250	0.249172	0.250110
$<R_iR_jR_k>$	0.125	0.124646	0.125172

Uniformity on the unit interval, a primary requirement of random number generators for Monte Carlo applications, is assessed by applying the equidistribution or frequency test (Knuth, 1981). For this test 10^5 random numbers are binned into 100 subintervals on the (0,1) interval. Figure 3.2 illustrates that there is a random fluctuation of the frequency in each cell about the expected frequency of 1000, which is what one expects for a uniform distribution of random numbers. The statistical significance of the results of this test are determined by calculating a chi-square test statistic with 99 degrees of freedom according to :

$$\chi_{freq}^{2} = \frac{k}{N} \cdot \sum_{i=1}^{k} \left(W_i - \frac{N}{k}\right)^2 \tag{3.1}$$

where the number of subintervals, k = 100; the sample size, N = 10^5 and W_i is the frequency in each cell. The empirically derived reduced chi-square, χ_v^2, is determined to be 1.0017 which corresponds to a probability of approximately 0.5. This is consistent with a random sample in which the observed values are expected to be larger than the norm 50% of the time (Bevington, 1969).

Serial association between the digits of successive pairs of numbers in a sequence of 10^5 random numbers is checked by performing the serial test. This is essentially a two dimensional frequency test in which the digits are selected by normalizing to the (0,k) interval. The experimental chi-square value with k^2 - 1 degrees of freedom was calculated according to:

$$\chi^2_{ser} = \frac{k^2}{N} \sum_{i,j} (W_{i,j} - \frac{N}{k^2})^2 \tag{3.2}$$

where $W_{i,j}$ is the frequency in each cell, N is the sample size of 50 000 pairs and k = 10. The experimental reduced chi-square value was is calculated to be 1.00608. As in the uniformity test described above, this implied a probability of approximately 0.5 so that the sequence is demonstrated to be random. On the basis of the results of these tests, the Sun Fortran77 random number generator appeared to satisfy the fundamental requirements of an rng to be used in Monte Carlo calculations (Knuth, 1981, Turner et al., 1985).

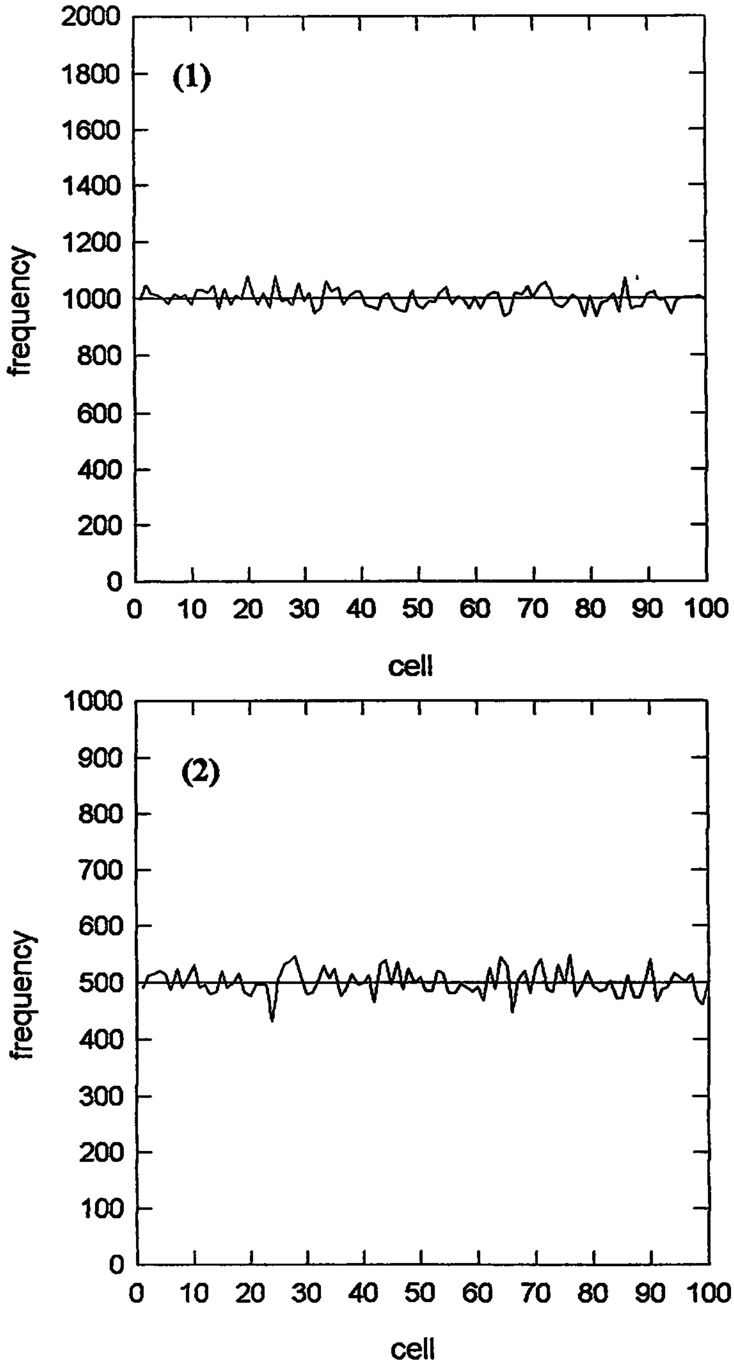

Figure 3.2 Results of 1) equidistribution test and 2) serial test on a sequence of 10^5 random numbers.

3.2.2 Photon Initialization

The location of a photon within a turbid medium is described by three Cartesian coordinates (x, y, z) for its spatial position and three cosines (μ_x, μ_y, μ_z) for its direction of travel. The direction of travel can be specified with spherical coordinates, a deflection angle θ and an azimuthal angle ϕ. However, it is advantageous to use Cartesian coordinates since in this coordinate system the direction cosines do not change along the flight path of the photon between scattering events (Carter & Cashwell, 1975; Prahl et al., 1989). Figure 3.3 illustrates the coordinate systems used to trace the photon within the medium.

The photon history begins at (0,0,0) with direction cosines (0,0,-1) such that the initial photon direction is downward into the medium. Simulation of realistic, imbedded isotropic and anisotropic source distributions require selection of a new set of direction cosines. The isotropic source simulated is an 800 μm spherical scattering tip attached to a 400 μm cut-end fibre, so that photons are not launched from within the solid angle, Ω, shown in Figure 3.4.1. For anisotropic delivery (see Figure 3.4.2), a 320 μm core cut-end fibre is used so that the launch angles are restricted by the numerical aperture (NA =0.22) of the fibre.

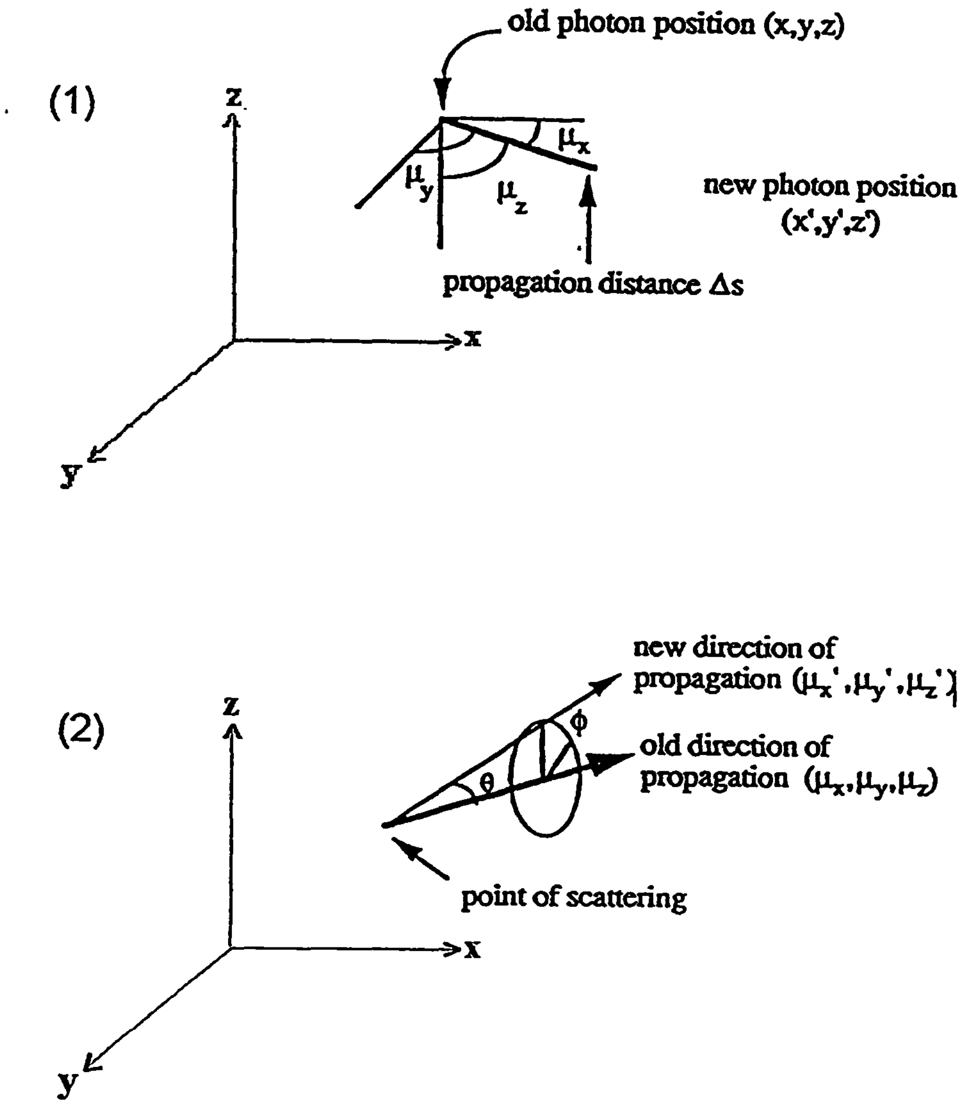

Figure 3.3 Coordinate systems (1) Cartesian coordinates - position and direction cosines. (2) Scattering angles (θ, ϕ) (Prahl, 1988)

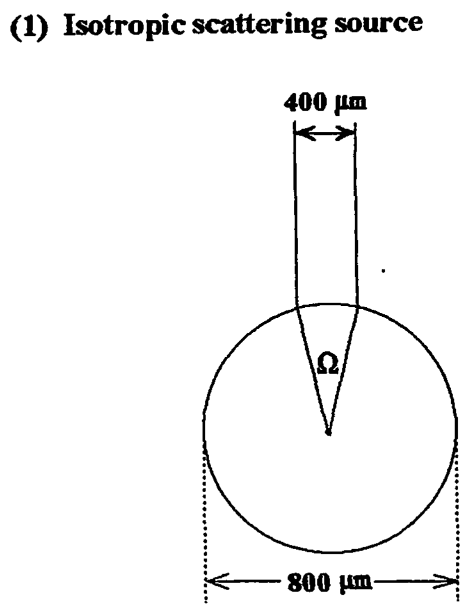

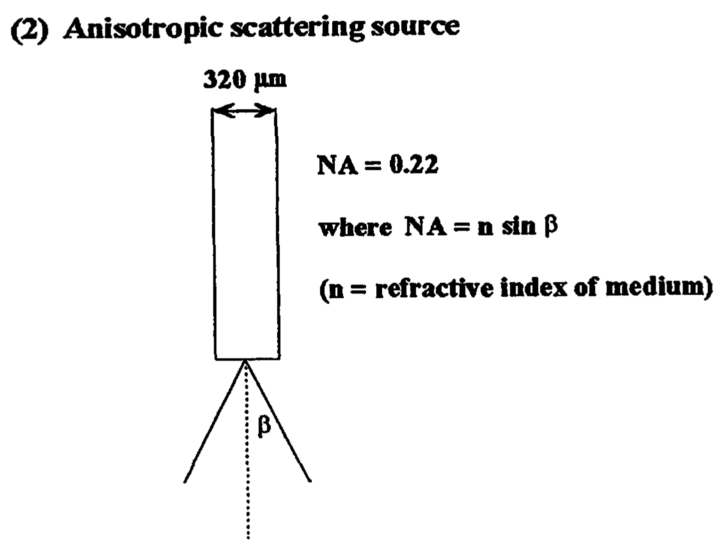

Figure 3.4 Geometry of source distributions: (1) isotropic and (2) anisotropic delivery

3.2.3 Scattering of photons

At each interaction point the photon weight is updated, as discussed in the next section, and the photon undergoes a scattering event. The scattering angles, specifically the deflection angle, θ where $0 \le \theta \le \pi$ and the azimuthal angle, ϕ where $0 \le \phi \le 2\pi$, are determined by random sampling. For isotropic scattering, the anisotropy parameter, g = $\langle \cos\theta \rangle = 0$, and the deflection angle is calculated as :

$$\cos(\theta) = 2\xi - 1 \tag{3.3}$$

where ξ is a uniformly distributed pseudo-random number on the unit interval. The Henyey-Greenstein phase function (Henyey & Greenstein, 1941), discussed in the previous chapter, is used to describe non-isotropic scattering. In this case, given the anisotropy parameter, g, the deflection angle is calculated as (Wang & Jacques, 1993; Prahl et al., 1989):

$$\cos\theta = \frac{1}{2g}\left\{ 1 + g^2 - \left(\frac{1 - g^2}{1 - g + 2g\xi}\right)^2 \right\} \tag{3.4}$$

(see equation 2.5) and the azimuthal angle is given by :

$$\phi = 2\pi\xi \tag{3.5}$$

Using the pair of randomly selected variables (θ, ϕ), the direction cosines can be updated according to :

$$\mu_x' = \frac{\sin\theta}{\sqrt{(1-\mu_z^2)}}(\mu_x\mu_z\cos\phi - \mu_y\sin\phi) + \mu_x\cos\theta \tag{3.6a}$$

$$\mu_y' = \frac{\sin\theta}{\sqrt{(1-\mu_z^2)}}(\mu_y\mu_z\cos\phi - \mu_x\sin\phi) + \mu_y\cos\theta \tag{3.6b}$$

$$\mu_z' = -\sin\theta\cos\phi\sqrt{1-\mu_z^2}\,(\mu_y\mu_z\cos\phi - \mu_x\sin\phi) + \mu_z\cos\theta \tag{3.6c}$$

Alternatively, if the photon direction is too close to the normal, i.e. $|\mu_z| > 0.9999$, for these formulae to be numerically accurate, equations (3.6.a) - (3.6.c) can be simplified so that the direction cosines are computed as:

$$\mu_x' = \sin\theta\cos\phi \tag{3.7a}$$

$$\mu_y' = \sin\theta\sin\phi \tag{3.7b}$$

$$\mu_z' = \frac{\mu_z\cos\theta}{|\mu_z|} \tag{3.7c}$$

3.2.4 Photon Propagation

The photon step-size, the distance travelled by a photon before undergoing an interaction, is calculated using random sampling from a probability distribution for the step size (Prahl et al., 1989). Since this distribution follows Beer's law, the step-size is calculated according to :

$$s = \frac{-\ln \xi}{\mu_t} \tag{3.8}$$

where μ_t is the total interaction probability and ξ is a pseudo-random number uniformly distributed on the unit interval (0,1). Once the step size has been determined, the photon position is updated according to (Figure 3.3.1) :

$$x' = x + \mu_x s \tag{3.9a}$$

$$y' = y + \mu_y s \tag{3.9b}$$

$$z' = z + \mu_z s \tag{3.9c}$$

3.2.5 Photon absorption

At each interaction point, the photon has a probability of undergoing an absorption or scattering event. A technique commonly used for reducing variance, called implicit capture (Prahl, 1988; Hendricks & Booth, 1983), propagates a photon packet of weight

W, initially set to 1. At the ith interaction point, a fraction of the photon weight,

$$\Delta W = \frac{\mu_a}{\mu_t} W_i \tag{3.10}$$

is absorbed and the photon packet continues propagation with an updated weight (Wilson & Adam, 1983),

$$W_{i+1} = (1 - \frac{\mu_a}{\mu_t}) W_i \tag{3.11}$$

or

$$W_{i+1} = \frac{\mu_s}{\mu_t} W_i \tag{3.12}$$

This technique provides better statistics with the propagation of fewer input photons since tracing does not end at an absorption event, but continues with a photon packet with reduced weight.

3.2.6 Internal Reflection

In finite and semi-infinite media, the effect of boundaries on incident photon packets must be taken into consideration. A photon packet crossing a refractive index matched boundary to a non-scattering medium is terminated since the photon packet will not be able to re-enter the medium of interest. For a photon packet incident on a boundary at which there is a refractive index mis-match to a non-scattering medium, the packet is split with a fraction of the weight being transmitted and the remainder internally reflected. This approach, called implicit photon capture, is another technique used to improve the variance of the scored reflectance and transmittance. The weight and the direction of the photon packet must be updated before propagation can continue. The probability of the packet being internally reflected is calculated according to Fresnel's law (see equation 3.16), and the weight of the packet is updated by that probability.

3.2.6.1 Boundary conditions in semi-infinite media

The semi-infinite geometry used is a medium infinite in the x and y directions and finite in the positive z direction, as shown in Figure 3.5. The origin of the Cartesian coordinate system is at a distance, τ, below the surface of the medium. The weight and direction cosines of a packet crossing the boundary of the medium, i.e. a packet for which $z > \tau$, has to be updated as described above. For this planar geometry, the angle of incidence is related to μ_z by :

$$\theta_i = \cos^{-1}(\mu_z) \tag{3.13}$$

and the angle of transmission, θ_t, is given by :

$$n_i \sin\theta_i = n_t \sin\theta_t \tag{3.14}$$

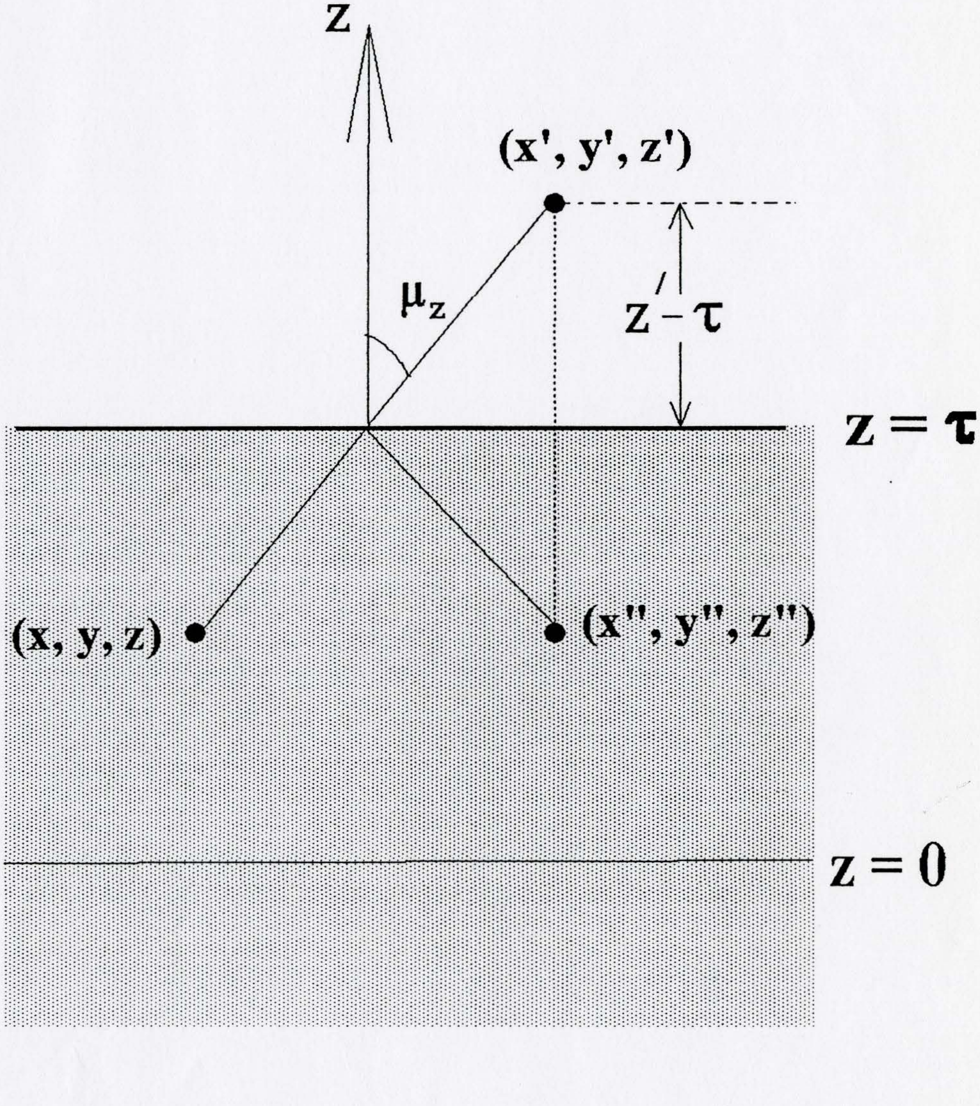

Figure 3.5 Internal reflection of photon packet in semi-infinite geometry (Prahl, 1988)

where n_i and n_t are the indices of refraction of the scattering and non-scattering media, respectively. Assuming unpolarized light, for angles of incidence greater than the critical angle, $\sin^{-1}(n_t/n_i)$, the Fresnel reflection coefficient is given by:

$$R(\theta_i) = 1 \tag{3.15}$$

while for smaller angles, the probability of internal reflection is calculated according to the Fresnel equation :

$$R(\theta_i) = \frac{1}{2}\left[\frac{\sin^2(\theta_i - \theta_t)}{\sin^2(\theta_i + \theta_t)} + \frac{\tan^2(\theta_i - \theta_t)}{\tan^2(\theta_i + \theta_t)}\right] \tag{3.16}$$

The photon weight, W, is then updated by :

$$W = W \cdot R(\theta_i) \tag{3.17}$$

and the spatial coordinates of the internally reflected packet (x", y", z") are given by

$$(x'', y'', z'') = (x', y', 2\tau - z') \tag{3.18}$$

where (x', y', z') are the coordinates of the transmitted photon packet. The direction cosines are updated by leaving μ_x and μ_y unchanged and reversing the z component so that the new direction of the photon packet is $(\mu_x, \mu_y, -\mu_z)$.

3.2.6.2 Boundary conditions in finite spherical volume

The Monte Carlo code used in the finite volume modelling is essentially the same as that used in the simulations of light propagation in the semi-infinite geometry described previously. In this instance, however, the boundaries are considered to be diffusely reflecting since this is a realistic approximation of realistic tissue boundaries. A photon packet crossing the spherical boundary is moved back to the boundary by retracing its photon path until it has reached the boundary, after which a new set of direction cosines are obtained by random sampling of a new pair of scattering angles (θ, ϕ), such that the packet is re-directed back into the medium. The weight of the photon packet is updated by:

$$W = W \cdot R_d \tag{3.19}$$

where R_d is the total diffuse reflectance of the boundary. Two boundary conditions with diffuse reflectance values of 0.033 and 0.78 are modelled since these correspond to the measured total diffuse reflectance from the absorbing (black) and diffusely reflecting (white) spherical volumes, respectively, used in the experiments (as described in the next chapter).

3.2.7 Photon termination

A photon packet can undergo multiple scattering events and if propagation is allowed to continue, the weight of the photon packet approaches zero. Continued tracing of a packet with a low weight contributes very little to the scored physical quantity so, in order to minimize computation time, it is necessary to terminate tracing if the weight falls below some threshold value. A variance reduction technique called Russian roulette (Carter & Cashwell, 1975; Prahl et al., 1989), is used to terminate the photon without biasing absorption or violating energy conservation. Russian roulette gives the photon packet a probability, 1/m, of survival. If the random number selected, $\xi \leq 1/m$, the photon packet survives and its weight is updated to mW else photon tracing is terminated. Russian roulette is performed after the photons have experienced a specified number of scattering events, by which time more than 99.9% of the photon weight has been deposited in the medium.

3.2.8 Scoring of photon fluence

The physical quantity scored in these simulations is the absorbed photon weight. A one-dimensional grid, consisting of annular rings of width, Δr and thickness, t, is set up to score the absorbed photon weight in arbitrary planes in the medium (see Figure 3.6). The absorbed photon density can be calculated from the absorbed photon weight as :

$$\frac{W}{2\pi r \Delta r t} = absorbed\ photon\ density\ (photons\ cm^{-3}) \tag{3.20}$$

where t is the thickness of the bin, Δr is the bin with and r is the radial distance from the source so that $2\pi r\Delta rt$ represents the volume of the scoring bin. The bin thickness and width are chosen to be 0.1 mm in all simulations, since this resolution is compatible with the experimental measurements of the fluence rate which are made with isotropic fibre optic detectors with an outer radius 100μm. Since the product of the fluence rate and the absorption coefficient yields the energy absorbed per unit volume in the tissue (Star & Marijnissen, 1987), the fluence rate can be calculated according to:

$$\frac{W}{2\pi r \Delta r t \mu_a} = photon\ fluence\ rate\ (photons\ cm^{-2}) \tag{3.21}$$

The fluence rates are normalized to one input photon to enable comparison of simulation results with the predictions of the diffusion models discussed in the previous chapter and with the experimentally determined fluence rates (see Chapter 4).

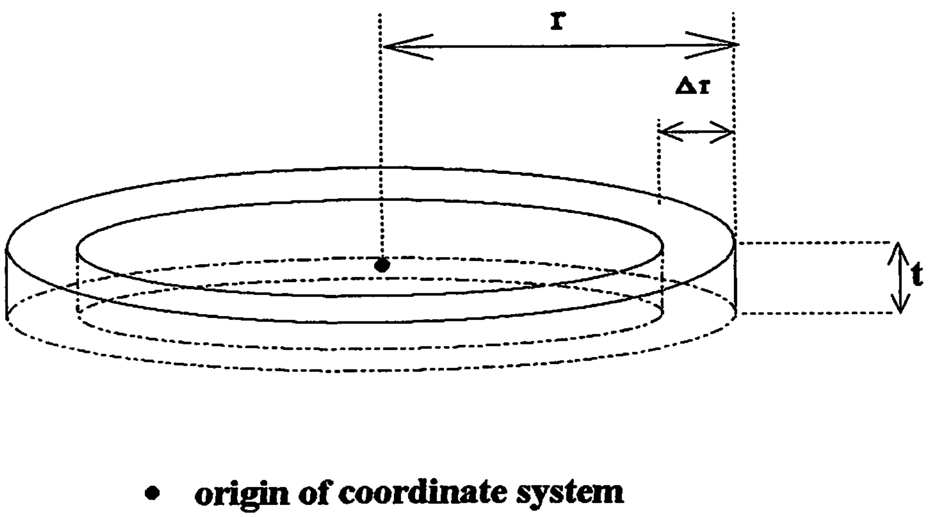

Figure 3.6 Scoring arrangement for absorbed photon weight

3.2.8.1 Infinite and semi-finite volumes

The Monte Carlo code is verified by comparison with solutions of the diffusion equation for infinite and semi-infinite media, equations (2.11) and (2.16), respectively. Simulation of photon propagation in an infinite medium, given the optical properties, entails propagation of photon packets in a medium without boundaries. The source distribution, which could be isotropic or anisotropic is located at the origin of the Cartesian coordinate system and the scoring plane is the $z = 0$ plane, i.e. the plane containing the source distribution. As discussed above, the absorbed weight of the packet is scored into a finite grid but photons are allowed to propagate beyond the grid until the weight is less than 0.0001, after which Russian roulette is performed.

In the semi-infinite medium, the source, again isotropic or anisotropic, is located at the origin which is some distance, τ, below the boundary of the medium (Figure 3.5). Both refractive index matched and mis-matched boundaries can be simulated and the scoring arrangement is as described above. In all simulations, absorbed photon weight could have been scored in arbitrary planes in the medium or in a three-dimensional grid. However, for compatibility with the experimental results, only the absorbed weight in the plane containing the source was scored.

3.2.8.2 Finite volume

As shown in Figure 3.7, the origin of the coordinate system coincides with the centre of the sphere. Simulations are run with the source, and consequently the scoring planes, located at three positions within the sphere. With the source located at the centre of the sphere (plane 1), the absorbed weight in the z = 0 plane is scored, while at 2 and 3 , the scoring planes are located at z = -15, -17 mm and z = -14.75, -16.75 mm for the black and white spheres, respectively. Planes 2 and 3 were chosen since they corresponded to distances (measured along the z axis) of 4 and 2 mm, respectively, between the source and the boundary of the sphere.

The size of the scoring grid for the semi-infinite and infinite media is typically 500 bins which corresponds to a width of 50 mm with a resolution of 10 bins/mm. The grid size for the finite spherical volume is 200 bins since the maximum radius of the scoring plane is 19 mm. Simulations are run for the three sets of optical properties (discussed in Chapter 4) in each of the two spheres, absorbing (R_d = 0.033) and diffuse reflecting (R_d = 0.78). for the three source locations described above. Results are presented in Chapter 5.

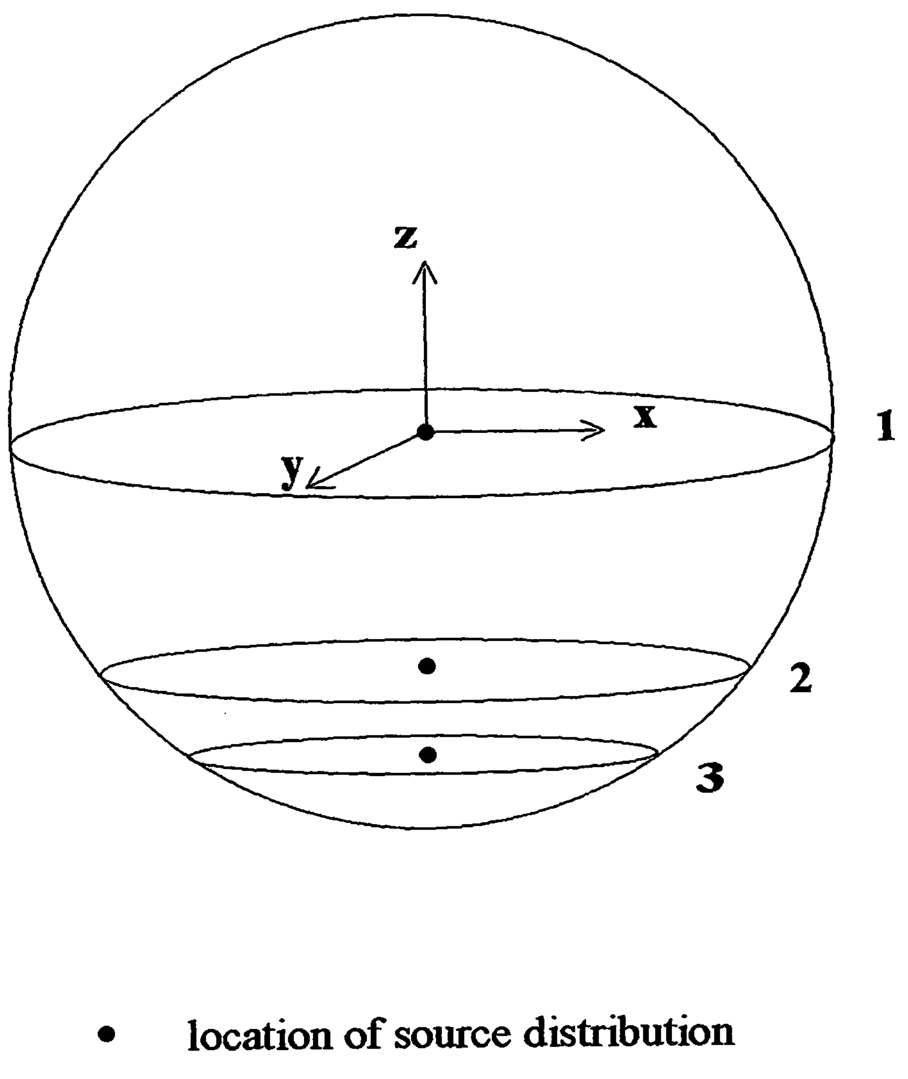

Figure 3.7 (1) Scoring planes in finite spherical volumes. Planes 1, 2 and 3 are located at z = 0, -15 and -17 mm for the black sphere and at 0, -14.75 and -16.75 mm for the white sphere.

Chapter 4

Interstitial measurements : materials and methods

4.1 Introduction

Direct measurement of the fluence rate using interstitial fibre optic detectors allows the energy deposited in the medium to be calculated, if the absorption coefficient is known. In early light dosimetry studies, the optical attenuation of light in tissue was investigated using anisotropic fibre optic detectors (Wilson & Adam, 1983; Wilson et al., 1985). Using cut-end fibre optic detectors with restricted numerical aperture, and hence anisotropic response, determination of the local fluence rate at any point in the tissue required measurement at different angular orientations about that point to compensate for the anisotropy of the radiance field. The major limitations of these studies were the restricted number of fluence rate measurements and the underestimation in the measured fluence rates as a result of limited detection of the scattered flux (Wilson et al., 1985).

The development of fibre optic detectors with isotropic response (Lilge et al., 1993, 1990; Marijnissen et al., 1985) facilitated improved light dosimetry since single measurements of the absolute fluence rate in tissue were made possible. The interstitial technique for light dosimetry is feasible for direct monitoring of the absolute fluence rate at points of interest in the tissue, as well as derivation of the tissue optical properties and subsequent calculation of the fluence rate field throughout the tissue volume of interest (Lilge & Wilson, 1993; Driver et al., 1991; Arnfield et al., 1990, 1989).

Arnfield et al. (1990, 1989) and Driver et al. (1991) have investigated this technique in biological tissue and optical phantoms and identified a number of limitations. These include the number of detectors and accuracy in positioning them. The latter was observed to cause changes of up to 30% in the measured fluence rate (Arnfield et al., 1990) while reduced optical attenuation resulted from disruption of tissue microstructures by the surgical needles through which the optical fibres were placed in the tissue. Further, the detector probes are believed to distort the fluence field (Arnfield et al., 1990, Lilge & Wilson, 1993). While the results of these studies indicated reasonable agreement between experiment results and the theoretical models, other important sources of errors identified were approximations in the theoretical models of light propagation such as neglecting the effect of inhomogeneities of the tissue optical properties and boundaries.

Lilge & Wilson (1993) assessed the accuracy of the interstitial measurements by investigating the effect of different source and detector fibres and models of light propagation on the derived optical properties. The experiments involved measurement of the absolute fluence rate in optically infinite and semi-infinite tissue-simulating phantoms for a wide range of optical properties using four isotropic, interstitial detectors calibrated for absolute response and delivery fibres with anisotropic and isotropic emission. The optical properties were derived using three mathematical models of light propagation to investigate the effect of the model on the derived absorption and reduced scattering coefficients, μ_a and μ_s', respectively.

While there appeared to be no difference between the derived optical properties for the different mathematical models, which was attributed to a lack of sensitivity of the fitting routine, the least-squares algorithm failed to converge for certain phantoms. These phantoms were those for which the assumption that the phantom was semi-infinite was invalid, suggesting the importance of taking boundaries into consideration. Other limitations to the technique which were suggested, some of which were consistent with the findings of other investigators, were the uncertainties in detector calibration, positional accuracy, optimum number of detectors and the effect of the detector probe itself on the fluence distribution.

This study, as outlined in the project proposal (Chapter 1) was aimed at improving quantitative *in vivo* dosimetry by investigating the influence of finite volume effects on the interstitial fluence rate measurements and quantifying the systematic errors in the technique. This required evaluation of the experimental procedure, as well as the diffusion models used to derive the optical properties. The experimental procedure presented in this chapter is divided into two parts. The first describes the interstitial measurements made in infinite and semi-infinite tissue-simulating phantoms to reproduce the study by Lilge & Wilson (1993), and expanded to investigate two detector arrangements with respect to the delivery fibre. The second part, the core of this thesis, is a description of the measurements in the finite volume phantoms which are compared directly with Monte Carlo predictions in Chapter 5.

4.2 Tissue-simulating phantoms

Tissue-simulating phantoms, as the name suggests, mimic the absorption and scattering characteristics of tissue thereby allowing investigation of the numerous factors affecting light propagation. The requirements of optical phantoms include optical stability and reproducibility of optical properties, the ability to simulate a wide range of optical properties and flexibility in modelling various geometries and boundary conditions (Wilson & Patterson, 1986). In addition, these phantoms must be homogeneous to satisfy the assumption of homogeneity of optical properties in some mathematical models of light propagation and the material should be non-fluorescent to avoid interference with the fluorescence signal of the fluence rate detectors. The phantom materials used in this study were Intralipid-20% as a scatterer and Crystal Violet and Congo Red as molecular absorbers.

4.2.1 Scatterer : Intralipid-20%

Intralipid (Intralipid-20%) is a phospholipid emulsion, comprising soybean oil, glycerin, lecithin and water, used clinically as an intravenous nutrient. Intralipid-10% has been commonly used as a scatterer in light dosimetry studies because it is relatively inexpensive and its optical properties, μ_a, μ_s and g, are reproducible and well characterized (Flock et al., 1992; van Stavaren et al., 1991). The absorption coefficient of stock Intralipid-10% is negligible compared to the scattering coefficient, with μ_a ranging from 0.0015 - 0.0007 mm^{-1} between 460 and 690 nm (Flock et al., 1992). For these experiments, performed at 514 nm, the contribution of Intralipid to the absorption coefficient of the phantom was neglected. The scattering particles in Intralipid are lipid micelles and vesicles formed, respectively, by the encapsulation of soybean oil in lecithin and by lecithin bilayers (van Stavaren et al., 1991). The scattering parameters have been calculated from Mie theory, based on the size distribution of the micelles and vesicles. Van Stavaren et al., (1991) have suggested the following expression to approximate the wavelength dependence of μ_s and g for Intralipid-10%:

$$\mu_s (\lambda) = 0.016\, \lambda^{-2.4} \qquad (\pm 6\%) \tag{4.1}$$

and

$$g (\lambda) = 1.1 - 0.58\, \lambda \qquad (\pm 5\%) \tag{4.2}$$

where λ is in micrometres (van Stavaren et al., 1991) and μ_s is in units of $ml^{-1}\,L\,mm^{-1}$ (recall that the true units of μ_s are mm^{-1}) for a certain concentration of Intralipid in water (ml per L). From equations (4.1) and (4.2), the scattering coefficient and anisotropy parameter of stock Intralipid-10% were determined to be 0.0790 $ml^{-1}\,L\,mm^{-1}$ and 0.802, respectively at 514 nm. A reduced scattering coefficient of 0.0156 $ml^{-1}\,L\,mm^{-1}$ was calculated using the relation ($\mu_s' = \mu_s\,[1 - g]$). The volume of Intralipid-20% required for a particular phantom was determined as :

$$V_{Intra} = \frac{1}{2} \left(\frac{\mu_s'{}_{ph}}{\mu_s'{}_{Intra}} \cdot V_{ph} \right) \tag{4.3}$$

where V_{intra} and V_{ph} are the volume of Intralipid-20% and the total volume of the phantom, respectively; $\mu_s'{}_{ph}$ and $\mu_s'{}_{intra}$ are the reduced scattering coefficients of the phantom and stock Intralipid-20% solution, respectively and the factor of ½ was to used to convert the values for Intralipid-10% to Intralipid-20%. The range of reduced scattering coefficients used in the interstitial measurements in infinite and semi-infinite, and finite volume phantoms are shown in Tables 4.1 and 4.2, respectively.

Table 4.1 Range of reduced scattering (μ_s') and absorption (μ_a) coefficients, respectively, of the phantoms used in the infinite and semi-infinite experiment (Crystal violet as absorber - μ_a stock = 102.9 mm^{-1}). The values quoted for μ_a are the calculated values multiplied by the correction factor discussed in the text.

μ_s' (mm^{-1})	μ_a (mm^{-1})
0.1	0.0059
0.5	0.0119
1.0	0.0296
2.0	0.0593
5.0	0.1186
10.0	0.2965
20.0	0.5930

Table 4.2 Optical properties of the finite volume phantoms (Congo Red as absorber - μ_a stock = 89.8 mm^{-1})

Phantom	μ_s' (mm^{-1})	μ_a (mm^{-1})
1	0.5	0.015
2	1.0	0.030
3	3.0	0.090

4.2.2 Molecular absorbers : Crystal Violet and Congo Red

Although the particulate absorber, India ink, comprised of minute carbon particles, has been used in many studies for modelling light distribution in optical phantoms, Madsen et al. (1992) have determined that the ink particles also scatter light which makes it difficult to measure the absorption coefficient of the ink accurately. As a result, molecular dyes are preferable as absorbers in tissue-simulating phantoms. The criteria are water solubility since they are to be used in conjunction with Intralipid, significant absorption at 514 nm, the excitation wavelength used in these experiments, and negligible fluorescence over the wavelength range of interest, 600 - 800 nm. In addition, the dye must be photostable and chemically inert so that it does not react with the Intralipid.

4.2.2.1 Crystal Violet

A saturated solution of Crystal Violet (Fisher Scientific, Nepean, Ontario) was made up in double-distilled (Millipore) water and left in an ultrasonic bath for 15 minutes, after which the undissolved dye was removed using 0.45 μm (Sterile Acrodisc) filters. A dilution series of Crystal Violet was prepared by successive dilution (1:9) in double-distilled water and the third and fourth dilutions were measured on a standard UV/VIS spectrophotometer (SP8-400, Pye Unicam) to obtain the optical density (OD),

$$OD = -\log_{10}\frac{I}{I_0} \tag{4.4}$$

where I and I_0 are the intensities of the incident and transmitted light, respectively. Using Beer's law,

$$I = I_0\, e^{-\mu_{ext} d} \tag{4.5}$$

and equation (4.4) and assuming that the dye is a pure absorber ($\mu_{ext} = \mu_a$), the absorption coefficient is calculated as :

$$\mu_a = \frac{2.3 \cdot OD k}{d} \tag{4.6}$$

where k is the dilution factor and d (= 1 cm) is the path length through the cuvette containing the sample. The OD measured for the third and fourth dilutions were 0.455 and 0.044, respectively, from which an absorption coefficient of 102.9 mm^{-1} ($\pm$2.4 mm^{-1}) was calculated. The volumes of Crystal Violet stock solution required for the optical phantoms used in the experiment in infinite and semi-infinite volumes were calculated according to :

$$V_{dye} = \frac{\mu_{a_{ph}}}{\mu_{a_{stock}}} \cdot V_{ph} \tag{4.7}$$

The optical properties of the Crystal Violet and Intralipid-20% phantoms (Table 4.1), used in the measurements in the infinite and semi-infinite volumes, were checked using a spatially resolved diffuse reflectance technique (Farrell et al, 1992). This technique is based on measurements of the light diffusely reflected from the phantom and subsequent derivation of the optical properties using a neural network (Farrell & Patterson, 1992). The measured μ_a values from a number of the phantoms in the series were observed to be a factor of 0.593 lower than the calculated values, while the μ_s' values were identical within the limits of the experimental errors. The inability to fit the interstitial fluence rate measurements with theoretical predictions of the fluence rate for the calculated optical properties of the phantoms supported the μ_a values derived from the diffuse reflectance measurements. The calculated values were corrected by the factor 0.593. This discrepancy could have been due to an interaction between the Crystal violet and Intralipid, such as incorporation of the dye into the micelles and vesicles of the Intralipid.

4.2.2.2 Congo Red

As a result of the above-mentioned problem with Crystal Violet, another molecular absorber, Congo Red (Aldrich Chemical Company, Milwaukee, USA), was selected as the absorber for the finite volume measurements. Congo Red was well-suited for these experiments since it was water soluble, had an absorption maximum around 500 nm, did not fluoresce over the spectral range of interest and demonstrated no interaction with Intralipid in the optical phantom. Following the same procedure as described above, a stock solution with an absorption coefficient of 89.8 mm-1, (±1.6 mm^{-1}) was prepared and used for the three phantoms, shown in Table 4.2.

4.2.3 Optical phantoms

4.2.3.1 Infinite and semi-infinite volume phantoms

The phantom used in the infinite and semi-infinite volume experiment was a 1 litre cube (10 cm*10 cm*10 cm) with blackened walls. Wilson & Jacques (1990) have determined that light losses occur at the boundary if the phantom half-width is less than 12δ ($\delta = 1/\mu_{eff}$). With the source-detector array at a depth of 5 cm below the surface an optically infinite medium was simulated for phantoms with $\mu_{eff} > 0.24$ mm^{-1}, while placing the array at a depth of 2 mm enabled simulation of a semi-infinite medium with a refractive index mismatch at the surface ($n_{rel} = 1.33$). For each of the seven scattering coefficients shown in Table 4.1, ink was added to the phantom to give absorption coefficients in the range $0.01 \leq \mu_a \leq 1$ mm^{-1} for a total of 49 phantoms. This wide range of optical properties was chosen since it encompassed the range of values for the optical coefficients quoted in the literature (Cheong et al., 1990).

4.2.3.2 Finite volume phantoms

Two spheres were built for the finite volume experiments, each comprising two hemispheres made from 1 inch (25.4 mm) thick, transparent plastic (see schematic in Figure 4.1). The inner walls of the spheres were coated with several layers of white and black enamel to simulate a diffuse reflecting and absorbing boundary, respectively. The final inner diameters were 38 mm for the black sphere and 37.5 mm for the white. The diffuse reflectance of the black and white spheres was measured using an integrating sphere technique described by Jaywant *et al.* (1993). A collimated beam was imaged onto the sample (black and white hemispheres, respectively) and the diffusely reflected light was measured by the integrating sphere. The reflectances measured at 514 nm were 0.78 and 0.033 for the white and black spheres, respectively, values used in the Monte Carlo simulations. There were a number of possible errors in these measurements which included the poor alignment of the sample with the integrating sphere which may have resulted in light loss at the port and the use of collimated rather than diffuse incidence. These errors in addition to the fact that the sample presented a hemispherical surface while the reflectance standards used were planar, could have contributed to an underestimation of the reflectance.

As shown in Figure 4.1, a slit at the top of the upper hemisphere facilitated insertion of the source-detector array for the finite volume measurements. The fibre array was introduced into the phantom via surgical needles mounted in a micrometer-controlled frame. The light scattering media were poured into the spheres which were water-tight when sealed. The transport albedo ($a' = 0.97$) of the phantoms used in these measurements was chosen on the basis of values quoted in the literature for brain tissue (Cheong et al., 1990). The optical properties (see Table 4.2) were then scaled to enable investigation of the effect of different sphere sizes (in terms of transport mean free paths) on the interstitial fluence rate measurements. Different sphere sizes (increasing from phantoms 1 through 3) correspond to different skull sizes in animal models.

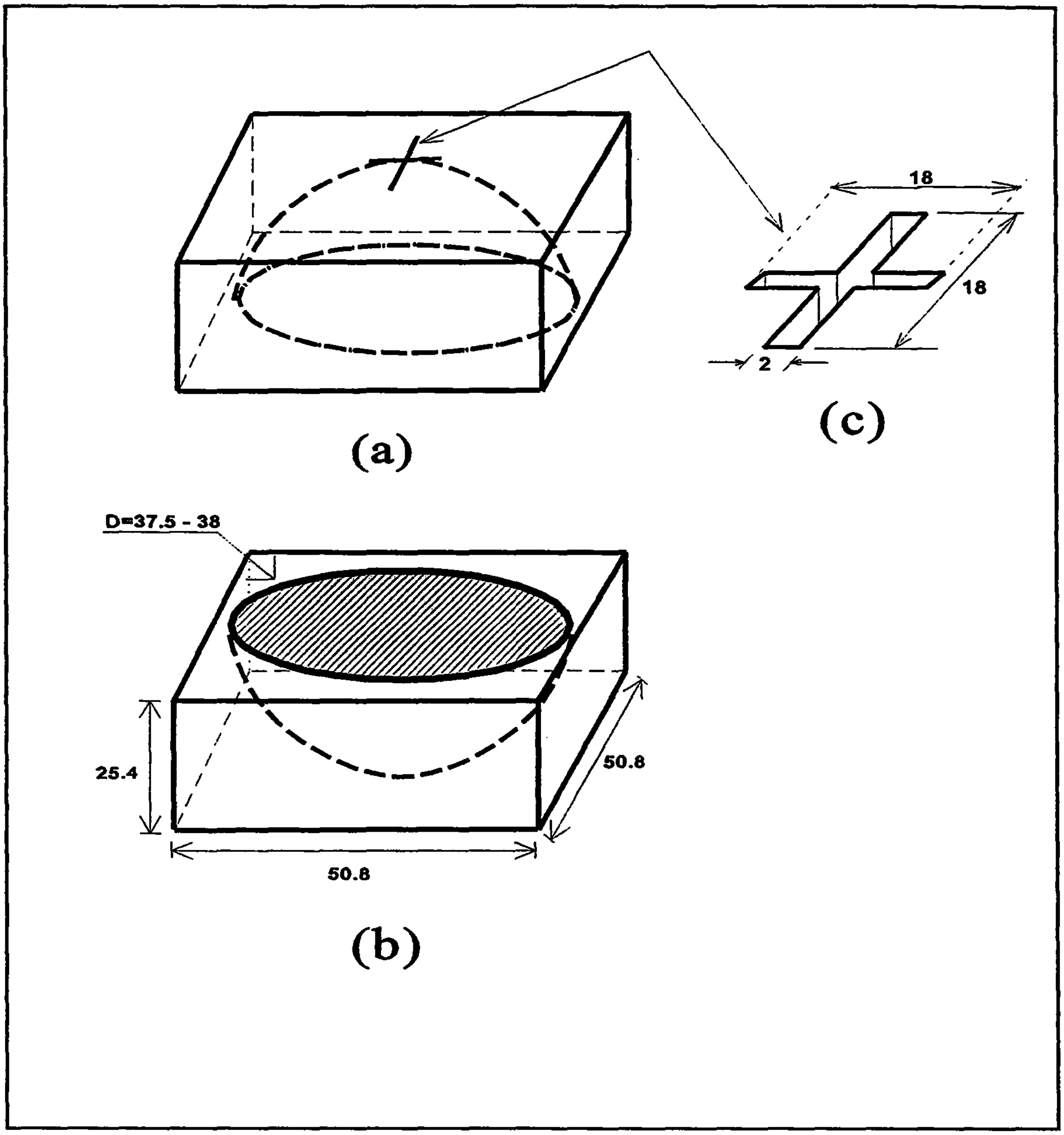

Figure 4.1 Schematic of finite spherical phantom showing (a) upper hemisphere, (b) lower hemisphere and (c) slit for insertion of source-detector array. All dimensions are in millimetres.

4.3 Interstitial experiments

Apart from the tissue-simulating phantoms used, the major components of the experimental arrangement were essentially the same for the two experiments (Figure 4.2), and are discussed below.

4.3.1 Charge-coupled device (CCD) detection system

The distal end of the detector fibres was imaged onto the entrance slit of a spectrograph and the spectrally resolved data collected by a cryogenically cooled charge-coupled device, CCD (EG&G Instruments), which replaced the exit slit of the spectrograph (see Figure 4.2). The processing of the data included background subtraction for the electronic noise of the CCD and room light leaking into the system, performed automatically as the spectra were acquired, and subsequent integration of the fluorescent peak area. Figure 4.3 illustrates a typical spectrum acquired.

4.3.2 Isotropic detectors

The fibre optic detectors developed by Lilge et al. (1993, 1990) have an isotropic response. These probes, shown in Figure 4.4, comprise a dye-filled silica capillary tubing attached to the end of a 100 μm core optical fibre (outer diameter = 170 μm). The fluorescent dye is Rhodamine 610 excited with 514 nm light and emits in the spectral

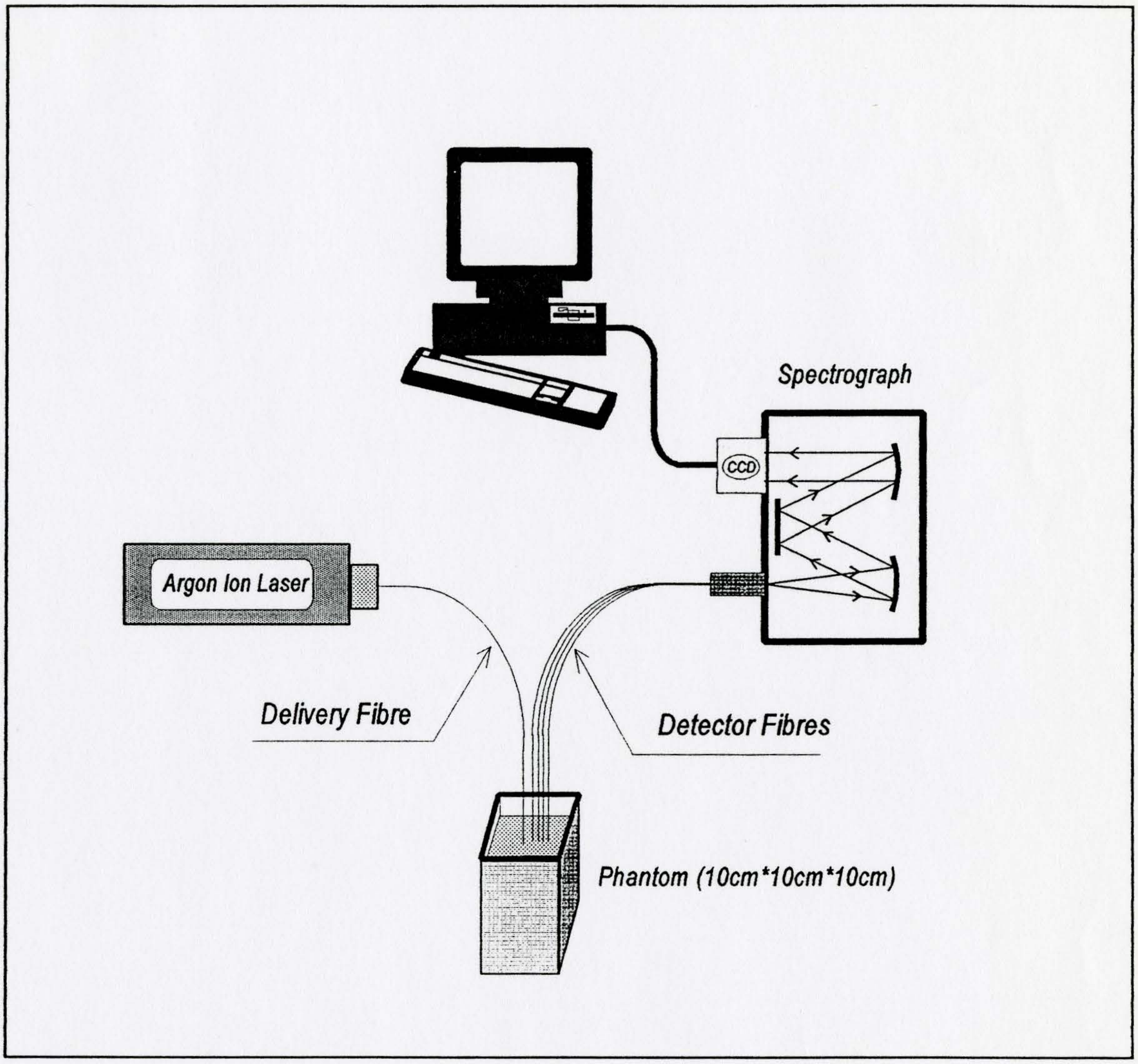

Figure 4.2 Experimental arrangement for interstitial measurements

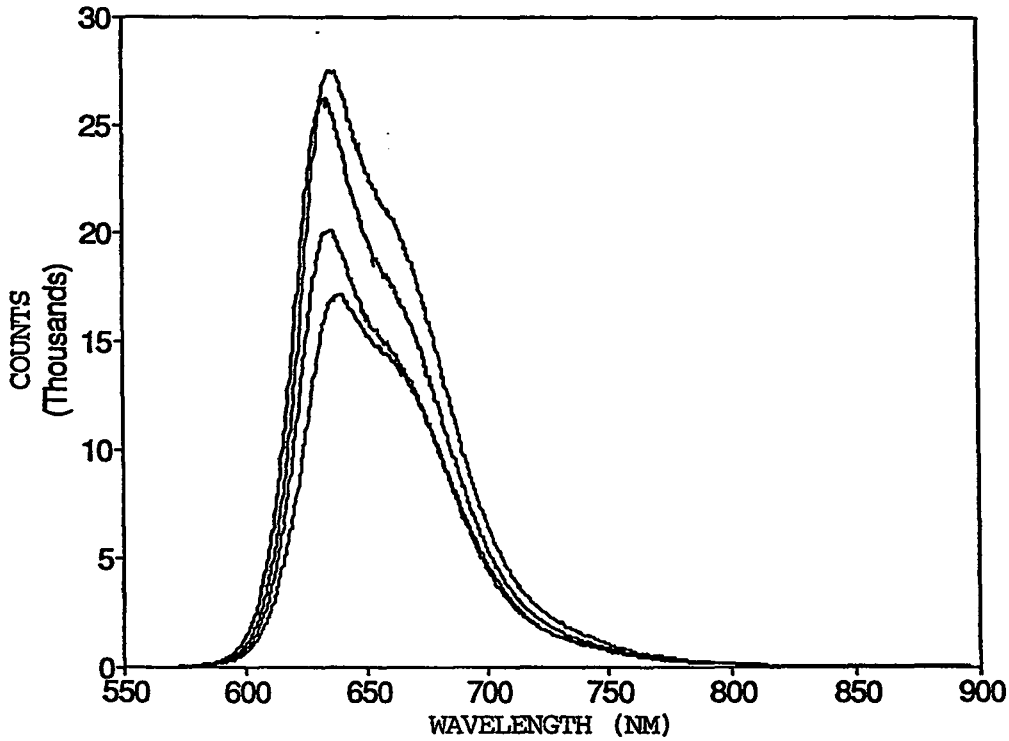

Figure 4.3 Typical spectra acquired for the four fluorescent detector probes

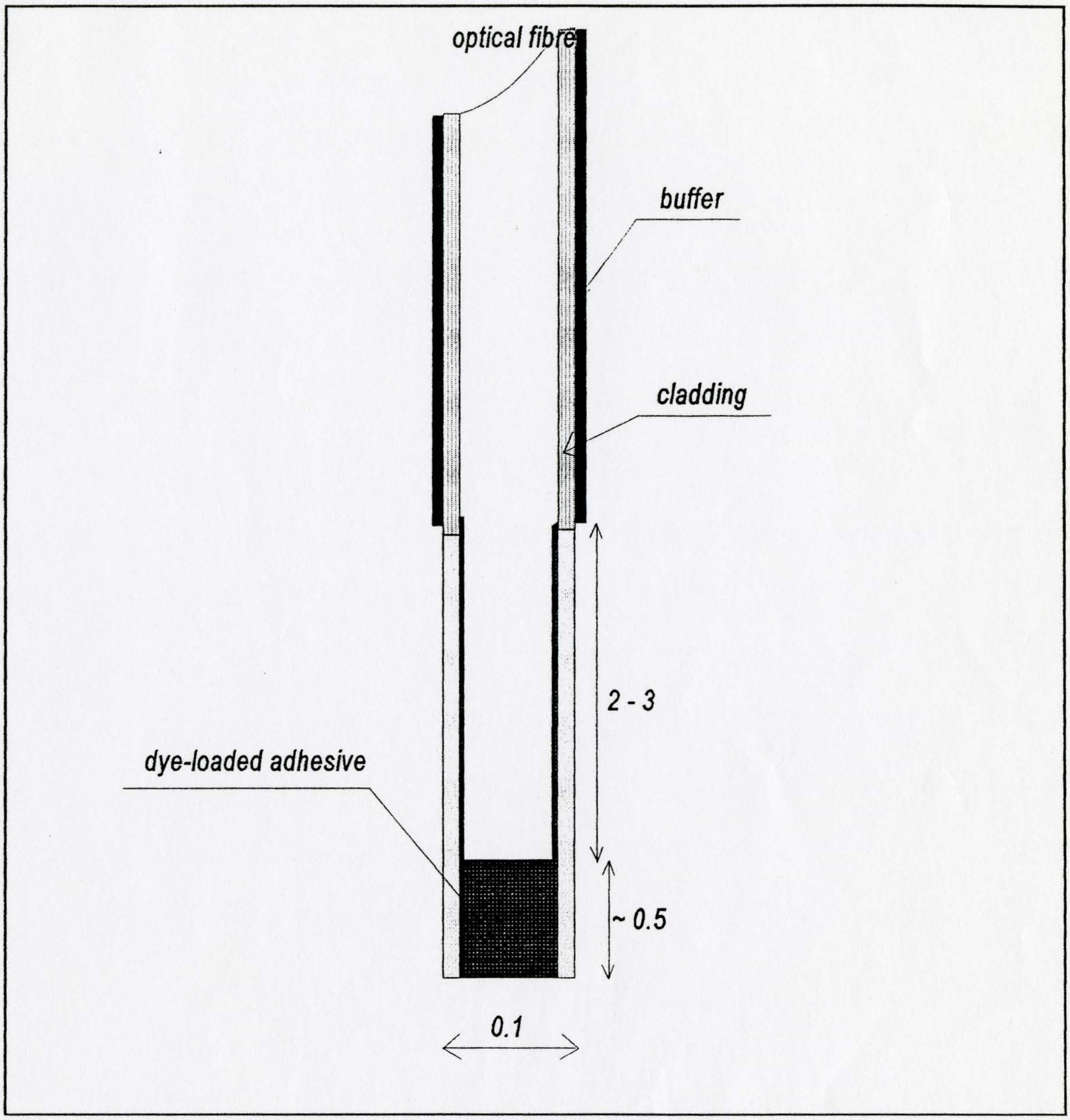

Figure 4.4 Fluorescent-tipped interstitial probes (Lilge et al., 1993). All dimensions are in millimetres.

range 600 - 800 nm. The fluorescent light detected by the charge-coupled device (CCD), discussed previously, is proportional to the local fluence rate at the fibre tip.

4.3.3.1 Absolute response calibration of detector probes

The probes were individually calibrated for absolute response (Lilge & Wilson, 1993) by fitting the measured fluence rates at the known detector positions to the fluence rate profile calculated using one-dimensional diffusion theory for a phantom with $\mu_s' = 2.0$ mm^{-1} and $\mu_a = 0.01$ mm^{-1}. Uniform irradiation of the phantom surface was achieved using a microlens-fitted optical fibre. The surface irradiance was determined by measurement of the total power output of the delivery fibre determined with a hand-held power meter (Newport Corporation) and measurement of the beam spot size on the phantom surface.

The depth profile of the fluence rate (obtained by advancing the source-detector array into the phantom in millimetre steps) was fitted to the fluence rate profile calculated using one-dimensional diffusion theory, taking into account the irradiance (Wcm^{-2}) and the optical properties of the phantom (Lilge & Wilson, 1993). Calibration factors were derived for individual detector probes with calibration errors (determined from the correlation coefficient of the fitting routine) in the 5 - 15% range. Figure 4.5 illustrates the calculated one-dimensional fluence rate profile and the measured fluence rates for four detector probes. Calibrations were performed prior to the actual measurements and repeated if any of the detector probes were replaced or if the coupling to the spectrograph/CCD detector was altered. Photobleaching of the fluorescent dye in the detector probes, and consequent changes in the responsivity (calibration factor) of the probe (Lilge et al., 1993, Lilge & Wilson, 1993) were neglected since the exposure times were kept as short as possible and the detector probes were replaced after receiving about 120 Jcm^{-2} (Lilge & Wilson, 1993).

4.3.3.2 Power calibration of delivery fibres

A 320 μm core diameter cut-end fibre and an 800 μm spherical scattering tip attached to a cut-end fibre with 400 μm core diameter were employed in these experiments as anisotropic and isotropic emitting delivery fibres, respectively. Power at the distal end of the anisotropic delivery fibre was measured using the hand-held power meter and the built-in photodetector of the integrating sphere (Labsphere Inc., Manchester, New Hampshire) was calibrated with this cut-end fibre. Subsequently, the output power of the isotropic emitting fibre was calibrated by measurement in the integrating sphere. These fibres were calibrated prior and subsequent to the experiments to check for stability of the light power.

4.3.4 Fluence rate measurements

An air cooled argon ion laser (Ion Laser Technology, Salt Lake City, Utah) with a maximum power output of 50 mW at 514 nm was coupled into the delivery fibre. Figure 4.6 illustrates the linear and spiral arrays of the detector probes relative to the delivery fibre which were used in the interstitial experiments. In the linear array, the fibres were spaced

2 mm apart (2, 4, 6, 8 mm) while in the spiral array the detector fibres were at radial distances of 2.0, 4.7, 7.0 and 8.0 mm respectively, from the source fibre.

4.3.4.1 Measurements in infinite and semi-infinite volumes

Measurements were made in 49 tissue-simulating phantoms (1 litre cubic phantom) for the range of optical properties shown in Table 4.1, using anisotropic and isotropic delivery and linear and spiral source-detector arrays. The local fluence rate at the positions of the detectors was calculated based on the measured fluorescence signal and the calibration factor, described previously. The optical properties of the phantoms were subsequently derived as free parameters by fitting the measured fluence rate to the predictions of the diffusion model, equations (2.14) and (2.20) for the infinite and semi-infinite measurements, respectively, using a grid-search least-squares fitting routine (Bevington, 1969). The accuracy of the derived optical properties for the 49 phantoms was assessed for the two source-detector arrays by comparison with the known optical properties given in Table 4.1, as will be discussed in the next chapter.

4.3.4.2 Measurements in finite spherical volume

As a result of difficulties in producing 4 detector probes with similar responses, the array of 4 detector probes was not used in these measurements. Instead, a single detector probe was used and was translated to the four radial positions (2.0, 4.7, 7.0 and 8.0 mm) via the micrometer-controlled frame. After aligning the delivery fibre and the detector probe at the top of the slit, the fibres were advanced 25.4 mm to the centre of the sphere where the measurements at the four radial positions were taken. Measurements were also taken in planes 2 and 3 (with the source at 4 and 2 mm, respectively, from the lower boundary) as shown in Figure 3.7, for both black and white spheres and for the three sets of optical properties presented in Table 4.2. The effect of the boundaries on the interstitial fluence rate measurements was investigated by direct comparison of the measured fluence rates at the known detector positions, with the predictions of Monte Carlo simulations, as well as derivation of the optical properties using the diffusion theory solution for infinite media (equation 2.14).

4.3.4.3 Rodent skulls

In order to investigate the effect of a complex, finite geometry on the interstitial technique, fluence rate measurements were made in a rabbit skull submerged in each of phantoms 1 and 2 (see Table 4.2) using anisotropic delivery. A slit, 2 mm in width and 9 mm long was made in the left hemisphere at the top of the skull to allow insertion of the source-detector array. The delivery fibre was located 5 mm lateral of the midline, posterior to the skull with the detector anterior to the delivery fibre. The fibres were aligned at the top of the slit and measurements were taken (at the four radial positions) at 1, 2 and 5 mm from the base of the skull. The fibres were approximately at the centre of the cranial cavity at the 5 mm position. Subsequently, the optical properties were derived from these measurements as described before in order to estimate the magnitude of the boundary effect.

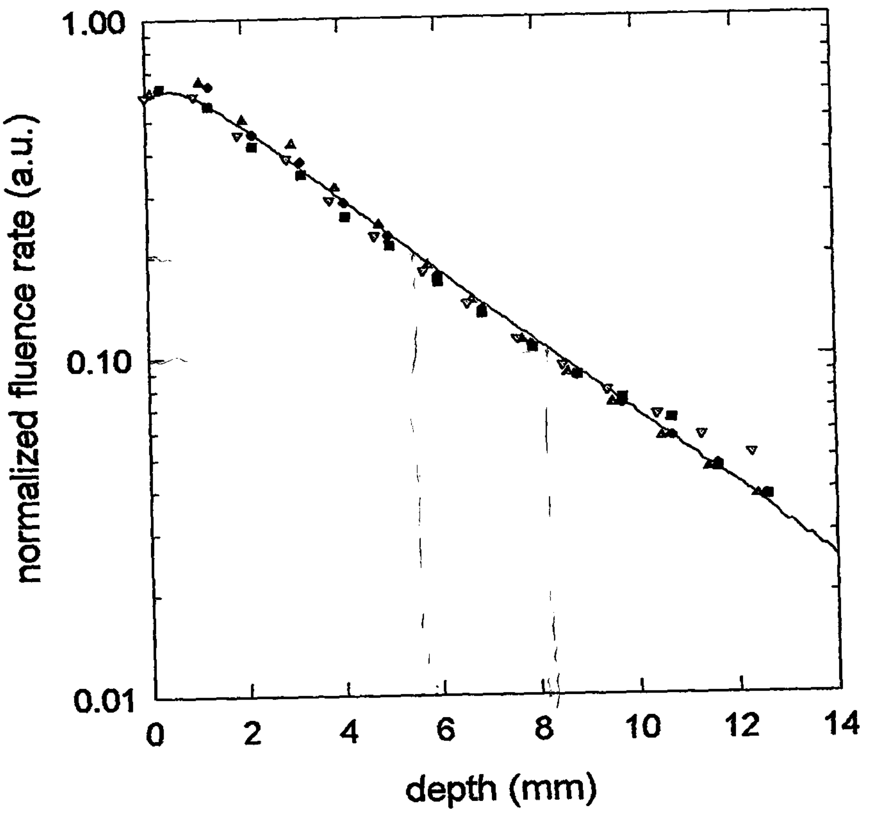

Figure 4.5 Detector probe calibration: line represents one-dimensional diffusion theory and symbols correspond to the measured fluence rates (× calibration factors) for 4 detector probes (for a phantom with μ_a = 0.01 mm^{-1} & μ_s' = 2.0 mm^{-1}).

μ_{eff} = 0.2456 mm^{-1}

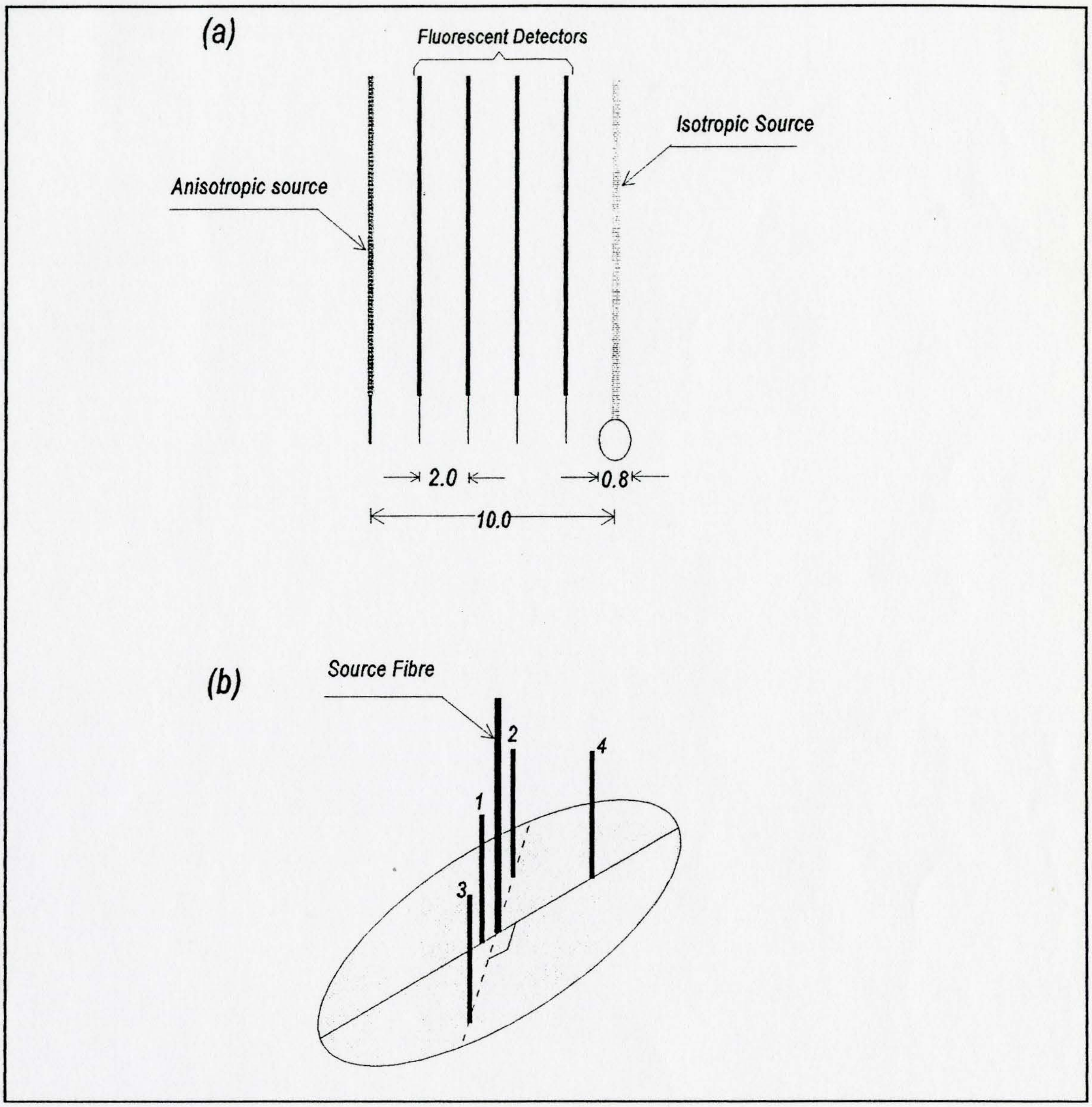

Figure 4.6 (a) Linear and (b) spiral arrangements of the detector probes relative to the delivery fibre. In the spiral array, detectors 1,2 3 and 4 are at radial distances of 2.0, 4.7, 7.0 and 8.0 mm, respectively, from the delivery fibre. All dimensions are in millimetres.

Chapter 5

Results and Discussion

The Monte Carlo code, adapted to simulate isotropic and anisotropic light delivery, is verified by comparison with the diffusion theory models for the fluence rate in infinite and semi-infinite media, equations 2.14 and 2.20, respectively. The interstitial measurements in infinite and semi-infinite media are evaluated by consideration of the accuracy of the derived optical properties. Further, an examination of the boundary effect is made by comparing the experimental fluence rates in finite volumes with predictions of the Monte Carlo model. The optical properties are also determined as independent parameters in a non-linear fit of the experimental fluence rates to the predictions of the infinite diffusion model.

5.1 Verification of Monte Carlo code

5.1.1 Infinite medium

The simulation results presented in this thesis are the mean of 5 runs of 10^5 photons each, enabling estimates of the variance to be made . Absolute fluence rates are normalized to 1 input photon. In Figure 5.1.a the fluence rate distribution calculated from diffusion theory (equation 2.14) is compared with simulation results for an infinite medium with optical properties, μ_a = 04 ~~0.01~~ mm^{-1} and μ_s' = 2.0 mm^{-1}. The accuracy of the code is assessed by considering the residuals between diffusion theory and Monte Carlo models (Farrell & Patterson, 1992). These residuals are calculated as the ratio of the differences between the diffusion theory and Monte Carlo fluence rates to the standard deviation of the Monte Carlo values, at each point. As indicated in Figure 5.1b, beyond 2 transport mean free paths (mfp') from the source, the Monte Carlo data agree well with the diffusion theory within 2 standard deviations.

Simulation results for anisotropic delivery in an infinite medium with optical properties, μ_a = 0.030 mm^{-1} , μ_s' = 1.0 mm^{-1} and g = 0, are plotted in Figure 5.2. In this case the Monte Carlo predictions are compared with two diffusion theory models, equations 2.14 and 2.15. As was observed previously there is good agreement between the diffusion and Monte Carlo models at distances greater than 2 mfp' from the source. There appears to be no significant difference between the two diffusion models which is understandable since for the optical properties of the medium ($\mu_s' \gg \mu_a$), the equation derived by Grosjean (equation 2.15) should approximate equation 2.14. For clarity, only the residuals between the Monte Carlo model and equation 2.14 are presented in Figure 5.2.a.

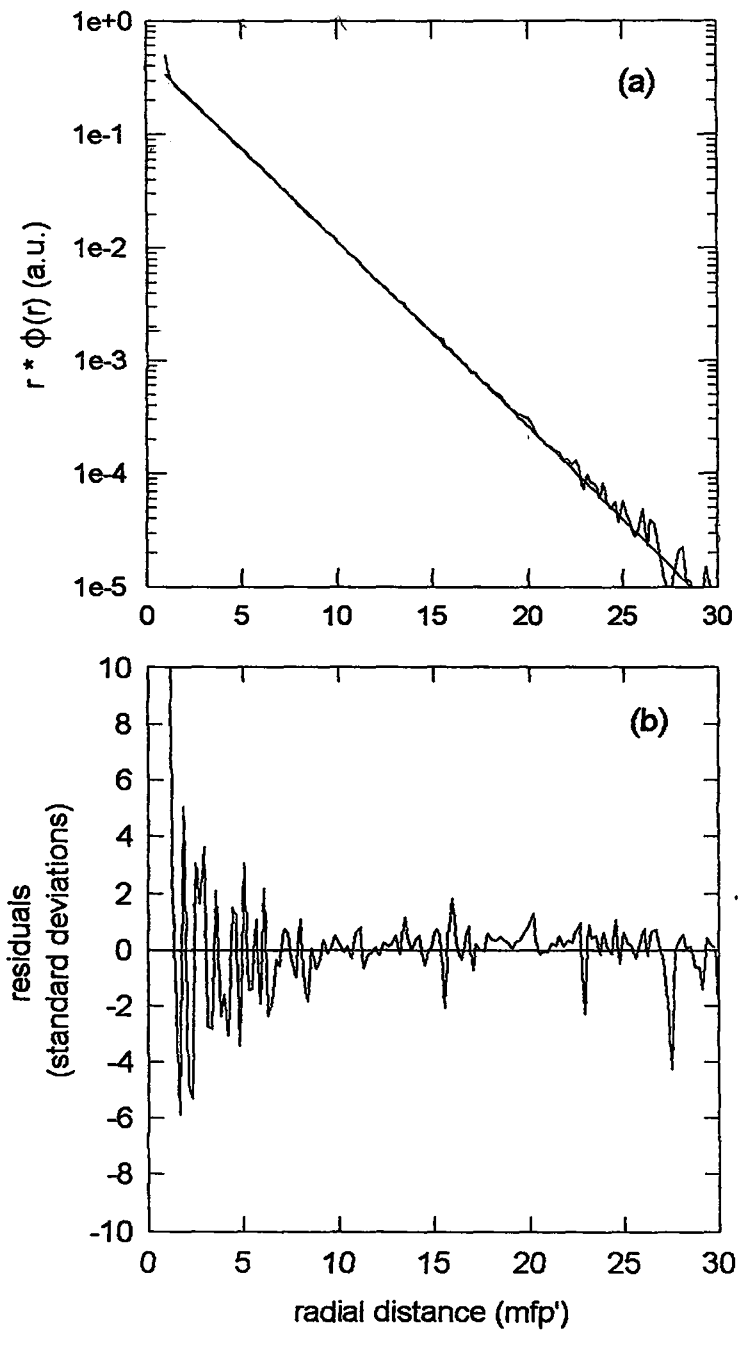

Figure 5.1 Isotropic delivery in an infinite medium. a) Comparison of diffusion theory and Monte Carlo simulations (noisy line), μ_a = 0.1 mm^{-1}, μ_s' = 2.0 mm^{-1} and g = 0.8. b) Standardized residuals

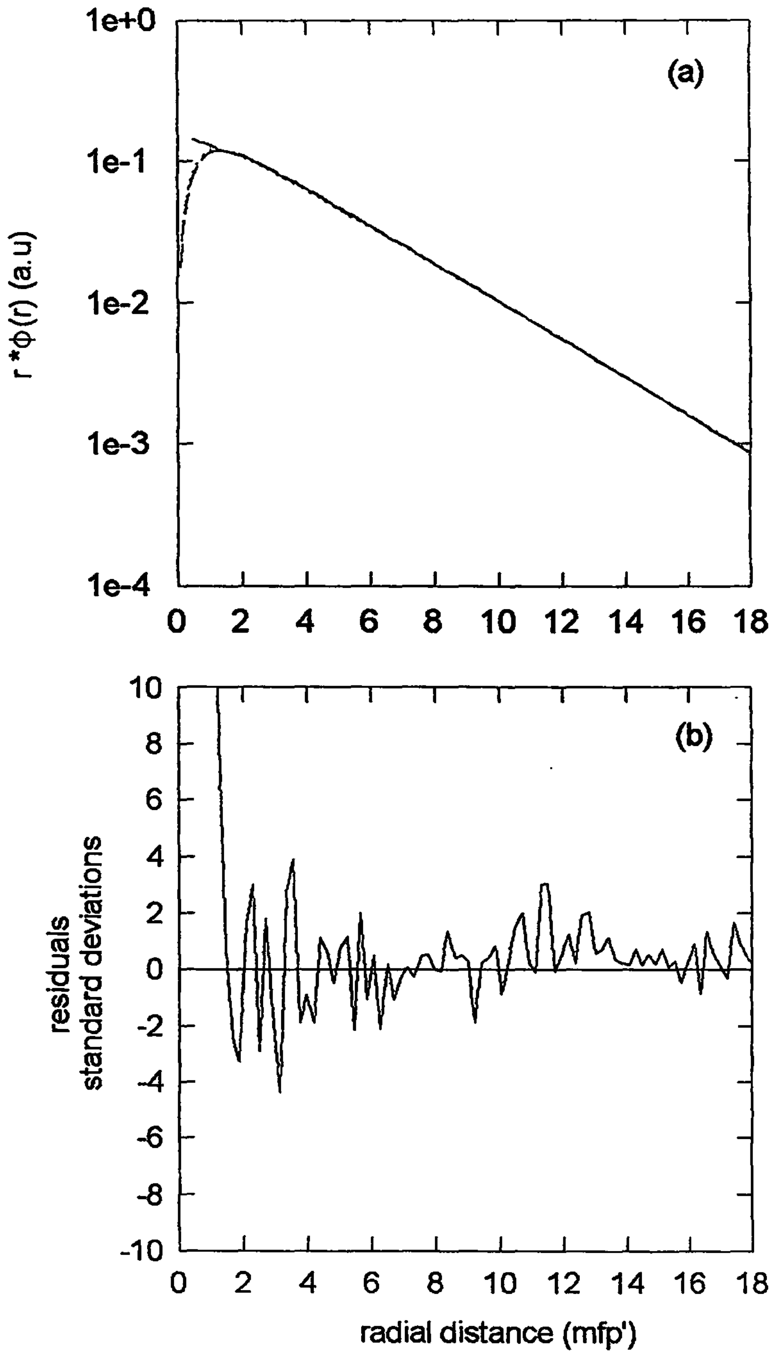

Figure 5.2 Anisotropic delivery in an infinite medium. a) Comparison between diffusion theory (equation 2.14 - dashed line & equation 2.15 - dotted line) and Monte Carlo simulations (solid line) ($\mu_a = 0.03\ mm^{-1}$, $\mu_s' = 1.0\ mm^{-1}$ and g = 0. b) Standardized residuals.

5.1.2 Semi-infinite medium

The Monte Carlo model for a point source in a semi-infinite medium is evaluated for both refractive-index-matched and refractive-index-mismatched boundary conditions by comparison with the diffusion model of equation 2.20. As discussed in Chapters 2 and 3, no photons are allowed to re-enter the medium for the matched boundary, while for mismatched boundaries, photons are totally internally reflected, provided that the angle of incidence exceeds the critical angle. The results for matched and mismatched boundaries, are presented in Figures 5.3 and 5.4, respectively. As was the case for the infinite medium, at distances greater than 2 mfp' from the source the Monte Carlo data agree with the diffusion model within 2 standard deviations.

Having established the accuracy of the Monte Carlo code for isotropic and anisotropic delivery in simple geometries, the effect of albedo on the diffusion model is evaluated by comparing the diffusion model (equation 2.14) with Monte Carlo simulations, in an infinite medium, for the 3 albedos shown in Table 5.1. These optical properties were measured at 633 nm by Splinter et al. (1989) and Andreola (1988),and compiled by Cheong et al. (1990). As is seen in Figure 5.5, both diffusion models are in good agreement with the Monte Carlo calculations for transport albedos of 0.73 and 0.87. At larger distances, equations 2.14 and 2.15 slightly underestimate and overestimate the fluence rate, respectively. As expected, equation 2.15 which is supposed to be accurate for comparable absorption and scattering is in good agreement with the Monte Carlo model while equation 2.14 significantly overestimates the fluence rate at small distances.

Table 5.1 Optical properties for Figure 5.5

Tissue type	μ_a (mm^{-1})	μ_s' (mm^{-1})	a' (= μ_s'/μ_t')
human white matter [1]	0.158	0.204	0.56
human grey matter [1]	0.263	0.722	0.73
human liver [2]	0.320	2.070	0.87

References :

1. Splinter et al., 1989
2. Andreola, 1988

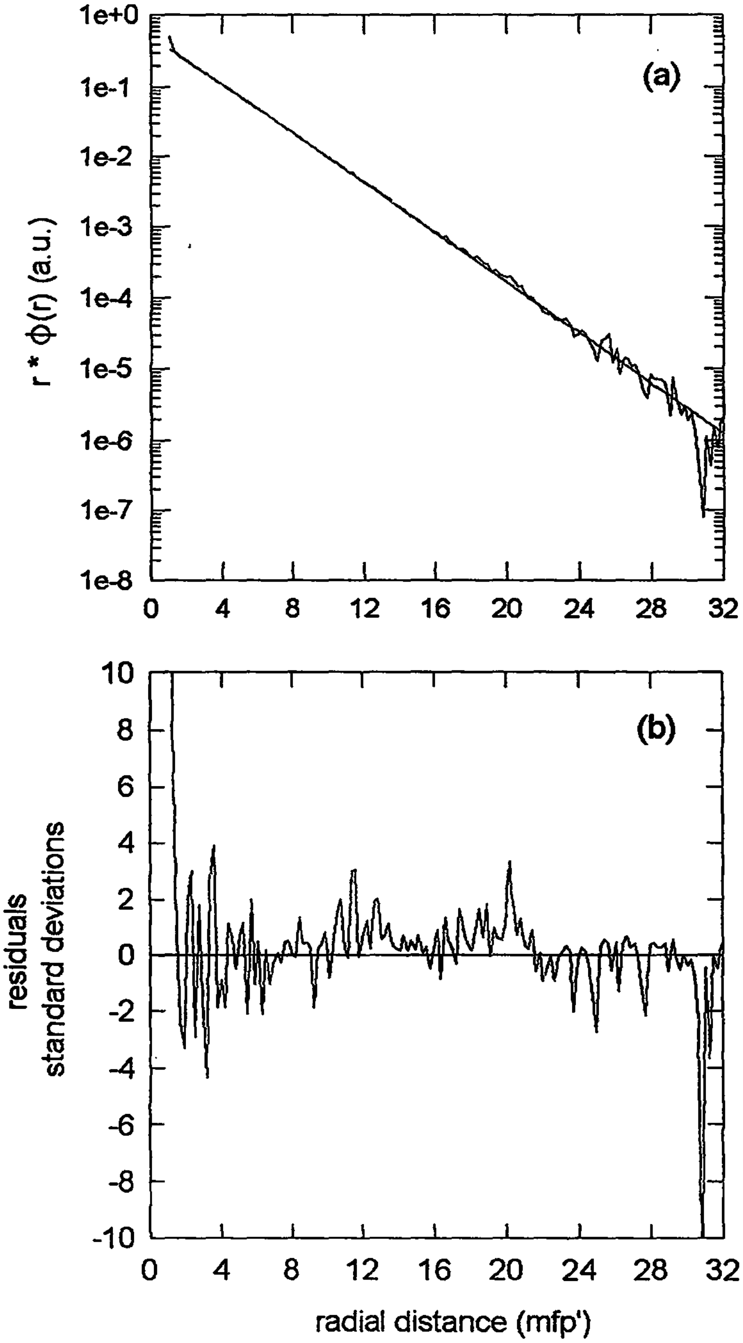

Figure 5.3 Refractive-index-matched boundary. a) Comparison between diffusion theory and Monte Carlo simulations (noisy line) for a semi-infinite medium with $\mu_a = 0.1\ mm^{-1}$, $\mu_s' = 2.0\ mm^{-1}$ and g = 0.8. b) Standardized residuals.

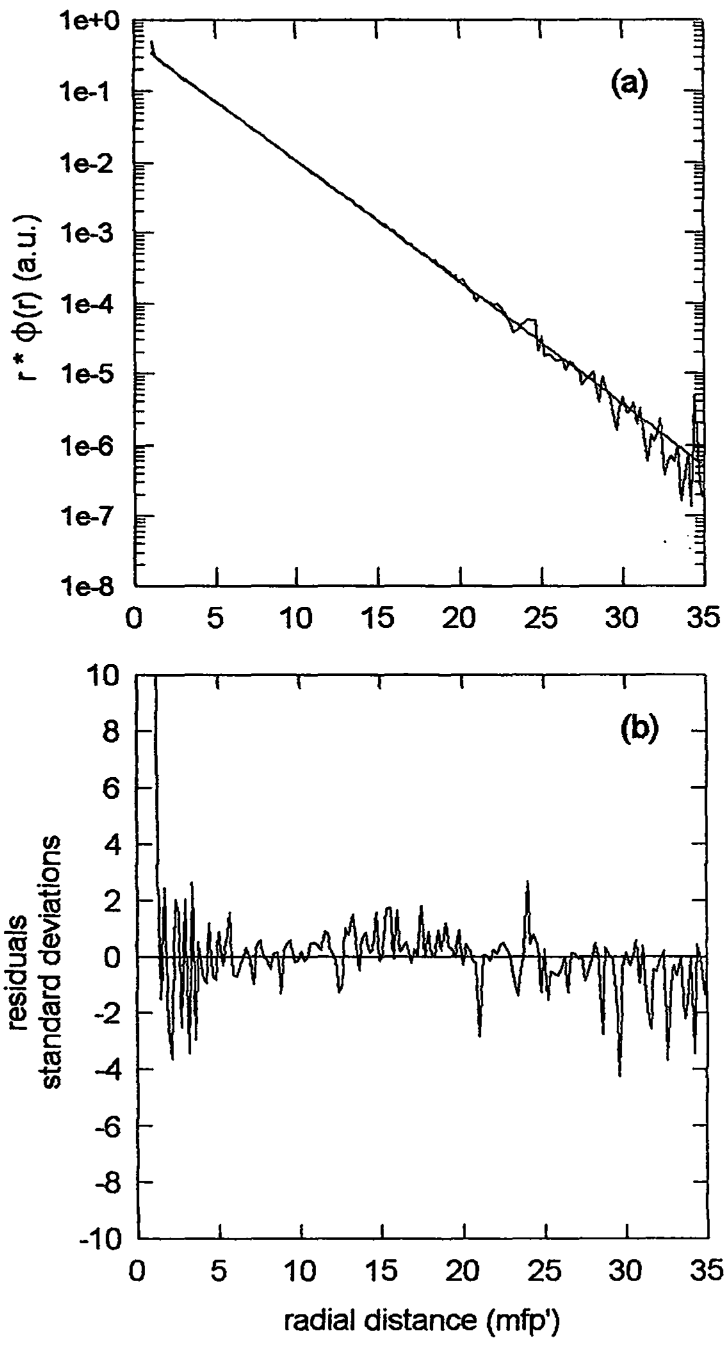

Figure 5.4 Refractive-index-mismatched boundary. a) Comparison between diffusion theory and Monte Carlo simulations (noisy line) for a semi-infinite medium with $\mu_a = 0.1$ mm^{-1}, $\mu_s' = 2.0$ mm^{-1} and g = 0.8. b) Standardized residuals.

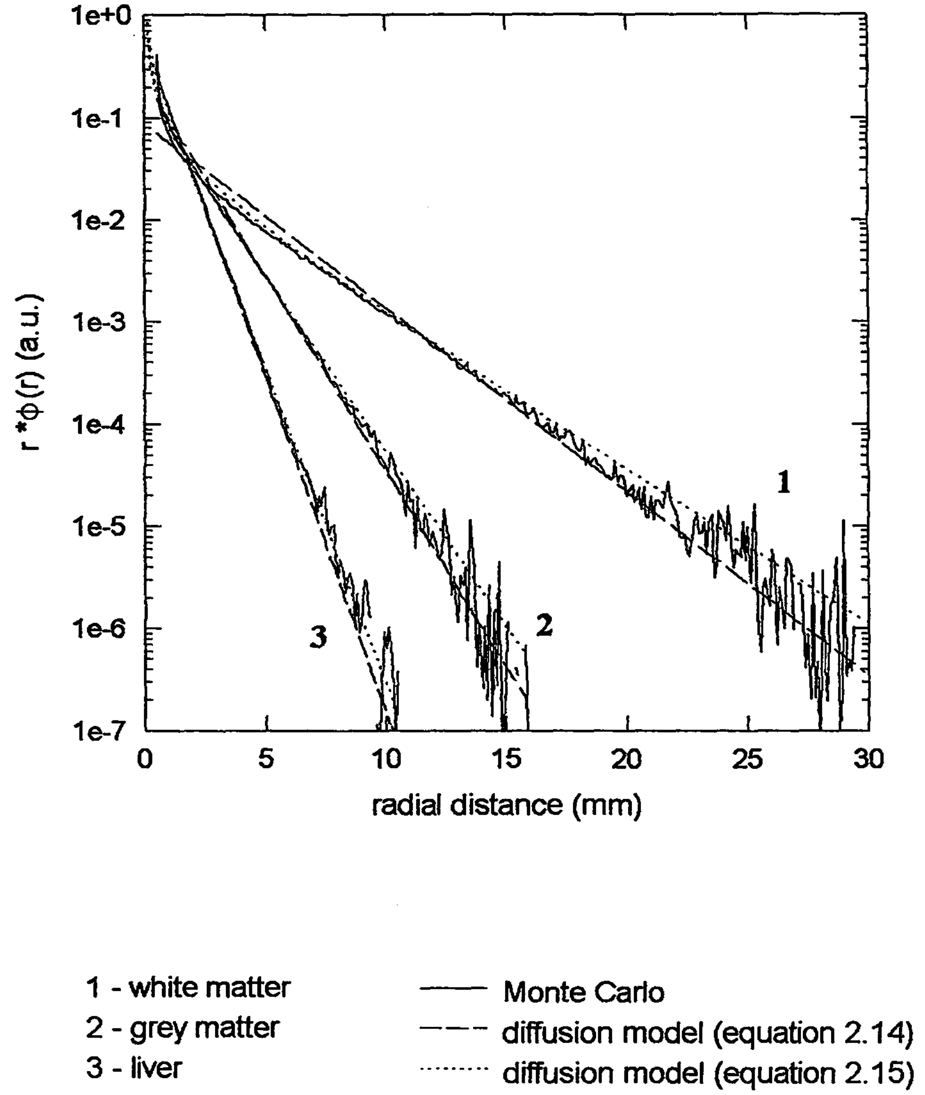

Figure 5.5 Effect of albedo on the accuracy of diffusion theory models (equation 2.14 - dashed lines & equation 2.15 - dotted lines) compared with Monte Carlo simulations (solid lines) for isotropic delivery in an infinite medium.

5.2 Evaluation of the derived optical properties in infinite and semi-infinite medium

As discussed in the previous chapter, interstitial fluence rate measurements were made in optically infinite and semi-infinite (refractive index mismatch - n_{rel} = 1.33) tissue-simulating phantoms. In addition to isotropic and anisotropic light delivery, linear and spiral arrays were used. In the previous study of the accuracy of the derived optical properties by Lilge & Wilson (1993), it was suggested that in the event that the detectors were acting as photon sinks, absorption of photons and the resulting inaccuracy in the derived optical properties could be minimized by avoiding dense packing of the detectors. Arrangement of the detectors in the spiral array was then suggested as an alternative.

These measurements were aimed at investigating whether the use of the spiral array of detectors improved the accuracy of the derived optical properties, through comparison of the derived values with the true values. The optical properties, μ_a and μ_s', were the independent parameters in a grid-search least squares fit (Bevington, 1969) of the measured fluence rates to the fluence rates predicted by the diffusion models (equations 2.14 & 2.20). Figures 5.6 - 5.8 are "pin" plots of the 49 pairs of optical properties in which the head and tail of the pins are the true and derived optical properties, respectively, so that the lengths of the pins represent the magnitude of the error in the derived optical properties.

Figures 5.6.a and b are pin plots of pairs of μ_a and μ_s' for linear and spiral arrays, respectively, and isotropic delivery while Figures 5.6.c and d are corresponding plots for anisotropic delivery in an optically infinite medium. In all cases the error in the derived μ_a

value is greater than that for μ_s' supporting the possibility of a photon sink effect (Figure 5.6 a and c). The larger errors in μ_a can be understood if one considers the diffusion models (equations 2.14 & 2.20) in which the diffusion coefficient, D (= 1/ (3[μ_a + μ_s']) appears in the denominator and μ_{eff} (= $\sqrt{[3\mu_a^2 + 3\mu_a\mu_s']}$) appears in the exponent. It is to be expected that the error in μ_a would be more significant than that in μ_s', since the primary source of error in the fitting routine is error in the slope which is determined by μ_{eff} for which there is a quadratic dependence on μ_a. Large individual errors are attributed to errors in positioning the detectors and low signal in phantoms with a high effective attenuation. For both isotropic and anisotropic delivery the accuracy of the derived optical properties is significantly improved with the spiral array, which can be seen in the pin plots of μ_t' and μ_{eff}, depicted in Figures 5.7.a - d.

The corresponding pin plots for the semi-infinite medium are illustrated in Figure 5.8. Comparing the linear and spiral arrays for isotropic and anisotropic delivery, it is observed that the use of the spiral array significantly improves the accuracy of the derived coefficients in the semi-infinite case. However, the improvement is not as great as in the infinite case. Due to the difficulties involved in positioning the source and the detector probes in the same horizontal plane, and knowing that the spiral array was inserted at only 2 mm below the surface, the increased inaccuracy can be attributed to a surface effect. Nevertheless, the spiral array yields more accurate values for the derived optical properties in both infinite and semi-infinite measurement geometries. From Figures 5.7.b and d and the corresponding plots shown in Figure 5.8, the optical properties are determined to be accurate to within 10% of the true values when $\mu_{eff} > 0.2$ mm^{-1} and $2 < \mu_t' < 10$ mm^{-1}. The limit obtained for μ_{eff}

is justifiable because the 1 litre cubic phantom cannot be considered as an optically infinite medium for $\mu_{eff} < 0.2$ mm^{-1} and therefore, there is a possibility of boundary effects (Wilson & Jacques, 1990). For phantoms with $\mu_t' < 2$ mm^{-1}, the detectors sample the fluence rate over a narrow range of transport mean free paths, specifically $4 <$ mfp' <16, which is too close to the source. At the other end of the range, the detectors are spaced much further apart, $20 <$ mfp' < 80, which may also be a problem since inaccuracies are introduced in the experimental data as a result of low signal.

The actual values of the optical properties greatly influence the derivation of these coefficients from the diffusion models, as is clearly illustrated in Figures 5.9 and 5.10, where the experimental fluence rates at the four detector positions are compared with those predicted by the diffusion model (for isotropic delivery in an infinite medium). As is demonstrated in Figure 5.9, the experimental results are in good agreement with the predictions of the diffusion model. This is because these phantoms all lie within the limits for μ_t' and μ_{eff} discussed previously. On the other hand, Figure 5.10 illustrates a poor agreement between the experiment and the model, which is typical of phantoms with optical properties lying outside of these ranges. Specifically, curve 1 of Figure 5.10 has a μ_{eff} which is less than 0.2 mm^{-1} while curves 2 and 3 are phantoms with $\mu_t > 10$ mm^{-1} and $\mu_t < 2$ mm^{-1}, respectively.

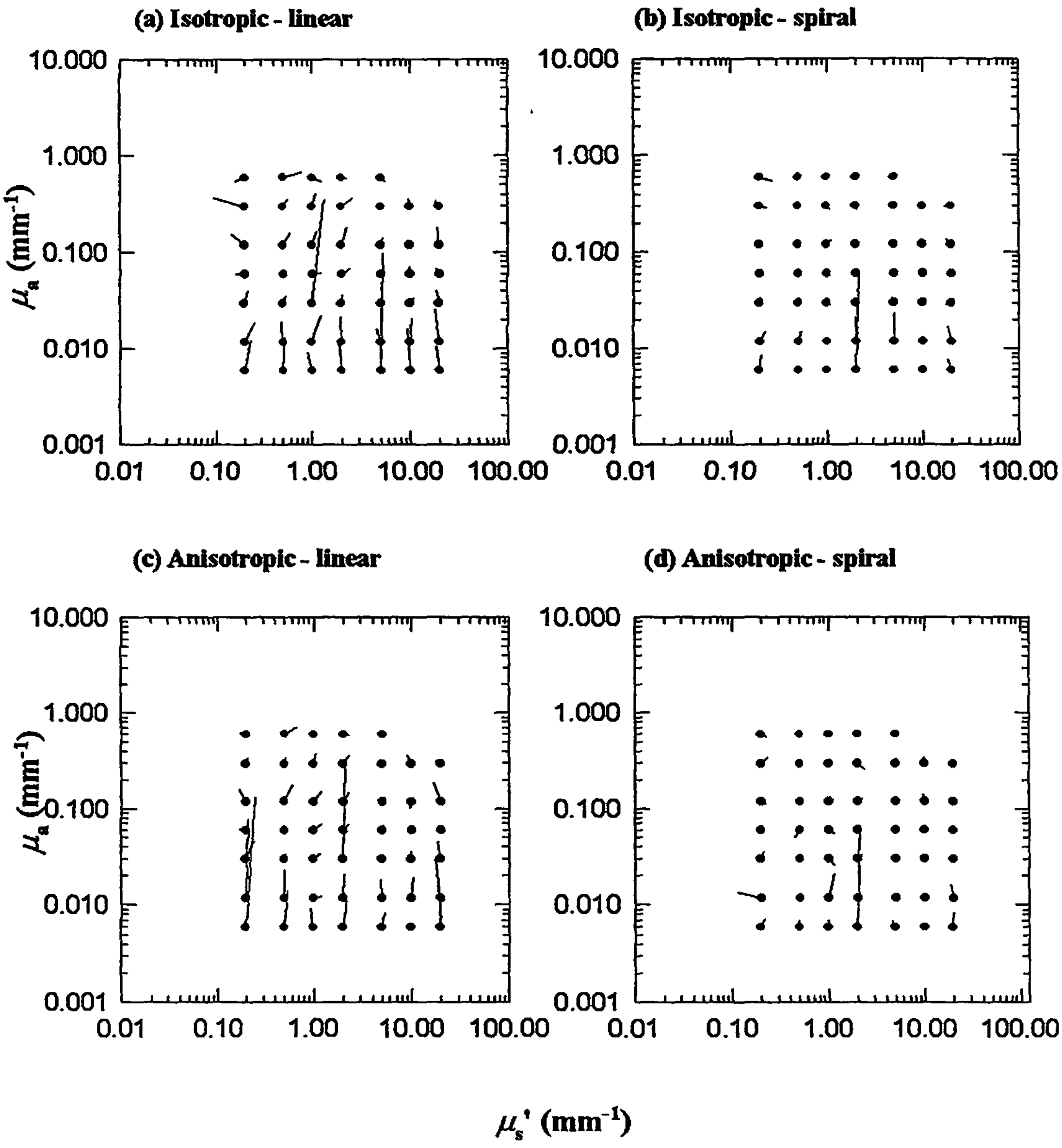

Figure 5.6 Pin plots of μ_a against μ_s' for isotropic and anisotropic delivery using linear and spiral arrays in an infinite medium.

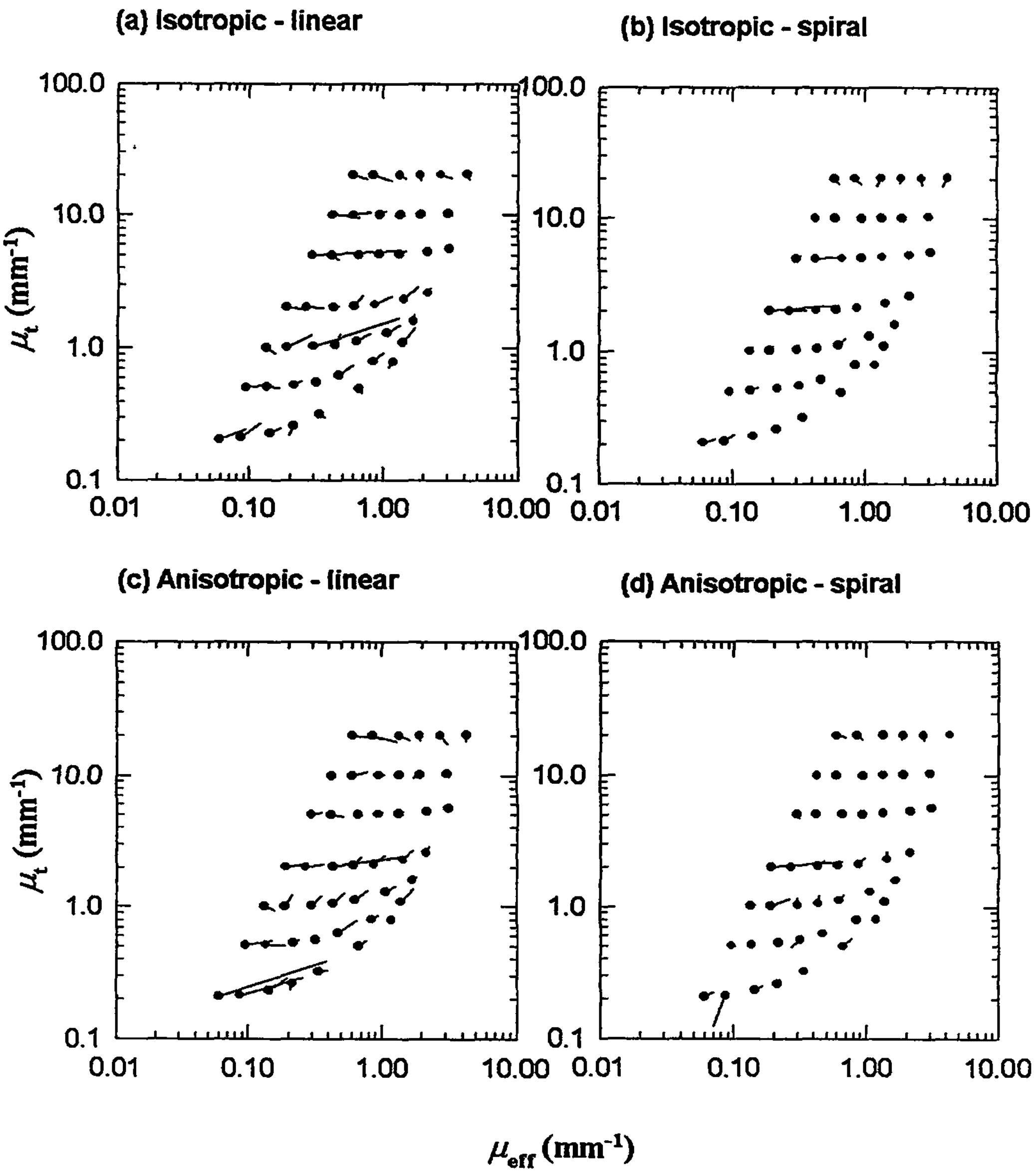

Figure 5.7 Pin plots of μ_t' versus μ_{eff} for isotropic and anisotropic delivery using linear spiral arrays in an infinite medium.

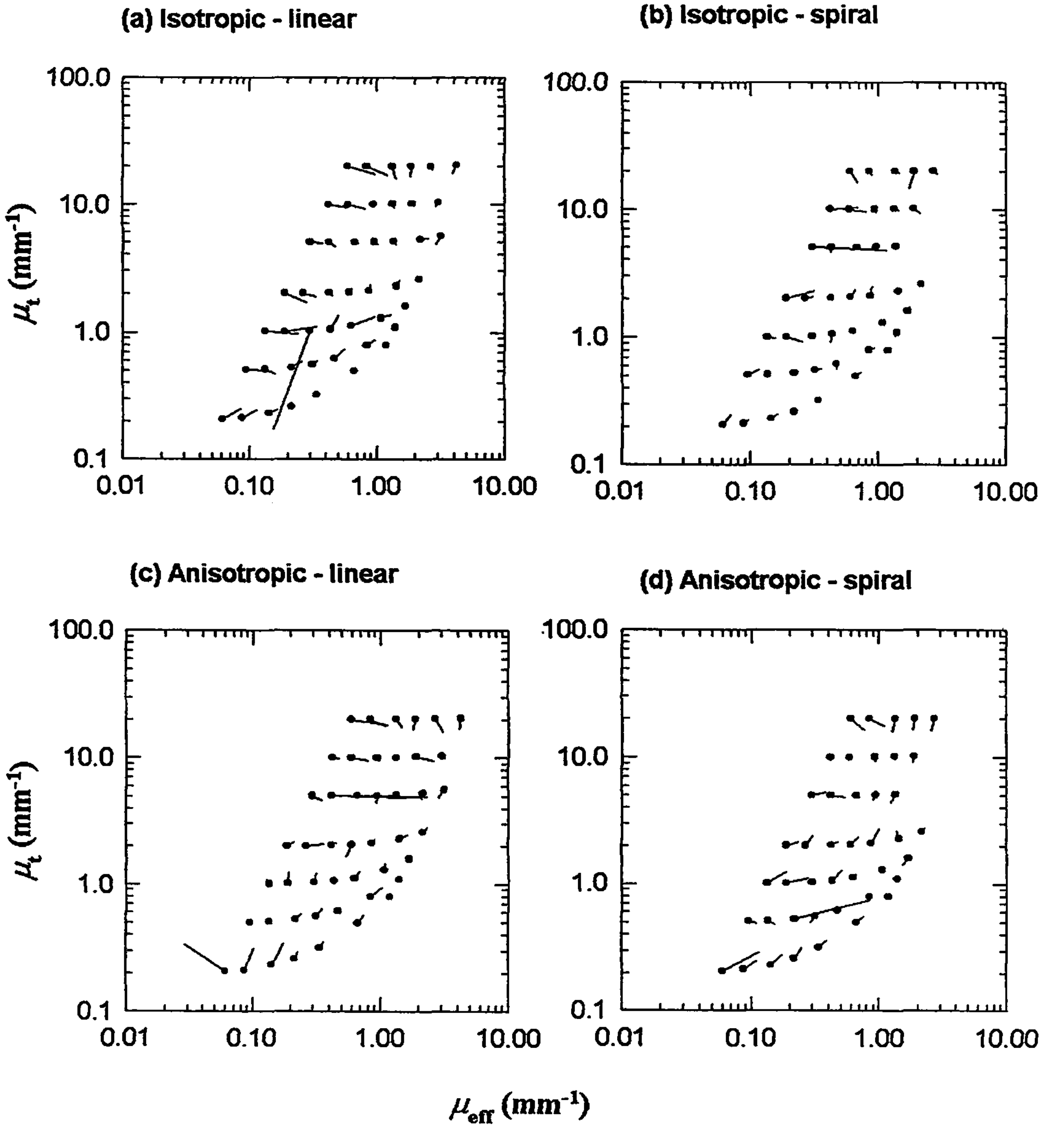

Figure 5.8 Pin plots of μ_t' versus μ_{eff} for isotropic and anisotropic delivery using linear and spiral arrays in a semi-infinite medium with a refractive-index- mismatch at the boundary (n_{rel} = 1.33).

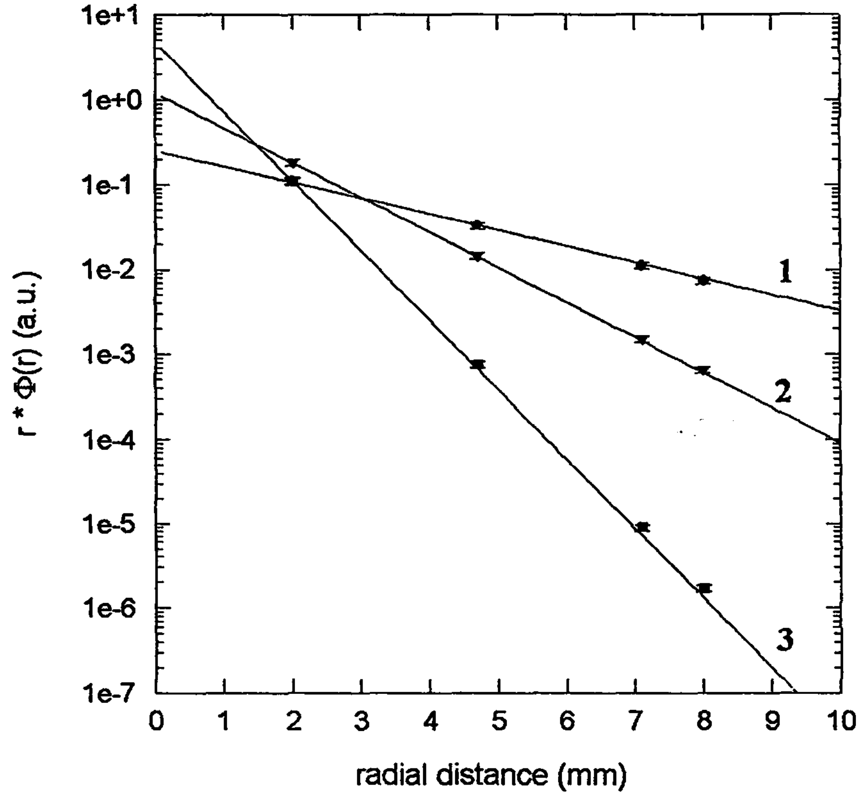

Symbol	Plot	$\mu_a(mm^{-1})$	$\mu_s'(mm^{-1})$	$\mu_{eff}(mm^{-1})$
●	1	0.0593	1	0.4341
▼	2	0.0593	5	0.9487
■	3	0.0593	20	1.8891

Figure 5.9 Comparison of experimental fluence rates (symbols) with the fluence rate distribution predicted by diffusion theory (solid lines) for an isotropic source in an infinite medium.

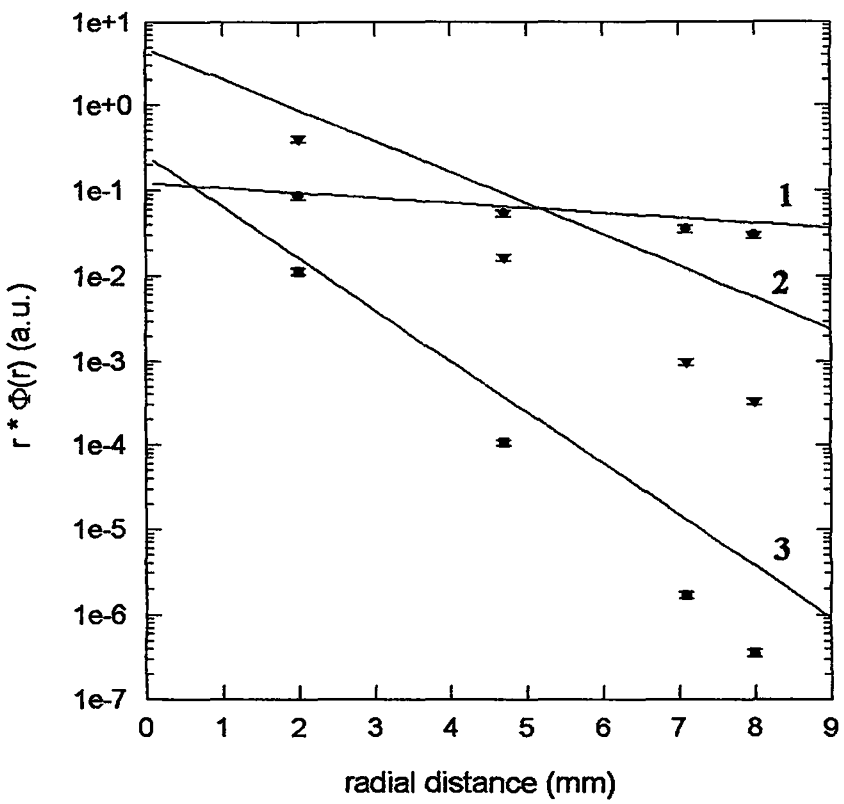

Symbol	Plot	$\mu_a(mm^{-1})$	$\mu_s'(mm^{-1})$	$\mu_{eff}(mm^{-1})$
•	1	0.0118	0.5	0.0181
▾	2	0.5930	20.0	6.0527
▪	3	0.5930	0.5	1.3944

Figure 5.10 Comparison of experimental fluence rates (symbols) with the fluence rate distribution predicted by diffusion theory (solid lines) for an isotropic source in an infinite medium.

5.3 Investigation of finite volume effects

The experimental technique was modified for the interstitial measurements in the finite volumes, the black and white spheres and the rabbit skull, as described in the previous chapter. As discussed in Section 5.2, use of the spiral array improved the accuracy of the derived optical properties since it minimized the effect of the detector probes on the fluence field. However, as described in the previous chapter, a single fibre was translated to the four radial positions for the finite volume measurements. Although this arrangement is impractical for *in vivo* use, in this case it had the two-fold advantage of removing the effect of variability of the detectors, as well as minimizing light absorption by the detectors. The three optical phantoms used all had an albedo of 0.97 and as described previously the optical coefficients were scaled to achieve different sphere sizes (in terms of mfp'). As shown in Table 5.2, phantom 1 has the lowest effective attenuation coefficient, μ_{eff}, and is thus the smallest sphere in terms of transport mean free paths (mfp').

Table 5.2 Optical phantoms used in finite volumes.

Phantom	μ_a (mm^{-1})	μ_s' (mm^{-1})	μ_{eff} (mm^{-1})	δ ($=1/\mu_{eff}$) (mm)	Sphere diameter (mfp')
1	0.015	0.5	0.152	6.57	20
2	0.030	1.0	0.304	3.28	39
3	0.090	3.0	0.913	1.09	119

In the remainder of this chapter an assessment of the finite volume effects is made through a direct comparison of the interstitial measurements of the absolute fluence rate with Monte Carlo calculations for the finite spheres, as well as an evaluation of the accuracy of the derived optical coefficients. For the interstitial measurements in the rabbit skull, a qualitative assessment of the boundary effects is made by consideration of the derived optical properties.

5.3.1 Comparison of experimental fluence rates with Monte Carlo calculations

As shown in Figure 5.11, the diffusion theory solutions for (a) isotropic and (b) anisotropic delivery in an infinite medium (equation 2.14) agree well with infinite Monte Carlo calculations for the optical properties of the phantoms under investigation here. These diffusion models are used to derive the optical properties of the phantoms, as will be discussed later in Section 5.3.2. Since the radius of the white and black spheres are 18.75 and 19 mm, respectively, it is to be expected that finite volume Monte Carlo simulations with the source in the central plane, plane 1, would produce fluence rate distributions comparable with infinite Monte Carlo calculations within the range of observation (2 - 8 mm). Figure 5.12 verifies that this is the case for both types of delivery and boundary conditions (R_d = 0.78 & 0.033 for white and black spheres, respectively) in which boundary effects occur at distances of 7 mm and 4 mm from the boundary for phantoms 1 and 2, respectively. This suggests that the fluence rate distribution is affected at a distance of approximately 4 transport mean free paths (mfp') from the boundary. As expected, phantom 3 with a transport mean free path of 0.32 mm is relatively unaffected.

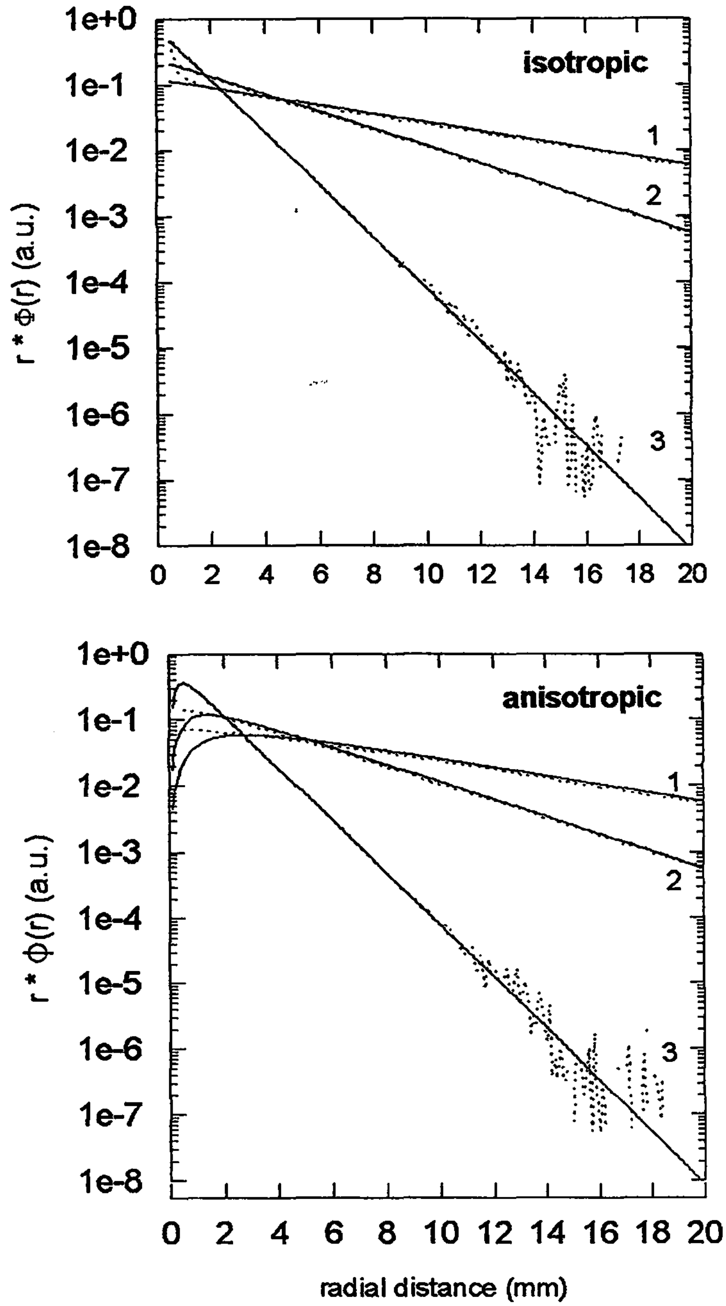

Figure 5.11 Comparison of diffusion theory (solid lines) with Monte Carlo simulations for isotropic and anisotropic delivery in an infinite medium for the three optical phantoms.

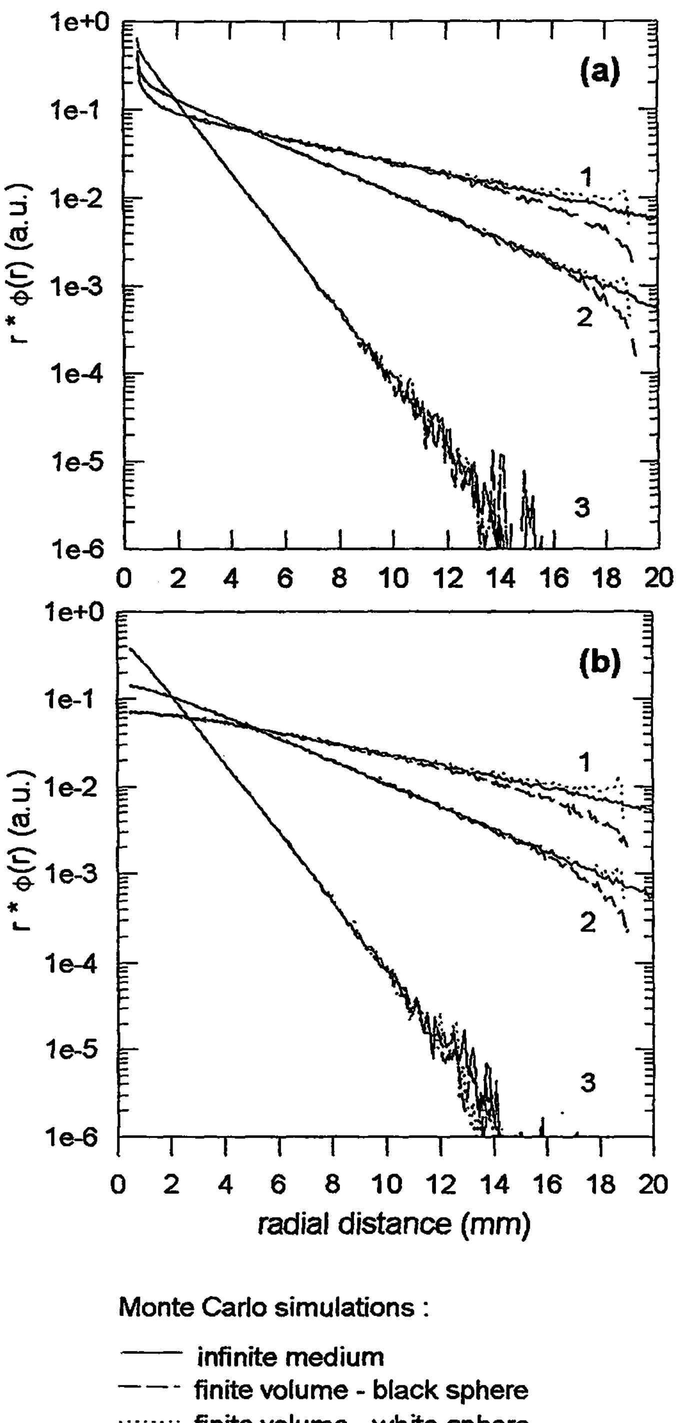

Figure 5.12 Comparison of infinite medium Monte Carlo calculations for (a) isotropic and (b) anisotropic delivery, with finite volume Monte Carlo having delivery in the central plane, for the three optical phantoms.

The detector probe used in this set of measurements was calibrated by determining the ratio of the finite volume Monte Carlo fluence rates to the measured signal. Since the fluence rate distributions for the finite volume Monte Carlo in the central plane were identical to those obtained from Monte Carlo simulations and diffusion theory in infinite media over the range of detector positions (2 - 8 mm), the measured fluence rates in the central planes (phantoms 1 and 2) were employed to calculate the calibration factor. The factor thus obtained was dependent on the responsivity of the probe, the optical coupling and the delivered power. As a result of the calibration factor being determined from a number of measurements as described above, the error in the this factor was determined as the standard deviation of the ratios and was approximately 8%.

The graphs plotted in Figures 5.14.1 - 5.14.6 present a direct comparison of the normalized absolute fluence rates for the interstitial measurements at the detector positions (2, 4.7, 7 and 8 mm), with the fluence rate distributions predicted by the finite volume Monte Carlo model. Each figure presents results for isotropic and anisotropic delivery for each boundary (black : R_d = 0.033 and white : R_d = 0.78), and plane. Included in these plots are the fluence rate distributions calculated from finite volume Monte Carlo for phantoms 1 and 2, with reflectances of 0.85 and 0.35 for the white and black spheres, respectively. When the experimental fluence rates were compared with the Monte Carlo calculations it became apparent that the latter underestimated the fluence rates for both boundary conditions.

The work of Flock et al. (1989) suggests that a semi-infinite medium with refractive index matched boundary conditions, a transport albedo of 0.97 and a reflectance greater than 0.62 would behave like a reflecting boundary causing an increase in the fluence rate compared with infinite diffusion theory. This observation is supported by Figure 5.13, which presents simulation results for a range of reflectances (0.6 - 0.9) using isotropic delivery in plane 3, verifying the accuracy of the finite volume Monte Carlo code. It is apparent that the actual reflectances of the spheres are higher than the values measured and used in the simulations. It was determined that reflectances of 0.85 and 0.35 for the white and black boundaries, respectively, produced fluence rate distributions which matched the experimental data. The problems in the measurement of the diffuse reflectance of the spheres, discussed in the previous chapter, likely gave rise to this discrepancy.

In the central plane (plane 1), there is good agreement between simulation and experimental results for phantoms 1 and 2 for both boundary conditions and delivery fibres, an observation supported by the crossover in the fluence rates for phantoms 1 and 2 at approximately 4.7 mm. The fluence rate at 2 mm is generally underestimated supporting the idea of the detector probes acting as photon sinks (Lilge & Wilson, 1993). This effect is most significant within a few mfp' of the source. Another factor contributing to the inaccuracy of the fluence rate at the 2 mm position is error in positioning the detector. As a result of the short active length of the fluorescent probe, 0.5 mm, alignment of the source and the detector probe in the same plane is critical and problematic particularly in the case of the isotropic spherical diffusing-tip fibre with a diameter of 0.8 mm.

In all cases the experimental fluence rates for phantom 3 show a systematic deviation from the fluence rate distribution predicted by Monte Carlo simulations. At 2 mm from the source the experimental values are significantly underestimated, with the exception of plane 1 for the white sphere and isotropic delivery (see Figure 5.14.1). On average, at 7 and 8 mm the experimental values are 3 and 5 times the Monte Carlo predictions of the fluence rate, respectively. Since phantom 3 is 9 times more attenuating than phantom 1 and the fluence rate distribution falls by approximately 4 orders of magnitude over the range of the detectors, the systematic errors at 7 and 8 mm are most likely due to a contribution to the fluorescent signal from the fluorescence of Intralipid itself.

Since plane 2, which is 4 mm from the base of the sphere, is 2, 4 and 12.5 mfp' from the boundary for phantoms 1, 2 and 3, respectively, one would expect a significant boundary effect for phantom 1, a relatively small effect for phantom 2 and no effect for phantom 3. For isotropic and anisotropic delivery in the white sphere, the Monte Carlo fluence calculations for a reflectance of 0.78 are slightly lower than the experimental values but as indicated by the dotted lines of Figure 5.14.2, there is good agreement between the experiment and the model predictions for a reflectance of 0.85. The discrepancies between the experimentally obtained fluence rates and those of the Monte Carlo calculations for the black and white spheres can be attributed to the positional errors mentioned previously. In plane 2 of the black sphere (Figure 5.14.5) the experimental measurements agree very well with the Monte Carlo fluence rate distributions for a reflectance of 0.35, which is surprisingly high for a black surface.

With the source and the detector in plane 3, significant boundary effects are expected for phantoms 1 and 2 since the boundary is within 2 mfp' in both cases. The experimental results for these phantoms of the white sphere (Figure 5.14.3) show excellent agreement with the simulations, for a reflectance of 0.85. Similarly, the fluence rates for isotropic delivery in plane 3 of the black sphere agree closely with Monte Carlo calculations for a reflectance of 0.35. However, for anisotropic delivery in the black sphere the experimental values for phantom 2 are less than the fluence rates determined from the Monte Carlo simulations by a factor of 2. Since it is unlikely that an error in detector position could have such a large effect, this discrepancy may have arisen as a result of photobleaching of the detector which would have invalidated the previously determined calibration factor. A further quantitative assessment of the boundary effects is made by considering the accuracy of the optical properties derived from the experimental fluence rate measurements, which will be discussed in the next section.

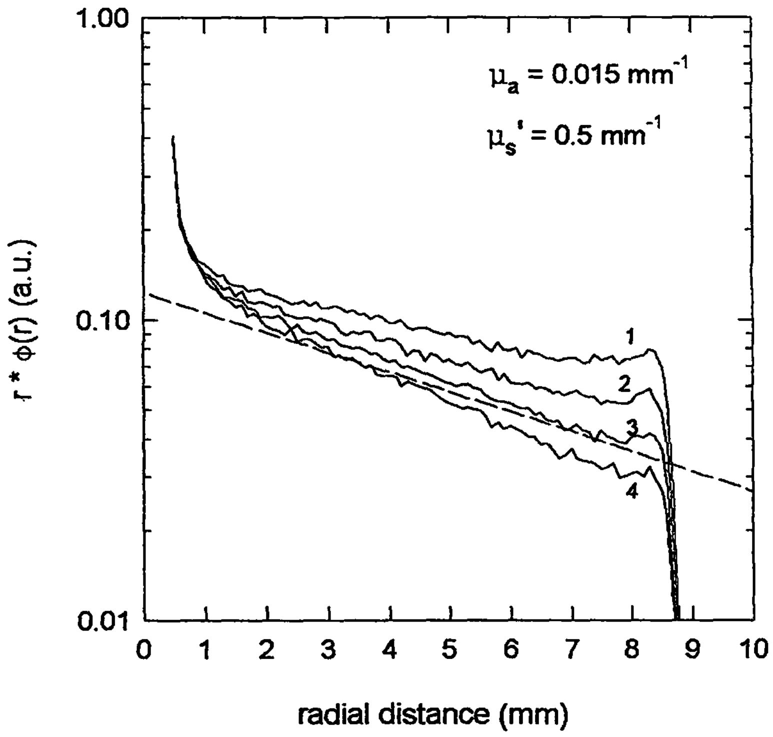

____ finite volume Monte Carlo (isotropic delivery in plane 3 of white sphere)

------ infinite diffusion model

Figure 5.13 Comparison of the fluence rate distribution for infinite diffusion theory (point isotropic source in an infinite medium) with finite volume Monte Carlo. Curves 1 - 4 represent reflectances of 0.9, 0.8, 0.7 and 0.6, respectively.

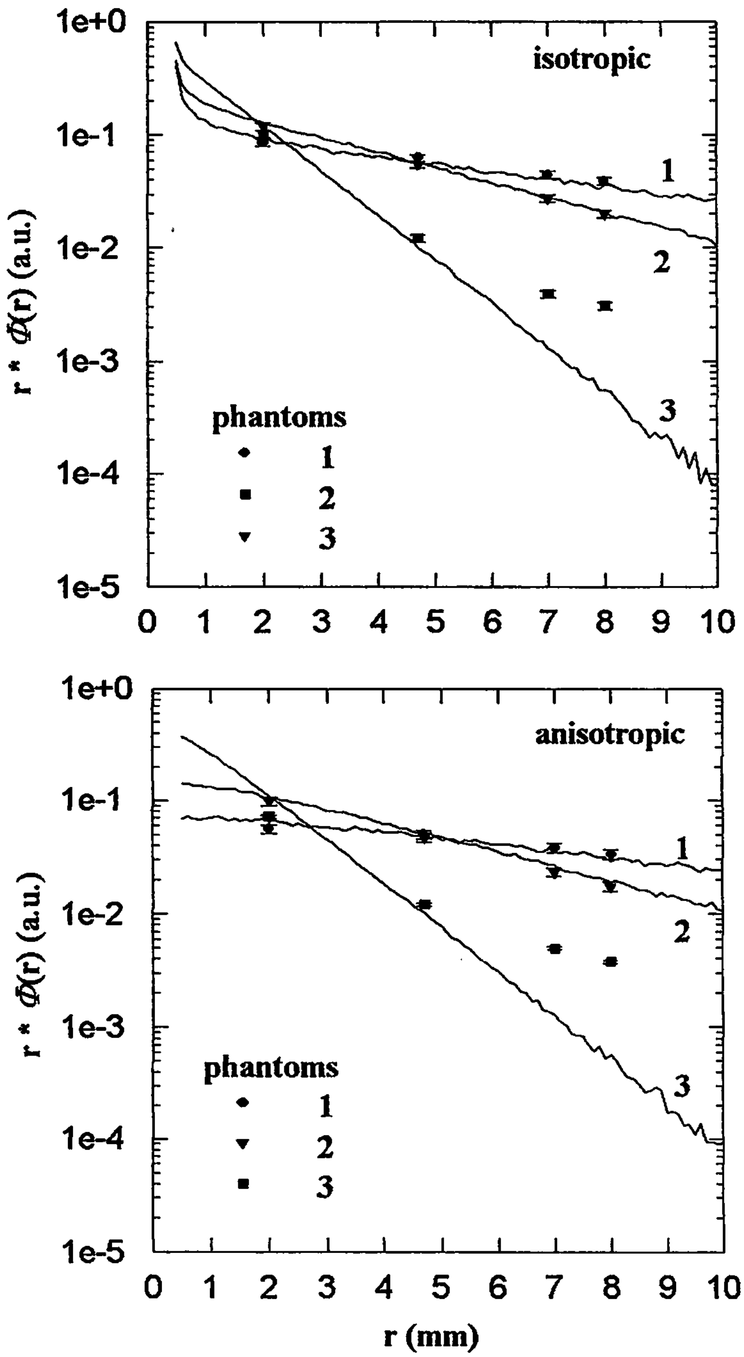

Figure 5.14.1 Delivery in plane 1 of white sphere. Comparison of the experimental fluence rates (symbols) with Monte Carlo simulations (R_d=0.78).

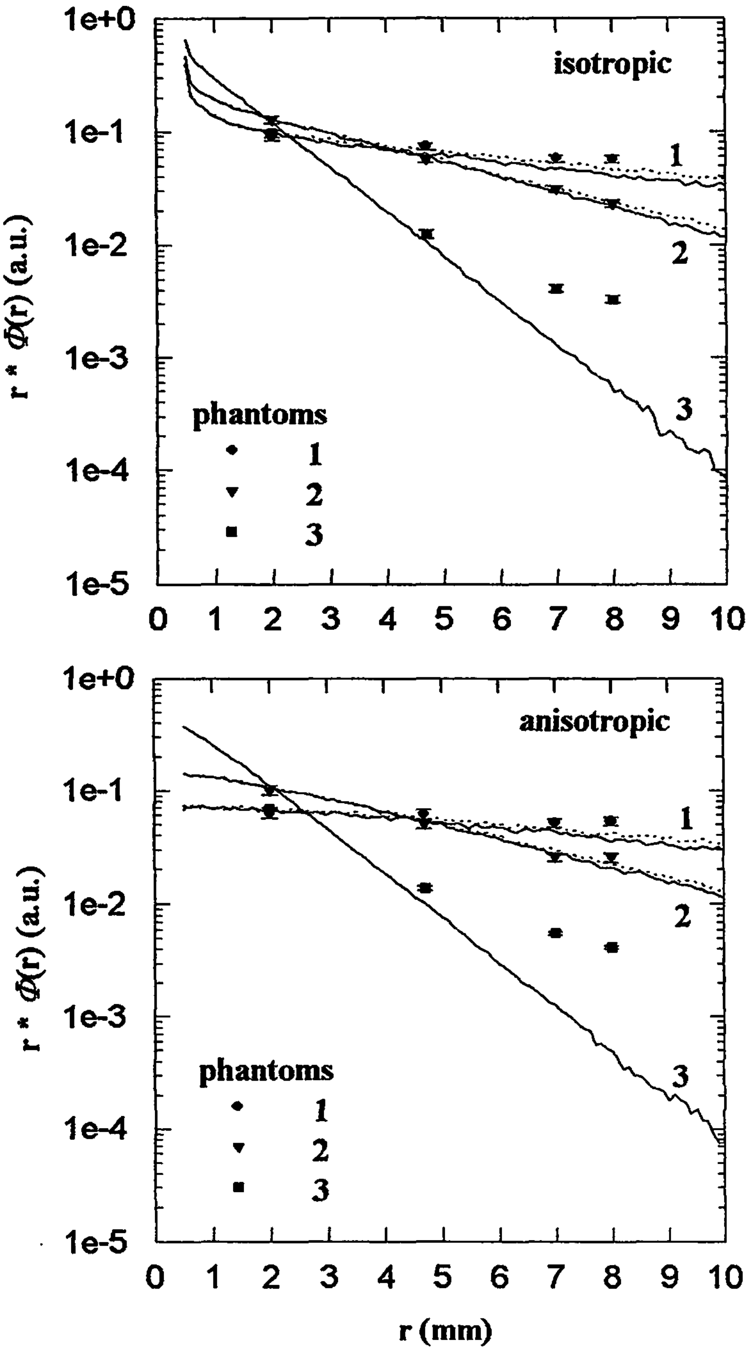

Figure 5.14.2 Delivery in plane 2 of the white sphere. Comparison of the experimental fluence rate (symbols) with the Monte Carlo predictions (solid lines - R_d=0.78 & dotted lines - R_d=0.85).

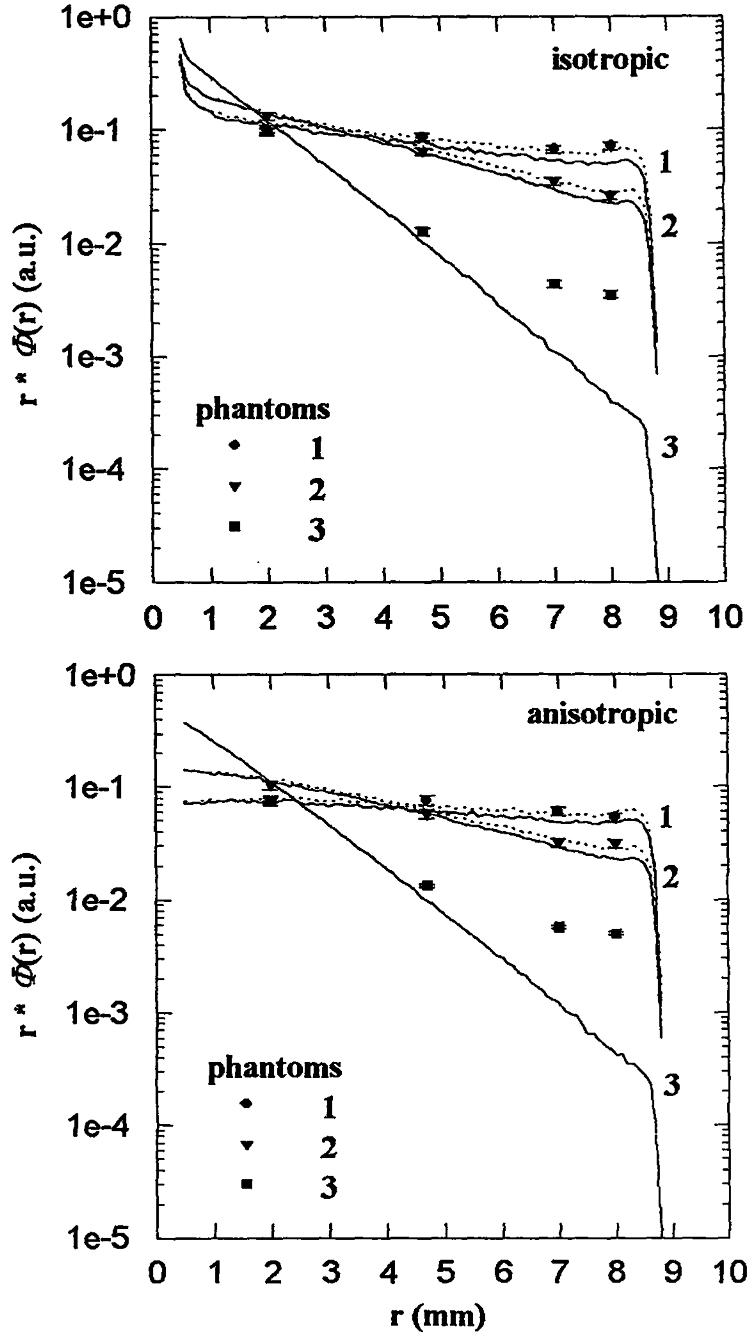

Figure 5.14.3 Delivery in plane 3 of the white sphere. Comparison of the experimental fluence rates (symbols) with the Monte Carlo predictions (solid lines - R_d=0.78 & dotted lines - R_d=0.85).

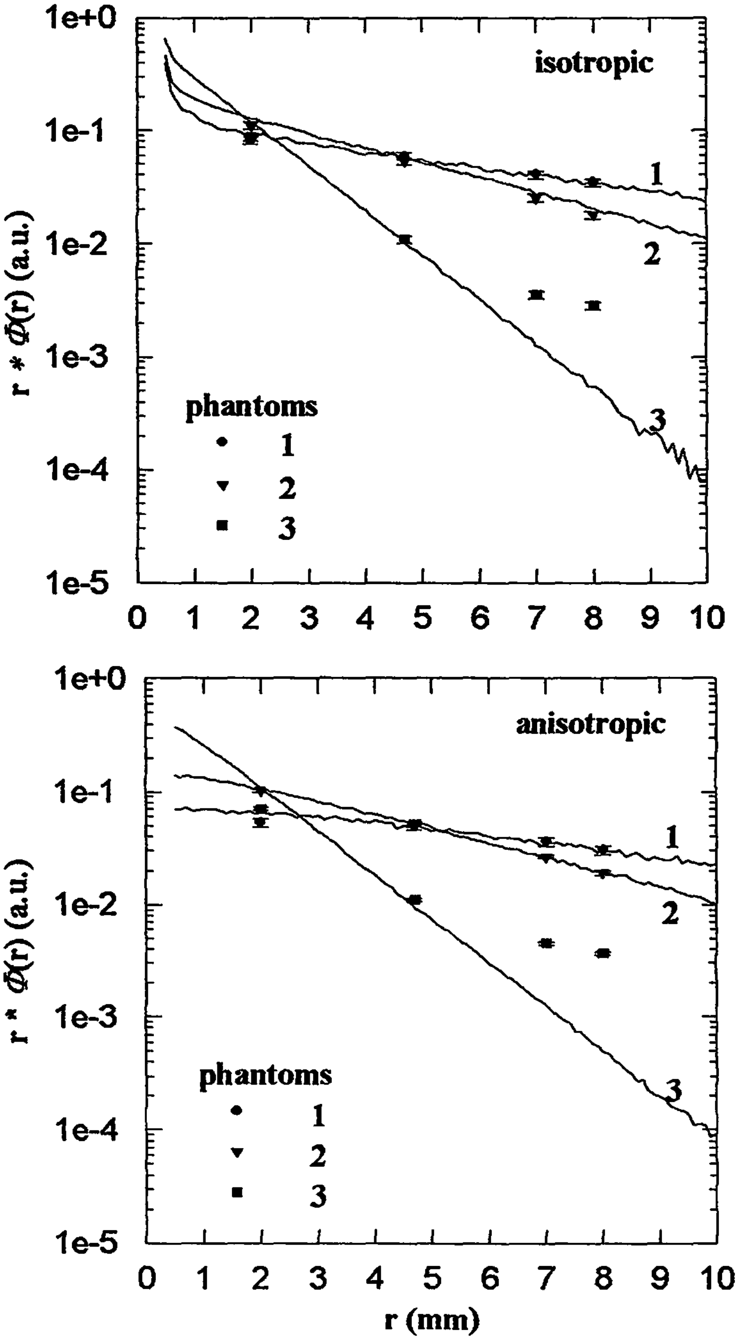

Figure 5.14.4 Delivery in plane 1 of the black sphere. Comparison of the experimental fluence rates (symbols) with the Monte Carlo predictions (R_d=0.033).

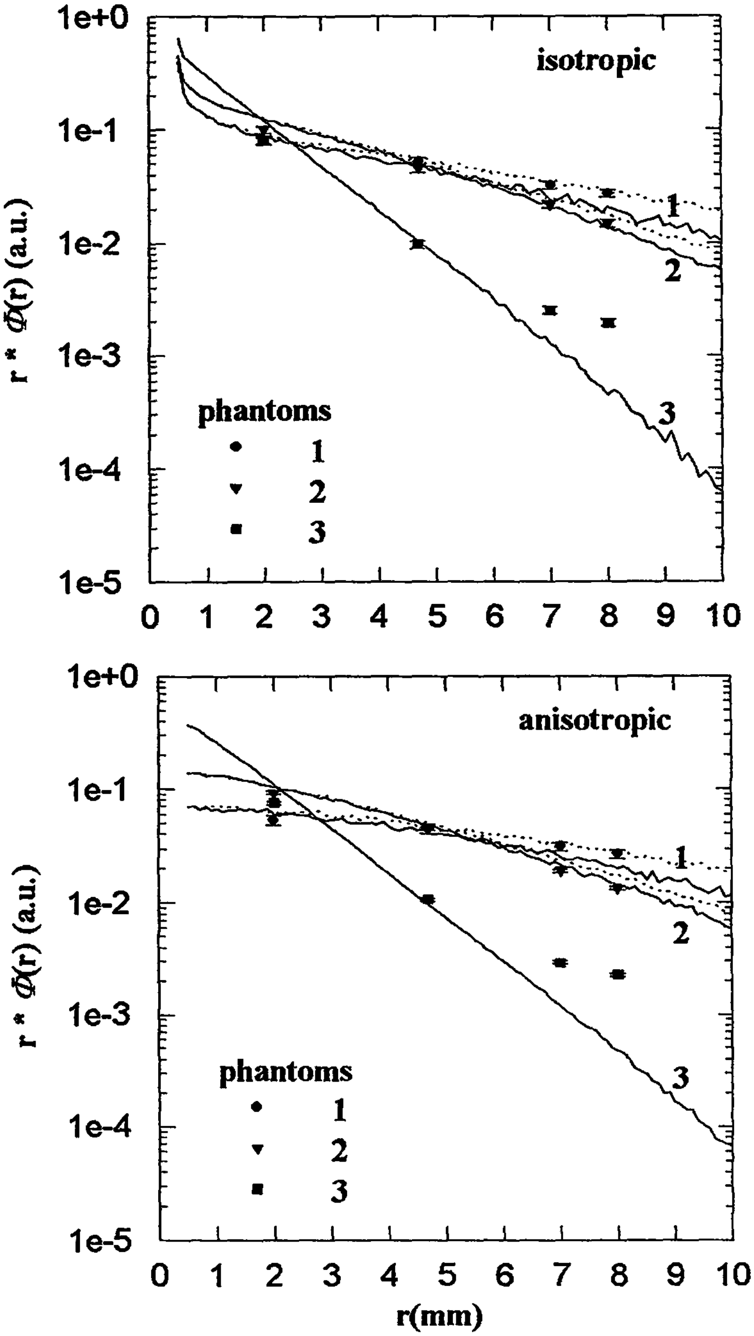

Figure 5.14.5 Delivery in plane 2 of the black sphere. Comparison of the experimental fluence rates(symbols) with the Monte Carlo predictions (solid lines - R_d=0.033 & dotted lines - R_d=0.35)

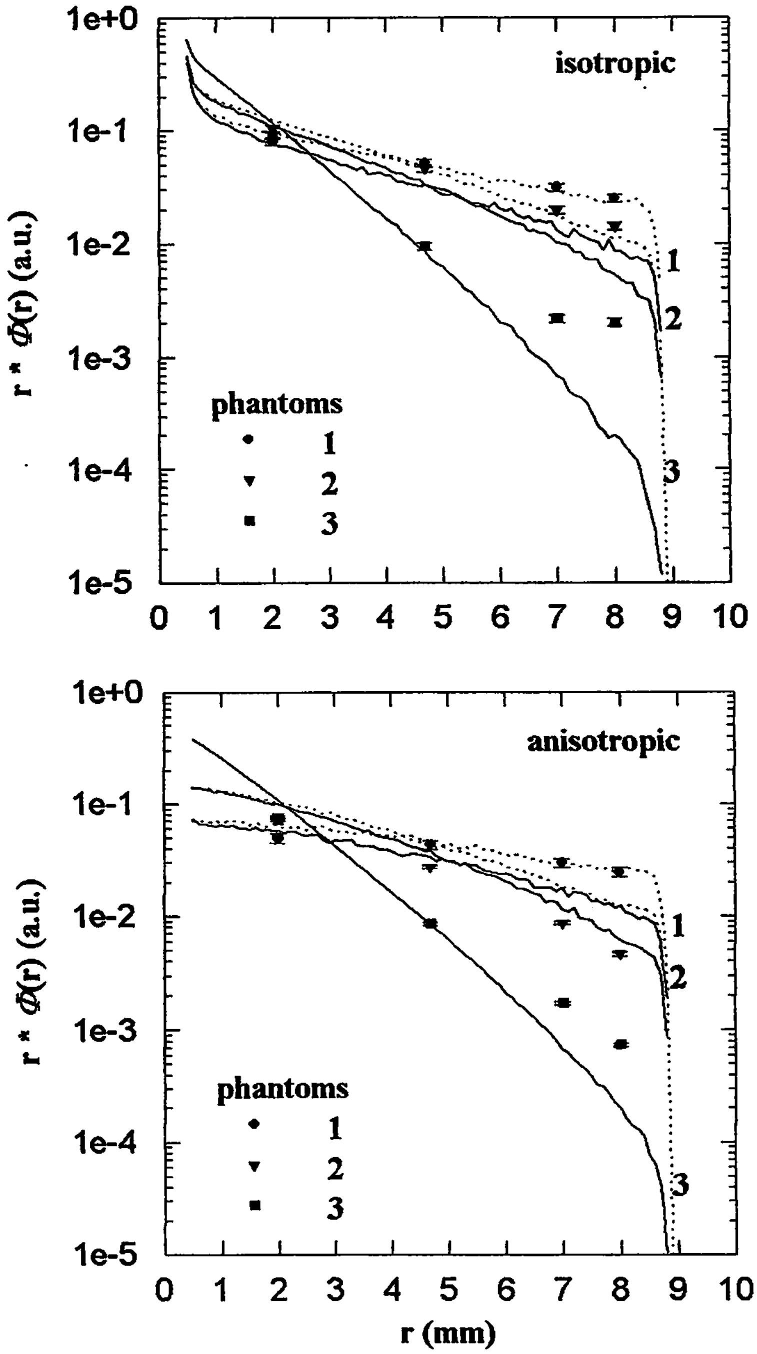

Figure 5.14.6 Delivery in plane 3 of the black sphere. Comparison of the experimental fluence rates(symbols) with the Monte Carlo predictions (solid lines - R_d=0.033 & dotted lines - R_d=0.35).

5.3.2 Derivation of the optical coefficients from the finite volume measurements

The optical properties, μ_a and μ_s', are determined as free parameters in a non-linear least squares fit of the normalized experimental fluence rates to the predictions of the infinite medium diffusion theory model (equation 2.14). Comparison of the optical properties using the two diffusion models for an infinite medium (equations 2.14 & 2.15) indicated differences of at most 5% for the optical properties used here, so that either equation was applicable. The derived optical coefficients and the ratios of the derived to the true values of the coefficients are presented in Tables 5.3.1 - 5.3.3 and 5.4. The finite volume effects are quantified by examination of the magnitude of these ratios.

Since the fluence rate measured in the central plane of the finite spherical volumes is unaffected by the boundaries over the range of the detectors (also see Figure 5.12). It is reasonable to expect that in these cases the optical properties could be derived accurately since the infinite medium diffusion model has proved to be valid. On average, the derived absorption coefficient, μ_a, is accurate to within 13% of the true value for phantoms 1 and 2. Taking into consideration the normalization error of 8% and the underestimation of the fluence rate at the 2 mm position as a result of the photon sink effect, this is a reasonable degree of accuracy for the derived μ_a. Individual cases of larger errors as in the case of plane 1 of Tables 5.3.1a and 5.3.2b could be attributed to positional errors (Figure 5.14.1).

Table 5.3.1 Derived optical coefficients for phantom 1 ((μ_a = 0.015 mm^{-1} & μ_s' = 0.5 mm^{-1}).

a) Isotropic delivery in the white sphere

Plane	$\mu_{a\ derived}$ (mm^{-1})	$\mu_{a\ derived}/\mu_{a\ true}$	$\mu_s'{}_{derived}$ (mm^{-1})	$\mu_s'{}_{derived}/\mu_s'{}_{true}$
1	0.011	0.733	0.445	0.890
2	0.005	0.333	0.434	0.868
3	0.003	0.200	0.487	0.974

b) Anisotropic delivery in the white sphere

Plane	$\mu_{a\ derived}$ (mm^{-1})	$\mu_{a\ derived}/\mu_{a\ true}$	$\mu_s'{}_{derived}$ (mm^{-1})	$\mu_s'{}_{derived}/\mu_s'{}_{true}$
1	0.016	1.067	0.500	1.000
2	0.008	0.533	0.495	0.990
3	0.006	0.400	0.558	1.116

c) Isotropic delivery in the black sphere

Plane	$\mu_{a\ derived}$ (mm^{-1})	$\mu_{a\ derived}/\mu_{a\ true}$	$\mu_s'{}_{derived}$ (mm^{-1})	$\mu_s'{}_{derived}/\mu_s'{}_{true}$
1	0.013	0.873	0.430	0.860
2	0.020	1.340	0.439	0.878
3	0.021	1.433	0.445	0.890

d) Anisotropic delivery in the black sphere

Plane	$\mu_{a\ derived}$ (mm^{-1})	$\mu_{a\ derived}/\mu_{a\ true}$	$\mu_s'{}_{derived}$ (mm^{-1})	$\mu_s'{}_{derived}/\mu_s'{}_{rue}$
1	0.017	1.107	0.486	0.972
2	0.022	1.473	0.507	1.014
3	0.023	1.520	0.485	0.970

Table 5.3.2 Derived optical coefficients for phantom 2 (μ_a = 0.030 mm^{-1} & μ_s' = 1.0 mm^{-1}).

a) Isotropic delivery in the white sphere

Plane	$\mu_{a\ derived}$ (mm^{-1})	$\mu_{a\ derived}/\mu_{a\ true}$	$\mu_s'{}_{derived}$ (mm^{-1})	$\mu_s'{}_{derived}/\mu_s'{}_{true}$
1	0.031	1.050	0.858	0.858
2	0.029	0.983	0.913	0.913
3	0.026	0.853	0.933	0.933

b) Anisotropic delivery in the white sphere

Plane	$\mu_{a\ derived}$ (mm^{-1})	$\mu_{a\ derived}/\mu_{a\ true}$	$\mu_s'{}_{derived}$ (mm^{-1})	$\mu_s'{}_{derived}/\mu_s'{}_{true}$
1	0.036	1.200	0.932	0.932
2	0.032	1.067	0.929	0.929
3	0.026	0.867	0.894	0.894

c) Isotropic delivery in the black sphere

Plane	$\mu_{a\ derived}$ (mm^{-1})	$\mu_{a\ derived}/\mu_{a\ true}$	$\mu_s'{}_{derived}$ (mm^{-1})	$\mu_s'{}_{derived}/\mu_s'{}_{true}$
1	0.033	1.090	0.778	0.778
2	0.039	1.303	0.726	0.726
3	0.040	1.340	0.762	0.762

d) Anisotropic delivery in the black sphere

Plane	$\mu_{a\ derived}$ (mm^{-1})	$\mu_{a\ derived}/\mu_{a\ true}$	$\mu_s'{}_{derived}$ (mm^{-1})	$\mu_s'{}_{derived}/\mu_s'{}_{true}$
1	0.031	1.050	0.940	0.940
2	0.039	1.313	0.910	0.910
3	0.067	2.233	0.937	0.937

Table 5.3.3 Derived optical properties for phantom 3 (μ_a=0.090 mm^{-1} & μ_s' = 3.0 mm^{-1}). Monte Carlo fluence rates are used.

a) Isotropic delivery in the white sphere

Plane	$\mu_{a\ derived}$ (mm^{-1})	$\mu_{a\ derived}/\ \mu_{a\ true}$	$\mu_s'_{\ derived}$ (mm^{-1})	$\mu_s'_{\ derived}\ /\ \mu_s'_{\ true}$
1	0.089	0.993	3.039	1.013
2	0.088	0.983	2.980	0.993
3	0.090	0.998	2.940	0.980

b) Anisotropic delivery in the white sphere

Plane	$\mu_{a\ derived}$ (mm^{-1})	$\mu_{a\ derived}/\ \mu_{a\ true}$	$\mu_s'_{\ derived}$ (mm^{-1})	$\mu_s'_{\ derived}\ /\ \mu_s'_{\ true}$
1	0.093	1.035	2.734	0.911
2	0.091	1.014	2.903	0.968
3	0.092	1.024	2.907	0.969

c) Isotropic delivery in the black sphere

Plane	$\mu_{a\ derived}$ (mm^{-1})	$\mu_{a\ derived}/\ \mu_{a\ true}$	$\mu_s'_{\ derived}$ (mm^{-1})	$\mu_s'_{\ derived}\ /\ \mu_s'_{\ true}$
1	0.086	0.960	3.215	1.072
2	0.087	0.962	3.142	1.047
3	0.090	0.995	3.252	1.084

d) Anisotropic delivery in the black sphere

Plane	$\mu_{a\ derived}$ (mm^{-1})	$\mu_{a\ derived}/\ \mu_{a\ true}$	$\mu_s'_{\ derived}$ (mm^{-1})	$\mu_s'_{\ derived}\ /\ \mu_s'_{\ true}$
1	0.093	1.038	2.870	0.957
2	0.093	1.034	2.879	0.960
3	0.096	1.064	3.108	1.036

The magnitude of the boundary effect and the resulting inaccuracy in the derived optical coefficients is dependent on the actual reflectance and on the proximity of the detectors to the boundary in terms of transport mean free paths. Assuming that the source is incorporated correctly into the diffusion models used for the fitting procedures and given that the boundary effect should be independent of the source distribution, the boundary effect can be determined by comparing the derived coefficients for isotropic and anisotropic delivery for the two boundary conditions. As was discussed previously, one would anticipate an effect for phantom 1 in planes 2 and 3, but only in plane 3 for phantom 2. Furthermore, the inaccuracy in the derived coefficients should be of similar magnitude in plane 2 for phantom 1 and plane 3 for phantom 2 since in both cases the boundary is at a distance of approximately 2 mfp'.

1) Phantom 1 (μ_a=0.015 mm^{-1} & μ_s' = 0.5 mm^{-1})

From the results presented in Table 5.3.1(phantom 1), the derived μ_s' is found to be independent of the reflectance (0.35 or 0.85) or the plane of measurement. In all cases μ_s' is determined to within 13% of the true value of 0.5 mm^{-1}. On the other hand, the derived μ_a values shows a definite boundary effect. It was observed previously that compared with the infinite medium diffusion model, there were increases and decreases in the experimental fluence rate in the white and black spheres, respectively, for phantoms 1 and 2. Therefore, it is to be expected that the derived absorption coefficient would be underestimated for the white sphere and overestimated for the black, as is the case here. Derivation of the optical coefficients from the fluence rates predicted by Monte Carlo calculations resulted in errors of approximately 25% and 50% in planes 2 and 3, respectively for both types of delivery in the white sphere. In the black sphere for isotropic and anisotropic delivery, μ_a is overestimated by 40% and 60% in planes 2 and 3, respectively. In addition to predicting similar errors for both types of delivery, the optical coefficients derived from the Monte Carlo predictions of the fluence rate indicate that the black boundary resulted in larger errors in the derived optical properties.

2) Phantom 2 (μ_a=0.030 mm^{-1} & μ_s' = 1.0 mm^{-1})

As is observed for phantom 1, the derived reduced scattering coefficient, μ_s', is accurate to within 10% of the true value in all cases. From the results for the white sphere (Table 5.3.2.a & b), it can be observed that there is no boundary effect in plane 2. In plane 3 of the white sphere μ_a (determined experimentally) is approximately 15% lower than the true values for both types of delivery. This is more or less in agreement with the 20% error obtained using the Monte Carlo fluence rates. It is unexpected that the results for isotropic delivery in the black sphere suggest the same effect in planes 2 and 3. For anisotropic delivery, the errors in the derived coefficient are also too large (31% and 123% for planes 2 and 3, respectively) to be attributed to boundary effects, when compared with Monte Carlo calculations. These errors were unusually large since these optical properties were derived from the experimental data which were likely affected as a result of photobleaching of the detector, as discussed previously. Using the fluence rates predicted by the Monte Carlo calculations, smaller errors are obtained (12% & 35% for planes 2 and 3, respectively). Since a 40% error is determined in plane 2 for phantom 1, the 35% error in μ_a can be justified. The discrepancies mentioned above which are attributed to the normalization errors, light absorption by the detectors and errors in positioning the detectors, contribute to the error in the derived values thus making quantification of the boundary effect difficult.

3) Phantom 3 (μ_a=0.090 mm^{-1} & μ_s' = 3.0 mm^{-1})

Due to the systematic errors encountered in the experimental measurements (see Section 5.3.1), the optical properties were derived from the Monte Carlo calculations (see Table 5.3.3). Since the measurement planes are always farther than 4 mfp' from the boundary, there are not expected to be any boundary effects and in fact, the optical coefficients can be accurately derived to within 8% of the true values, as shown in Table 5.3.3.

4) Rabbit skull

The results presented in Table 5.4 show that for both phantoms 1 and 2, while μ_s' appears to be unaffected by the boundary, μ_a is always overestimated suggesting that the skull is behaving like a lossy boundary. One would expect bone to be diffuse reflecting but the results seem to suggest instead that most photons are transmitted rather than diffusely reflected at the boundary. The staining of the skull by the Congo Red dye used as the absorber, could have resulted in a reduction in the reflectance. For both phantoms, the overestimate in μ_a increases in moving from the base of the skull to the centre suggesting that complex structures within the skull have an even greater effect than those at the surface. As expected, the effect for phantom 2 is less than that for phantom 1 but it is still significant, with μ_a being overestimated by greater than 45%, a larger effect than predicted for the black sphere.

Table 5.4 Optical coefficients derived from measurements in the rabbit skull). Positions 1, 2 and 5 mm refer to the distance of the source-detector array from the base of the skull (described in Chapter 4).

a) Phantom 1 (μ_a = 0.015 mm^{-1} & μ_s' = 0.5 mm^{-1})

Position (mm)	$\mu_{a\ derived}$ (mm^{-1})	$\mu_{a\ derived}/\mu_{a\ true}$	$\mu_s'_{derived}$ (mm^{-1})	$\mu_s'_{derived}/\mu_s'_{true}$
1	0.025	1.694	0.434	0.868
2	0.026	1.733	0.434	0.868
5	0.028	1.871	0.453	0.906

b) Phantom 2 (μ_a = 0.030 mm^{-1} & μ_s' = 1.0 mm^{-1})

Position (mm)	$\mu_{a\ derived}$ (mm^{-1})	$\mu_{a\ derived}/\mu_{a\ true}$	$\mu_s'_{derived}$ (mm^{-1})	$\mu_s'_{derived}/\mu_s'_{true}$
1	0.044	1.465	0.821	0.821
2	0.046	1.519	0.819	0.819
5	0.049	1.622	0.876	0.876

Chapter 6

Conclusions

In this study, we have investigated further the systematic errors in the interstitial measurement technique and evaluated the effects of boundaries on the absolute fluence rate measurements and on the accuracy of the derived optical properties. It has been shown that the optical coefficients can be derived accurately in optically infinite and semi-infinite media if the measurement technique is tailored to fit the optical properties of the medium. Specifically if a good guess of the optical coefficients can be made, the optimum separation and number of detectors/measurement positions can be chosen over a reasonable range of the fluence rate distribution. Systematic errors such as light absorption by the detector probes, detector positional errors, calibration errors and low signal were found to significantly decrease the accuracy of the derived optical coefficients. Increasing the size of the detectors would improve positional accuracy, responsivity and rigidity. Although this would increase light absorption by the probes, this effect could be potentially quantified and corrected for.

Measurements in the finite spherical volumes show definitively that fluence rate measurements made within 4 mfp' of the boundary are affected resulting in significant errors in the derived absorption coefficient, μ_a. For the reflecting ($R_d = 0.85$) and absorbing ($R_d = 0.35$) boundaries evaluated, the errors in the derived μ_a are approximately 20% and 40%, respectively, within 2 mfp' of the boundary. Clearly if the optical properties are to be derived accurately, fluence rate measurements have to be made at distances greater than 4 mfp' from the boundary. On the other hand, measurements made close to the boundary may allow determination of the reflectance of the boundary. A combination of these approaches would enable accurate fluence rate dosimetry in clinical situations where boundaries will have a significant effect.

In the complex geometry of the rabbit skull, μ_a was significantly overestimated suggesting that there was substantial transmittance and the bone was behaving as a lossy boundary. These results indicate that any measurements made in the cranial cavity of the rabbit are subject to boundary effects causing μ_a to be potentially overestimated by at least 50%. More extensive studies need to be carried out to determine empirical correction factors which could be applied to fluence rate measurements in rodent brain models and other finite measurement geometries.

References

Arnfield, M.R., Tulip, J. and McPhee, M.S. (1988) Optical Propagation in Tissue with Anisotropic Scattering. **IEEE Transactions on Biomedical Engineering, 35, No. 5**, 372-381.

Arnfield, M.R., Tulip, J., Chetner, M. and McPhee, M.S. (1989) Optical dosimetry for interstitial photodynamic therapy. **Med. Phys., 16(4)**, 602-608

Arnfield, M.R., Tulip, J. and McPhee, M.S. (1990) Photodynamic therapy dosimetry in postmortem and *in vivo* rat tumors and an optical phantom. **Photochem. Photobiol., 51, No. 6**, 667-674.

Bevington, P.R. (1969) **Data Reduction and Error Analysis for the Physical Sciences.** pp 208-215. McGraw -Hill Inc., New York.

Bolin, F.P., Preuss, L.E., Taylor, R.C. and Ference, R.J. (1989) Refractive index of some mammalian tissues using a fiber optic cladding method. **Appl. Opt., 28**, 2297-2303.

Carter, L.L. and Cashwell, E.D. (1975) **Particle-Transport Simulation with the Monte Carlo Method**, USERDA Technical Information Center, Oak Ridge.

Cheong, W., Prahl, S.A. and Welch, A.J. (1990) A Review of the Optical Properties of Biological Tissues. **IEEE J. Quant. Electr., 26, No. 12,** 2166-2186.

Doiron, D.R. (1984), Photophysics of and Instrumentation for Porphyrin Detection and Activation. In: **Porphyrin Localization and Treatment of Tumors**, pp. 41-73. Alan R. Liss, Inc.

Driver, I., Lowdell, C.P. and Ash, D.V. (1991) *In vivo* measurement of the optical interaction coefficients of human tumours at 633 nm. **Phys. Med. Biol., Vol 36, No 6**, 805-813.

Duderstadt, J.J. and Hamilton, L.J. (1976) **Nuclear Reactor Analysis**, John Wiley and Sons, Inc., Toronto.

Eason, G., Veitch, R., Nisbet, R. and Turnbull, F. (1978) The theory of backscattering of light by blood. **J. Phys., D 11**, 1463-1479.

Egan, W.G. and Hilgeman, T.W. (1979) **Optical Properties of Inhomogeneous Materials.** Academic, New York.

Farrell, T.J. and Patterson, M.S. (1992) A diffusion theory model of spatially resolved, steady-state diffuse reflectance for the non-invasive determination of tissue optical properties *in vivo*. **Med. Phys., 19(4),** 879-888.

Farrell, T.J., Wilson, B.C. and Patterson, M.S. (1992) The use of a neural network to determine tissue optical properties from spatially resolved diffuse reflectane measurements. **Phys. Med. Biol., 37, No. 12,** 2281-2286.

Flock, S.T., Wilson, B.C. and Patterson, M.S. (1989) Monte Carlo Modeling of Light Propagation in Highly Scattering Tissues - I : Model Predictions and Comparison with Diffusion Theory. **IEEE Transactions on Biomedical Engineering, 36, No. 12,** 1162-1167.

Groenhuis, R.A.J., Ferweda, H.A. and Ten Bosch, J.J. (1983) Scattering and absorption of turbid materials determined from reflection measurements. 1: Theory. **Appl. Opt., 22, No. 16,** 2456-2462.

Grosjean, C.C. (1956) A High Accuracy Approximation for Solving Multiple Scattering Problems in Infinite Homogeneous media. **Nuovo Cimento, III, No. 6,** 1266-1275.

Henyey, L.G. and Greenstein, J.L. (1941) Diifuse radiation in the galaxy. **Astrophys. J., 93,** 70-83.

van de Hulst, H.C. (1980) **Multiple light scattering, Volume 2**, Academic, New York.

Ishimaru, A. (1989) Diffusion of light in turbid material. **Appl. Opt., 28, No. 12**, 2210-2215.

Jacques, S.L., Alter, C.A. and Prahl., S.A. (1987) Angular Dependence of HeNe Laser Light Scattering by Human Dermis. **Lasers in Life Sciences, 1(4)**, 309-333.

Jaywant, S., Wilson, B.C., Patterson, M.S., Lilge, L., Flotte, F., Woolsey, J. and Mcculloch, C. (1993) Temperature-dependent changes in the optical absorption and scattering spectra of tissues: correlation with ultrastructure. **Proc. SPIE, 1882**, 218-229.

Key, H., Davies, E.R., Jackson, P.C. and Wells, P.N.T. (1991) Monte Carlo modelling of light transport in breast tissue. **Med. Phys. Biol. Vol 36, No. 5**, 591-605.

Kienle, A. and Steiner, R. (1994) Determination of the optical properties of tissue by spatially resolved transmission measurements and Monte Carlo simulations. **Proc. SPIE, 2134**.

Knuth, D.E. (1981) **The Art of Computer Programming, Vol 2**. Chapter 3, Addison-Wesley, Reading,MA.

Kubelka, P. (1948) New contributions to the optics of intensely lightscattering materials, Part 1. **J. Opt. Soc. Am., 38**, 448-457.

Lilge, L., Flotte, T.J., Kochevar, I.E., Foley, J.W. and Wilson, B.C. (1990) A fluorescent-tip optical fiber probe for quantitative light dosimetry in light scattering media and in tissue. **SPIE Proceedings of Photodynamic Therapy: Mechanisms II, 1203**, 106-117.

Lilge, L., Haw, T. and Wilson, B.C. (1993) Miniature isotropic optical fibre probesfor quantitative light dosimetry in tissue. **Phys. Med. Biol., 38**, 215-230.

Lilge, L. and Wilson, B.C. (1993) The accuracy of interstitial measurements of absolute light fluence rate in the determination of tissue optical properties. **SPIE Proceedings of Laser-Tissue Interaction IV, 1882**, 291-304.

Madsen, S.J., Patterson, M.S. and Wilson, B.C. (1992) The use of India ink as an optical absorber in tissue-simulating phantoms. **Phys. Med. Biol., 37, No. 4**, 985-993.

Marijnissen, J.P.A., Star, W.M., van Delft, J.L. and Frunken, N.A.P. (1985) Light intensity measurements in optical phantoms and in vivo during HPD-photoradiation treatment, using a miniature light detector with isotropic response. In: **Photodynamic Therapy of Tumors and of Diseases**, pp 387-390. Jori, G. and Perriac (eds.).

Metropolis, N. and Ulam, S. (1949) The Monte Carlo Method. **Journal of the American Statistical Asssociation, 44, No. 247**, 335-341.

Parrish, J.A. and Wilson, B.C. (1991) Current and Future Trends in Laser Medicine. **Photochem. Photobiol., 53, No. 6**, 731-738.

Patterson, M.S., Chance, B. and Wilson, B.C. (1989) Time resolved reflectance and transmittance for the non-invasive measurement of tissue optical properties. **Appl. Opt. 28**, 2331-2336.

Patterson, M.S., Wilson, B.C. and Graff, R. (1990) *In vivo* tests of the concept of photodynamic threshold dose in normal rat liver photosensitized by aluminium chlorosulphonated pthalocyanine. **Photochem. Photobiol., 51, No. 3**, 343-349.

Patterson, M.S., Moulton, J.D., Wilson, B.C., Berndt, K.W. and Lakowicz, J.R. (1991) Frequency-domain reflectance for the determination of the scattering and absorption properties of tissue. **Appl. Opt., 30, No. 31**, 4474-4476.

Prahl, S.A. (1988) **Light Transport in Tissue**. PhD dissertation. University of Texas, Austin.

Prahl, S.A., Keijzer, M., Jacques, S.L. and Welch, A.J. (1989) A Monte Carlo Model of Light Propagation in Tissue. **Dosimetry of Laser Radiation in Medicine and Biology, SPIE Institute Series, IS 5**, 102-111.

Profio, A.E. and Doiron, D.R. (1981) Dosimetry considerations in phototherapy. **Med. Phys., 8(2)**, 190-196.

Profio, A.E. and Doiron, D.R. (1987) Transport of light in tissue in photodynamic therapy. **Photochem. Photobiol., 46, No. 5**, 591-599.

Profio, A.E. (1989) Light transport in tissue. **Appl. Opt., 28, No. 12**, 2216-2221.

Raeside, D.E. (1976) Monte Carlo Principles and Applications. **Phys. Med. Biol., 21, No. 2**, 181-197.

Star, W.M. and Marijnissen, J.P.A. (1987) Quantitative light dosimetry in vitro and in vivo. **Laser. Med. Surg. 7**, 235-242.

Star, W.M., Wilson, B.C. and Patterson, M.S. (1992), Light Delivery and Optical Dosimetry in Photodynamic Therapy of Solid Tumors. In: **Photodynamic Therapy : Basic Principles and Clinical Applications**, Henderson, B.W. and Dougherty, T.J. (eds.), pp 335-368. Marcel Dekker, Inc., New York.

van Stavaren, H.J., Moes, C.J.M., van Marle, J., Prahl, S.A. and van Gemert, M.J.C. (1991) Light scattering in Intralipid-10% in the wavelength range of 400-1100 nm. **Appl. Opt., 30, No. 31**, 4507-4514.

Sutter, E. (1989) Quantities and Units of Optical Radiation and their Measurement. **Dosimetry of Laser Radiation in Medicine and Biology, SPIE Institute Series, IS 5**, 38-60.

Svaasand, L.O. (1984), Optical Dosimetry for Direct and Interstitial Photoradiation Therapy of Malignant Tumors. In: **Porphyrin Localization and Treatment of Tumors**, pp. 91-114. Alan R. Liss, Inc.

Turner, J.E., Wright, H.E. and Hamm, R.N. (1994) Review Article : A Monte Carlo Primer for Health Physicists. **Health Physics**, 717-733.

Wang, L. and Jacques, S.L. (1992) **Monte Carlo Modeling of Light Transport in Multi-layered Tissues in Standard C**. Laser Biology Research Laboratory, Univ. of Texas.

Wilson, B.C. and Adam, G. (1983) A Monte Carlo model for absorption and flux distributions. **Med. Phys., 10, No. 6**, 824-830.

Wilson, B.C., Jeeves, W.P. and Lowe, D.M. (1985) *In vivo* and *post mortem* measurements of the attenuation spectra of light in mammalian tissues. **Photochem. Photobiol., 42, No. 2**, 153-162.

Wilson, B.C. and Patterson, M.S. (1986) The physics of photodynamic therapy. **Phys. Med. Biol., 31, No. 4**, 327-360.

Wilson, B.C., Patterson, M.S. and Flock, S.T. (1987) Indirect *versus* direct techniques for the measurement of the optical properties of tissues. **Photochem. Photobiol., 46, No. 5**, 601-608.

Wilson, B.C. and Jacques, S.L. (1990) Optical Reflectance and Transmittance of Tissues: Principles and Applications. **IEEE J. Quant. Electr., 26, No. 12**, 2186-2199.

Wilson, B.C. (1991a) Optical Properties of Tissues. In: **Encyclopedia of Human Biology, Vol. 5**, pp. 587-597. Academic Press, Inc.,

Wilson, B.C. (1991b) Modelling and measurements of light propagation in tissue for diagnostic and therapeutic applications. In: **Laser Systems for Photobiology and Photomedicine**. pp 13-27. Chester, A.N. et al., (eds.). Plenum Press, New York.